Scuola Normale Superiore
PISA

Measurement of the $B^o\bar{B}^o$ Mixing Using Muon Pairs at CDF

tesi presentata dal **Dott. Emilio Meschi**

per il conseguimento del Diploma di Perfezionamento in FISICA
Pisa, 1995.

relatore **Prof. Luciano F. Ristori**

relatore **Dott. Stefano Belforte**

Well, that [a straight line] *is just what we see when one of our triangular or other acquaintances comes toward us in Flatland. As there is neither sun with us, nor any light of such a kind as to make shadows, we have none of the helps to the sight that you have in Spaceland. If our friend comes closer to us we see his line becomes larger; if he leaves us it becomes smaller: but still he looks like a straight line; be he a Triangle, Square, Pentagon, Hexagon, Circle, what you will–a straight Line he looks and nothing else.*

(Edwin Abbott Abbott - Flatland*)*

Contents

Abstract **1**

Introduction **3**

1 Theory **7**
1.1 Introduction: the Standard Model 7
1.1.1 The quark mixing matrix 9
1.1.2 Wolfenstein (approximate) parameterization of V_{CKM} . . . 10
1.2 Mixing - General Formalism 13
1.3 Mixing in the $B^0\bar{B}^0$ system 16
1.3.1 Measurements and constraints on x_d 17
1.3.2 Combined measurements of x_s/x_d 18
1.3.3 Constraints on the unitary triangle from mixing and CP violation 19

2 Experimental Scenario **21**
2.1 B-meson production and decay 21
2.1.1 B meson production facilities 21
2.1.2 "Near threshold" production 22
2.1.3 "Continuum" machines 23
2.1.4 Z^0 peak colliders 23
2.1.5 Hadron Colliders 23
2.2 Mixing measurements 24
2.2.1 Mixing at the $\Upsilon(4S)$ 24
2.2.2 Mixing outside the $\Upsilon(4S)$ 26
2.3 Direct measurements of ${B_s}^0\bar{B_s}^0$ mixing 29

3 The CDF Detector **31**
3.1 Overview 31
3.2 The Central Tracking Chamber 34

3.3 Muon systems 34
3.4 Trigger and data acquisition 37

4 Mixing at CDF **41**
4.1 The Dielectron Channel 43
4.2 The Electron-Muon Channel 45
4.3 The dimuon channel 48

5 Real muon pairs in CDF dimuon data **51**
5.1 Data samples and selection cuts 53
5.1.1 Muon quality cuts 54
5.1.2 The J/ψ sample 58
5.1.3 The $K_s^0 \to$"μ"π sample 62
5.1.4 Study of selection cuts on real data 63
5.2 Technique to evaluate the number of real muon pairs 66
5.2.1 Single muon equations 68
5.2.2 Dimuon equations 70
5.3 Determination of the N's 73
5.4 Determination of ϵ_μ 78
5.5 Determination of ϵ_f^- 80
5.5.1 ϵ_f^π vs. $\epsilon_f^{K^-}$ 82
5.5.2 ϵ_f^π vs. ϵ_f from $K_s^0 \to \pi^+\pi^-$ 84
5.5.3 Effect of protons and anti-protons 88
5.5.4 ϵ_f^- from $\Phi^0 \to K^+K^-$ 91
5.6 True muon fractions 93
5.6.1 Monte Carlo Algorithm 93
5.6.2 Statistical and systematic uncertainties 94

6 Determination of R and $\bar{\chi}$ **99**
6.1 Cosmics background 99
6.2 Drell-Yan background 101
6.2.1 E_t^{iso} modeling for non-Drell-Yan component 102
6.2.2 E_t^{iso} modeling for Drell-Yan 103
6.2.3 Drell-Yan fraction in the data 106
6.2.4 Comparison with the CDF measurement of the Drell-Yan cross section 111
6.3 The R ratio 113
6.4 Determination of $\bar{\chi}$ 113
6.4.1 Monte Carlo study of B-meson decays 114

6.4.2 Sequentials fraction 114
6.4.3 Charm fraction 115
6.4.4 Conclusions, the value of $\bar{\chi}$ 115

Abstract

This thesis concerns the experimental study of B mesons (mesons containing a b quark) produced in proton-antiproton collisions at center of mass energy of 1800 GeV. This work has been performed within the CDF collaboration. CDF is a general purpose detector located at Fermilab, in Batavia (Illinois), which exploits the Fermilab proton-antiproton collider (Tevatron).

The specific problem that has been the focus of this study is the identification of muon pairs originating from the decay of a pair of B mesons. The physics of the B mesons is a very rich and stimulating field, that offers the opportunity to probe the validity of the current description of the matter at its more fundamental level (the Standard Model). In addition, the study of B mesons can provide insight on the mechanism at the basis of the violation of the particle-antiparticle symmetry (CP symmetry) and on the mixing of quark families in weak interactions.

In a hadron collider like the Tevatron, B mesons are produced only in about one collision in a thousand and together with tens of other particles. They then decay very rapidly, most of the times in an indistinctive final state. One of the cleanest signature for B mesons, is the production of a muon in the decay, which happens about 10% of the times. These muons are produced in a kinematic region populated by a much larger number of hadrons (especially pions and kaons), which usually originate from other processes than b quark production. The standard technique to identify muons among this background, is to exploit their unique capability among charged particles to traverse a large amount of material without interacting. Unfortunately, a non-negligible fraction of π and K mesons can simulate a muon signal, either because they decay to a muon-neutrino pair, or simply due to their non-zero (although very small) probability of traveling without interacting in any finite length of material. In a typical situation in the CDF case, about half of the particles that give a muon-like signal in the detector are in fact hadrons.

Therefore, the problem of identifying muons produced in B meson decays is a very difficult one.

In this work a technique will be introduced that allows to count the number

of muon pairs produces, via a statistical subtraction of the background.

This result, which can be used in several different analyses, is applied in this work to the measurement of the so called "mixing in the $B^0\bar{B}^0$ system". Perturbative corrections in the weak interactions allow a B meson to change into its own antiparticle before decaying. This phenomenon is called "mixing ". In proton-antiproton interactions the great majority of B mesons are produced in pairs of opposite flavour (e.g. $B^0\bar{B}^0$), but, as a consequence of mixing, it is possible for one of the mesons to change flavour so that for example two B^0 's or two $\bar{B}^0$'s can be found in the same event. This fact in turn produces a consistent fraction of events in which the two muons originating from the decay of the B mesons have the same charge, while in the absence of mixing all such muons would have opposite charge, since one originates from a b quark and the other from a $\bar{b}$ antiquark. Therefore the final part of this thesis will address the measurement of the ratio between like-sign and opposite-sign muon pairs coming from the decay of neutral B mesons, in order to obtain the mixing probability $\bar{\chi}$.

The mixing probability has been already measured by other experiments, but as far as CDF is concerned, until now results have been reported only in the much cleaner electron-muon and electron-electron channels. The present work, besides providing a tool for counting the number of real muon pairs produced in proton-antiproton collisions at CDF, contains a first estimate of the mixing parameter in the muon-muon channel, thus completing the set of measurements possible at CDF with a channel which has higher statistics and different systematics. The result $\bar{\chi} = 0.121 \pm 0.026(\text{stat.})^{+0.032}_{-0.031}(\text{sys.})$ is in agreement with the current world average.

Introduction

In the last decade, beauty physics has received a great deal of interest in the particle physics community, both from the experimental and theoretical viewpoints. There are several reasons for this success. First, until the very recent discovery of the top quark, beauty was the heaviest quark flavor, and the one whose properties were less known. Second, the Standard Model and QCD predict a number of new, interesting phenomena in the b sector, starting with the spectroscopy of $b\bar{b}$ bound states, to $B^0\bar{B}^0$ mixing, up to the yet unobserved CP violation phenomena. Third, because of the relatively large mass of b, beauty hadron physics lends itself as an almost perfect testing ground for SM flavor physics, being comparatively immune to the large non-perturbative QCD corrections which affect bound systems of the lighter quarks.

During the 80's the spectroscopy of hidden and open flavor beauty hadrons has known a period of great activity and success worldwide. In the meantime, both the Standard Model and QCD theoretical frameworks were being consolidated and tested, first in their gross features, and then, with the advent of the LEP experiments and CDF, to a higher and higher level of refinement. The growing confidence in the predictive power of the SM, and the lack of conclusive results in the search for direct CP violation in neutral kaon decays have led to consider the measurement of the phases of the Cabibbo-Kobayashi-Maskawa matrix a crucial step in the comprehension of the origin of CP violation. This last subject has become one of the leading themes for experiments in the next decade. It is believed it could help, along with high precision measurements of the ratio ϵ'/ϵ in the K sector, to finally unravel the thirty years old question of the origin of CP violation. In fact, since the b is the isospin partner of the very massive top quark, it shows a very rich phenomenology involving virtual t transitions; in principle, a comparative study of several b-physics phenomena, would allow to measure independently all the off-diagonal elements in the third column and third row of the Cabibbo-Kobayashi-Maskawa matrix and overconstrain them, providing a test of the unitarity of the matrix, and thus a fundamental test of the SM itself. This has led to a multiplication of proposals for b physics measurements both by

existing experiments and by *ad hoc* designed detectors and machines.

Hadroproduction of beauty is an interesting field for its own sake. Since the b is so heavy, several approximations can be made in the QCD calculations, still obtaining consistent predictions for bound state production rates in hadron-hadron interactions. At hadron colliders, the production mechanism of $b\bar{b}$ pairs can be studied, thus testing the various approximation in QCD calculations to account for the final state interaction leading to the bound state.

Hadron machines, existing nowadays, or being built, are in the very delicate situation of having a very high $b\bar{b}$ production over a huge background of hadronic events. Recent results have shown that indeed $\bar{p}p$ collider experiments can produce competitive measurements, and that exploiting the large production cross-section one can look for exclusive channels, or very rare phenomena, obtaining very clean signals, thus eluding the problem of background. This does not mean that inclusive measurements are impossible, but that, in this case, one has to face several problems connected with the hadronic nature of the colliding beams.

Mixing measurements have been for a while in the top list of b physics tasks, both because of the general interest recognized to the phenomenon, and because a time integrated mixing measurement is relatively easy, being basically a counting experiment. On the other hand their impact on the theory is not so strong, because of the large uncertainties in the parameters used to connect the observed mixing probability with more fundamental quantities (V_{CKM}). Besides, in many cases (e.g. in $\bar{p}p$), a statistical mix of b hadrons is produced, with different mixing probabilities for each type. Nonetheless a precise knowledge of the time-integrated mixing is important, e.g. as a source of tagging dilution when measuring time-independent asymmetries related to CP violation.

The measurement presented here uses muon pairs as an inclusive signature of a $B\bar{B}$ pair where both B decay semileptonically.

In general, the cleanest inclusive signature of b is from its semileptonic decay. The semileptonic branching fraction of b hadrons is of the order of ten percent, therefore a significant fraction of the b pairs produced will give at least one lepton. Since the energy spectrum of b quarks produced at $\bar{p}p$ is quite soft, leptons from b decays will have relatively low P_t and will be inside the soft hadronic jet from the rest of the b decay chain. The basic problem, in order to preserve the advantages of the high statistics in this type of measurements, is therefore the identification of (relatively) low-momentum leptons inside a jet. This is a completely different situation than, for example, at LEP, at the Z^o resonance, where one gets two 45 GeV b quarks, and therefore two 45 GeV jets, and one looks for a relatively high P_t lepton inside each jet. Besides, in $\bar{p}p$ one has in general more jets from QCD

radiation, each containing a number of soft charged particles. The large hadron multiplicity from the underlying event can be a further problem. In general, even with a very good identification technique, the misidentification probability is multiplied by factors of order 10 or more, thus giving a rate of misidentified hadrons comparable to the one from leptons. Although electrons can be faked by single π^o's, or fluctuations in the fragmentation of jets, the situation is much worse with muons, which can be faked by non-interacting punch-through hadrons, and by kaons or pions which decay in flight to a muon and a neutrino. These are in all aspects similar to real muons. This is the reason why the mixing measurement using muon pairs was not attempted at CDF with data from the 88-89 run. In general, when looking for inclusive b decay to μ+anything, the option has been to raise the P_t threshold at the price of loosing statistics. This approach is reasonable in the case of the inclusive production cross-section measurement, but much less reasonable for a mixing measurement using the muon pairs, since on top of the square of the semileptonic branching ratio, of order 10^{-2}, one cannot afford to further reduce the statistics because of a high P_t cut on both muons. It is instead highly desirable to devise a statistical method to evaluate the number of real muons after having applied only quality cuts which preserve statistics. Even though this method may not give the most accurate result, it is interesting for its own sake, and in view of any application where counting the number of real muons is important. In fact at a hadron collider the more general problem of extracting the number of real muons from a sample of candidates after a given set of quality cuts can be difficult to solve. The development of statistical techniques to extract this number over the large background due to jet and underlying event activity is important for many analyses, and for b-physics in particular.

The work presented in this thesis mainly concerns the study and development of a technique enabling us to isolate the muon pairs from $b\bar{b}$ double semileptonic decay over the large background from hadrons which fake muons in several ways. This technique is applied to the measurement of $B^0\bar{B}^0$ mixing, thus completing the scheme of mixing measurements at CDF, along with the published result obtained from the electron-muon and the electron-electron channels.

The thesis is structured in six chapters.

In the first chapter the theory of $B^0\bar{B}^0$ mixing in the framework of the Standard Model is introduced, and all the theoretically relevant quantities defined. The connection of the mixing parameters with the elements of the Cabibbo-Kobayashi-Maskawa matrix is discussed, and the current knowledge of the elements of the matrix itself and the theoretical and experimental constraints on them examined.

The second chapter is devoted to a discussion of $B^0\bar{B}^0$ mixing from an ex-

perimental viewpoint. The experimental problems and advantages at different production facilities are discussed, and then experimental methods to measure the $B^0\bar{B}^0$ mixing examined.

After a short discussion of the parts of the CDF detector relevant for the present analysis, in chapter 3, we turn in chapter 4 to a comparative summary of the old measurement of the time integrated mixing parameter $\bar{\chi}$ by the CDF collaboration, using electron-electron, and electron-muon data from the 1988-89 collider run. This introduces a discussion of the various problems involved in a measurement of $\bar{\chi}$ using dimuons, such as muon quality cuts, residual background estimates, and extraction of the mixing parameter. A review of the techniques relevant to the channel of interest and their possible application to the present measurement concludes the chapter.

In chapter 5, after examining the characteristics of the data sample, the selection cuts are discussed and studied, using Monte Carlo, in the light of the problem of evaluating the number of "real" muon pairs (as opposed to "fake" muon pairs, i.e. muon candidate pairs in which one or both the candidate muons either are not muon or have been originated far from the interaction region, by hadron decay). The method to extract the signal muon pairs over the fake background is then introduced. This relies on the different behavior of real and fake candidate muons when traversing the additional material separating the two muon systems of CDF, the central muon chambers (CMU), where they have both been identified as muons, and the central muon upgrade (CMP) in the region of overlap of the two systems. The evaluation itself is obtained solving a set of linear equations that relate the measured number of muon candidates, and whose parameters need to be measured separately on the data. The rest of the chapter is devoted to the details of these measurements, and ends with the experimental number of Like-Sign and Opposite-Sign real muon pairs as estimated from the data.

In chapter 6 the residual backgrounds from cosmic rays and Drell-Yan dimuon production are discussed and subtracted. The last step is the extraction of the mixing parameter. This involves the use of Monte Carlo to extract the fraction of dimuons from sequential b decays and of separate estimates of the number of dimuons from $c\bar{c}$ expected in the sample. Our final result $\bar{\chi} = 0.121 \pm 0.026(\text{stat.})^{+0.032}_{-0.031}(\text{sys.})$ is in agreement with the world average. The comparison to the SM constraints and the world average of χ_d is finally discussed and some conclusion is drawn.

Chapter 1

Theory

1.1 Introduction: the Standard Model

The Standard Model (SM) [1] describes the electroweak interactions of fermion fields (leptons and quarks). The interactions among these fields are dictated by the requirement of invariance under the local gauge symmetry $SU(2)_L \otimes U(1)_Y$ (weak isospin and hypercharge). The fermion fields are thus grouped in $SU(2)_L$ doublets (families) of left-handed fields, and $SU(2)_L$ singlets of right-handed fields. The currently accepted *minimal* scheme includes three families of leptons [1] and quarks:

$$\text{Leptons:} \quad \begin{pmatrix} \nu_e \\ e \end{pmatrix}_L, \quad \begin{pmatrix} \nu_\mu \\ \mu \end{pmatrix}_L, \quad \begin{pmatrix} \nu_\tau \\ \tau \end{pmatrix}_L; \quad e_R, \mu_R, \tau_R$$

$$\text{Quarks:} \quad \begin{pmatrix} u \\ d \end{pmatrix}_L, \quad \begin{pmatrix} c \\ s \end{pmatrix}_L, \quad \begin{pmatrix} t \\ b \end{pmatrix}_L; \quad u_R, d_R, c_R \ldots;$$

(right handed neutrini do not interact even weakly and are therefore unobservable).

Implementation of the local gauge symmetry requires the introduction of four massless gauge bosons: an isospin triplet ${W_\mu}^1, {W_\mu}^2, {W_\mu}^3$ for the $SU(2)_L$ (weak isospin), and an isospin singlet B_μ for $U(1)_Y$ (hypercharge). The last ingredient of the SM is a doublet of scalar fields (Higgs fields, Φ), interacting with the fermions via Yukawa coupling $\bar{f}_i f_j \Phi h_{ij}$ (where h_{ij} are the coupling constants). Giving the Higgs a nonzero vacuum expectation value spontaneously breaks the $SU(2)_L \otimes U(1)_Y$ symmetry to $U(1)_{EM}$ (the conservation of electric charge), and gives mass to the fermion and gauge boson fields (except the neutrini and photon)

[1] The number of (light) neutrino families in the SM has been established experimentally by direct measurement of invisible Z decays ($N_\nu = 2.97 \pm 0.17$) and SM fits to Z data from LEP and SLC ($N_\nu = 2.985 \pm 0.023 \pm 0.004$) [3]

via the Higgs mechanism [2]. In generating the masses of the bosons by symmetry breaking, the two neutral fields W_μ^3 and B_μ must mix in such a way that the physical states are:

$$A_\mu = B_\mu \cos\theta_W + W_\mu^3 \sin\theta_W \quad (1.1)$$
$$Z_\mu = -B_\mu \sin\theta_W + W_\mu^3 \cos\theta_W \quad (1.2)$$

ending up with a massless neutral boson A_μ (the photon), a massive neutral boson Z_μ, and a pair of massive charged bosons $W_\mu^\pm$.

The Higgs mechanism causes a kinetic-like term to appear in the Lagrangian; this term contains mass matrices for the fields involved, which depend only on the free parameters of the theory. The mass matrices of the charged leptons are diagonal because the neutrini have no right component, while quark mass matrices are non-diagonal. There is a matrix for the *up*-type quarks, and a matrix for the *down*-type quarks:

$$\begin{aligned}(m_{jk})_U &= -(h_{jk})_U \frac{v}{\sqrt{2}} \\ (m_{jk})_D &= -(h_{jk})_D \frac{v}{\sqrt{2}}\end{aligned} \quad (1.3)$$

where j and k run from 1 to 3 corresponding to the three families, h_{jk} are the Yukawa coupling constants discussed above, and v is the vacuum expectation value of the Higgs. The physical Lagrangian must be written in terms of the mass eigenstates. The two mass matrices must thus be diagonalized by means of two unitary matrices ${V_L}^{up}$, ${V_L}^{down\dagger}$, and the physical quark fields are given by:

$${u_L}^{phys} = {V_L}^{up} \begin{pmatrix} u_L \\ c_L \\ t_L \end{pmatrix}$$

$${d_L}^{phys} = {V_L}^{down} \begin{pmatrix} d_L \\ s_L \\ b_L \end{pmatrix} \quad (1.4)$$

The coupling of the fermions to the physical gauge-bosons reflects the symmetry breaking in the mixing of the weak isospin triplet of currents with the hypercharge singlet, resulting in a doublet of weak charged currents, a weak neutral current, and the electromagnetic current. The couplings to the gauge bosons $A_\mu, {W_\mu}^\pm, {Z_\mu}^0$ can finally be rewritten as the sum of three terms. The first is the coupling of the electromagnetic current to the photon:

$$J_\mu^{\text{e.m.}} A^\mu = e \sum_i \bar{f}_i \gamma_\mu Q_i f_i A^\mu \quad (1.5)$$

where Q_i is the electric charge. The second is the coupling of the weak neutral current to the Z^0:

$$J_\mu{}^{NC} Z^\mu = \frac{e}{2\sin\theta_W \cos\theta_W} \sum_i \bar{f}_i \gamma_\mu \left[(I_3(1-\gamma^5) - 2Q\sin^2\theta_W)_i \right] f_i Z^\mu \qquad (1.6)$$

where I_3 is the Pauli matrix corresponding to the third component of the weak isospin. The neutral current coupling is therefore flavour conserving. The third term is the charged current coupling which has the form:

$$J_\mu^{CC} W^\mu + C.C.$$

corresponding to the combinations I_+, I_- of the first two components of the weak isospin triplet. In the leptonic sector the charged current has the simple form:

$$J_\mu^{CC} = \bar{\ell}_i \gamma_\mu (1-\gamma_5) \nu_{\ell,i}$$

coupling the left-handed components only. Leptons are not mixed since one has always the freedom to redefine the neutrino to be massless. In the quark sector instead:

$$J_\mu{}^{CC} = (\bar{u}, \bar{c}, \bar{t})_L \gamma_\mu V_{CKM} \begin{pmatrix} d \\ s \\ b \end{pmatrix}_L \quad J_\mu^{CC\dagger} = (\bar{d}, \bar{s}, \bar{b})_L V_{CKM}^\dagger \gamma_\mu \begin{pmatrix} u \\ c \\ t \end{pmatrix}_L \qquad (1.7)$$

gives a charged current interaction which is a) flavour nonconserving, and b) non diagonal if $V_{CKM} \equiv V_L{}^{up} V_L{}^{down\dagger}$ is non diagonal.

The $V-A$ structure of the charged current violates the charge conjugation symmetry C and the parity P maximally, while conserving electric charge, baryon- and lepton-number separately and exactly. It may violate CP if V_{CKM} contains a non-trivial phase (i.e. a phase which can not be eliminated by rearranging the phases of the fields).

1.1.1 The quark mixing matrix

V_{CKM}, the Cabibbo-Kobayashi-Maskawa matrix, is a 3×3 unitary matrix in the flavour space which was first introduced to explain CP violation in the K sector [4], and is an extension of the GIM mechanism [5] to three families.

$$V_{CKM} \equiv \begin{pmatrix} V_{ud} & V_{us} & V_{ub} \\ V_{cd} & V_{cs} & V_{cb} \\ V_{td} & V_{ts} & V_{tb} \end{pmatrix}$$

The introduction of the third family was necessary to have a physical phase in the matrix parameters: a unitary $n \times n$ matrix has $n(n-1)/2$ independent angle

and $(n-1)(n-2)/2$ independent phase parameters, so that for $n=2$ we have zero phases, whereas for $n=3$ we have one physical phase. The elements of V_{CKM} depend on the Yukawa couplings of the Higgs to the fermion fields, which are arbitrary complex numbers in the SM, through the mass matrices. The link between the V_{CKM} elements and the mass matrices is discussed in deep in ref. [6].

The elements of the matrix are determined experimentally from processes involving the charged current coupling of the quarks to the $W^{\pm}$ bosons. The four elements which only involve u, d, c, s quarks are functions of the Cabibbo angle θ_c; they form an independent square 2×2 unitary matrix. V_{ub} and V_{cb} can be directly measured from B-meson decays. The remaining three elements, involving the top quark, are only indirectly accessible in B-decays through virtual transitions, such as $B^0\bar{B}^0$ mixing. The five elements of V_{CKM} which involve heavy quarks (b or t), as well as the CP violating phase, are all in principle measurable through precision experiments on B-decays.

1.1.2 Wolfenstein (approximate) parameterization of V_{CKM}

The CKM matrix can be parameterized in several manners, depending on how the relative phases of the various fields are chosen. Of course these phases are not physical observables and therefore all the parameterization must be equivalent. The original KM parameterization was based on the rotation matrices in the flavour space involving three angles and a phase, where one of the angles was the Cabibbo angle θ_C. Approximate representations are also widely used, originally motivated by the scarce knowledge on some of the elements and by the need to exploit unitarity. A popular and useful one is due to Wolfenstein [8] and is based on the empirical observation (see below) that:

$$\begin{aligned} |V_{ud}| &\simeq |V_{cs}| \simeq |V_{tb}| \simeq 1 \\ |V_{us}| &\simeq |V_{cd}| \sim \lambda \\ |V_{cb}| &\simeq |V_{ts}| \sim \lambda^2 \\ |V_{ub}| &, \quad |V_{td}| \sim \lambda^3 \end{aligned} \tag{1.8}$$

(1.9)

where $\lambda \equiv \sin\theta_c \simeq 0.22$. Lets first consider the 2×2 submatrix spanned by the $(u,d),(c,s)$ doublets in

$$V_W \sim \begin{pmatrix} 1-\frac{1}{2}\lambda^2 & \lambda & \cdot \\ -\lambda & 1-\frac{1}{2}\lambda^2 & \cdot \\ \cdot & \cdot & 1 \end{pmatrix} \tag{1.10}$$

obtained taking all three diagonal elements to be real. $V_{cd} \simeq -\lambda$ is dictated by consistency with the observation that the physical u and c charge-changing transitions are of the form $u \leftrightarrow d\cos\theta_c + s\sin\theta_c$ and $c \leftrightarrow -d\sin\theta_c + s\cos\theta_c$. V_{cd} is accidentally nearly real due to the smallness of the remaining elements in the third column and third row, therefore the 2×2 square matrix in (1.10) is not only unitary but also orthogonal. We have the freedom to choose one more term, V_{cb}, to be real; it is proportional to λ^2 so we introduce a new parameter A. Unitarity then fixes V_{ts}. The remaining terms, of order λ^3, having both non-trivial phases, impose the introduction of two new parameters, ρ and η. This gives the following "perturbative" form of the CKM matrix:

$$V_W = \begin{pmatrix} 1-\frac{1}{2}\lambda^2 & \lambda & A\lambda^3(\rho - i\eta) \\ -\lambda & 1-\frac{1}{2}\lambda^2 & A\lambda^2 \\ A\lambda^3(1-\rho-i\eta) & -A\lambda^2 & 1 \end{pmatrix} + \mathcal{O}(\lambda^4) \qquad (1.11)$$

The Wolfenstein parameterization expresses well the similarity of V_{CKM} to a unity matrix, the main charged current contributions in the standard model being from $u \leftrightarrow d$, $c \leftrightarrow s$, and $t \leftrightarrow b$. The current best estimates of the modules of elements of V_{CKM} are [9]:

- from a comparison of muon decay and nuclear beta-decay:

$$|V_{ud}| = 0.9744 \pm 0.0010;$$

- from the decays of charmed particles:

$$|V_{cs}| = 1.02 \pm 0.18;$$

- from unitarity, assuming three families (top observations are consistent with $\mathrm{BR}(t \to b) \simeq 100\%$):

$$|V_{tb}| = 0.9915 \pm 0.002;$$

- from strange particle decays:

$$|V_{us}| \equiv \lambda = 0.2196 \pm 0.0023;$$

- from neutrino production of charm and successive decay to nonstrange final states:

$$|V_{cd}| \simeq \lambda = 0.204 \pm 0.017;$$

The magnitude of the remaining elements, V_{ub}, V_{cb}, V_{ts} and V_{td} are discussed below.

Figure 1.1: Unitarity triangle for CKM elements. a) the relation (1.13) in the complex plane; b) the triangle "normalized" to $A\lambda^3$ in the Wolfenstein parameterization. Angles α,β,γ follow the usual convention.

physics; one of the goals of beauty physics is to overconstrain it. We now examine the current knowledge on its parameters, completing the list of current experimental data on the CKM matrix elements.

- V_{cb} has been determined from the partial width of the semileptonic decays $B \to X(c) + \ell\bar{\nu}_\ell$ and from the exclusive decays $B \to D^* \ell\bar{\nu}_\ell$. In the first case the partial width is assumed to be that of a b-quark; this method depends

critically on the choice of the mass of the b quark and relies on the use of the quark model to describe B hadron decay. The extraction from exclusive decay data is independent from m_b and suffers mainly from statistical error. The two values of V_{cb} are consistent with similar uncertainties around $\pm 12\%$:

$$V_{cb} = 0.040 \pm 0.005 \tag{1.14}$$

from D^* and

$$|V_{cb}| = (0.042 \pm 0.001 \pm 0.004)\sqrt{\frac{1.49}{\tau_B(ps)}} \tag{1.15}$$

Since $V_{cb} = A\lambda^2$ it results:

$$A = 0.823 \pm 0.10 \tag{1.16}$$

- The ratio $|V_{ub}/V_{cb}|$ can be determined from the semileptonic decay of B mesons produced at the $\Upsilon(4S)$. Due to the dominance of the $b \leftrightarrow c$ coupling the semileptonic decay of a B meson to non-charmed states is rare in comparison to decays to $D + X$. By measuring the p_t spectrum of leptons above the $b \to c\ell\nu$ endpoint the $b \to u\ell\nu$ rate is obtained by subtraction of continuum background. Continuum background determination and theoretical models for the signal spectrum are the main sources of error here. From the whole set of measurements

$$|V_{ub}|/|V_{cb}| = 0.08 \pm 0.02.$$

- $V_{tb}V_{td}^*$ can be measured from mixing (an independent determination of V_{td} is also possible from rare decays). The most accurate estimate comes from mixing measurements at the $\Upsilon(4S)$, and depends on hadronic matrix elements for the virtual (box) transitions, and on the top quark mass. Connections of mixing to this parameter will be discussed at length in the next sections.

- $V_{tb}V_{ts}$ can also, in principle, be measured from $B_s\bar{B}_s$ mixing, although no direct observation as been made as yet. This item is discussed more extensively later in this chapter and in the next one.

1.2 Mixing - General Formalism

From the formal theory of scattering it is possible to show that if a system is described by the Hamiltonian $H = H_0 + H_I$ and $|\chi_\alpha>$ are discrete eigenstates of

the *free* Hamiltonian H_0 which decay due to H_I, then evolving at time t an initial state $|\chi_\alpha>$ and projecting it on the Hilbert subspace spanned by the $|\chi_\alpha>$ we obtain:

$$e^{-i(E_\alpha+M)t-\frac{1}{2}\Gamma t}|\chi_\alpha> \tag{1.17}$$

Where M and Γ are hermitian matrices and Γ is also positive definite.

Since the time-evolution operator is not necessarily diagonal in (1.17), transitions between the undecayed states $|\chi_\alpha>$ are possible through the action of this operator.

The derivation of (1.17) can be outlined as follows: the probability amplitude that a system which is in a state α at time $t = 0$ be still in an undecayed state α' at time t is given by

$$A_{\alpha\alpha'} = \left[e^{-iP\bar{R}P}\right]_{\alpha\alpha'} \tag{1.18}$$

i.e. the matrix element between the two states of the operator enclosed in parentheses, where P is the projection operator over the Hilbert subspace spanned by the $|\chi_\alpha>$, R is an operator defined by the equality

$$P\frac{1}{E-H+i\epsilon}P = \frac{1}{E-PH_0P-PR(E)P} \tag{1.19}$$

and $\bar{R} = R(\bar{E})$ is the operator R evaluated in the poles of (1.19). From (1.18) it is immediate that $P\bar{R}P$ can be regarded as an effective hamiltonian on the states $|\chi_\alpha>$. The matrix $PH_0P + P\bar{R}P$ is called the *mass matrix* of the system; it can be shown that $P\bar{R}P$ can be written as $M - i\Gamma/2$, with the characteristics stated above, hence equation (1.17).

States that diagonalize $M-i\Gamma/2$ are states with definite mass and lifetime. If, as is the case for the $B^0\bar{B}^0$ system, the decaying states are a particle-antiparticle pair degenerate under $H_0 = H_{strong}$ then the mass matrix may have non-diagonal terms which mix the two degenerate states. In general if α and $\bar{\alpha}$ are two degenerate states the time evoluted of a system being in the state α at $t = 0$ will be a linear combination of α and $\bar{\alpha}$, and equation (1.17) can be rewritten in the equivalent form:

$$i\partial_t \begin{pmatrix} \alpha \\ \bar{\alpha} \end{pmatrix} = H \begin{pmatrix} \alpha \\ \bar{\alpha} \end{pmatrix} = \begin{pmatrix} M - \frac{1}{2}i\Gamma & M_{12} - \frac{1}{2}i\Gamma_{12} \\ {M_{12}}^* - \frac{1}{2}i{\Gamma_{12}}^* & M - \frac{1}{2}i\Gamma \end{pmatrix} \begin{pmatrix} \alpha \\ \bar{\alpha} \end{pmatrix} \tag{1.20}$$

where H is the effective "Hamiltonian" and the equality of the diagonal terms comes from CPT invariance. Diagonal terms describe the free evolution (M) and, respectively, the decay of the particle (Γ), M and Γ being the mass and the decay width of the two degenerate eigenstates of H_0. Off diagonal elements are responsible for $\alpha\bar{\alpha}$ transitions: the real part M_{12} corresponds to virtual transitions

while the imaginary part corresponds to "decay" transitions, i.e. transitions proceeding on the mass-shell.

The α,$\bar{\alpha}$ states are the eigenstates of the *unperturbed* Hamiltonian H_0. If H_0 preserves a certain symmetry, then it is possible to write linear combinations of those states which still diagonalize H_0 and that symmetry. The introduction of the interaction Hamiltonian H_I, responsible for the metastability of those states may or may not preserve that symmetry. To be specific let's take the combined charge-parity transformation CP; then, if we assume CP $\alpha = \bar{\alpha}$ the combinations:

$$\frac{\alpha + \bar{\alpha}}{\sqrt{2}}$$

$$\frac{\alpha - \bar{\alpha}}{\sqrt{2}}$$

have respectively CP $= 1$ and -1. If the interaction Hamiltonian H_I violates CP then the mass eigenstates will also "violate" CP i.e. they will mix the CP-even and CP-odd combinations. Let's call this states α_1 and α_2, respectively with masses M_1 and M_2 and decay widths Γ_1 and Γ_2; they are conveniently expressed as:

$$\alpha_1 = \frac{(1+\epsilon)\alpha + (1-\epsilon)\bar{\alpha}}{\sqrt{2(1+|\epsilon|^2)}} \tag{1.21}$$

$$\alpha_2 = \frac{(1+\epsilon)\alpha - (1-\epsilon)\bar{\alpha}}{\sqrt{2(1+|\epsilon|^2)}} \tag{1.22}$$

The amount of CP violation is determined by the complex parameter ϵ, and $\epsilon = 0$ corresponds to CP conservation, α_1 α_2 being CP eigenstates.

Given a system in a pure α state at time $t = 0$ the probabilities of it decaying as an α or $\bar{\alpha}$ at time t, $W_\alpha(t)$ and $W_{\bar{\alpha}}(t)$, neglecting CP violation effects, are:

$$W_\alpha(t) = \frac{1}{4}\left[e^{-\Gamma_1 t} + e^{-\Gamma_2 t} + 2e^{-\Gamma t}\cos\Delta M t\right] \tag{1.23}$$

$$W_{\bar{\alpha}}(t) = \frac{1}{4}\left[e^{-\Gamma_1 t} + e^{-\Gamma_2 t} - 2e^{-\Gamma t}\cos\Delta M t\right] \tag{1.24}$$

Where ΔM is the mass difference of the mass eigenstates, α_1 and α_2, and $\Delta\Gamma$ the difference of the widths. These are related to M_{12}, Γ_{12} by

$$\Delta M = 2Re\sqrt{(M_{12} - i\frac{\Gamma_{12}}{2})(M_{12}{}^* - i\frac{\Gamma_{12}{}^*}{2})}$$

$$\Delta\Gamma = -4Im\sqrt{(M_{12} - i\frac{\Gamma_{12}}{2})(M_{12}{}^* - i\frac{\Gamma_{12}{}^*}{2})}$$

The time-integrals of (1.23, 1.24) give the relative "unmixed" ($N(\alpha)$) and, respectively "mixed" ($N(\bar{\alpha})$) decay rates as functions of ΔM, Γ and $\Delta\Gamma$; a parameter which will be relevant in the following discussion is the ratio r of mixed to unmixed events:

$$r = \frac{N(\bar{\alpha})}{N(\alpha)} = \frac{(\Delta M)^2 + (\Delta\Gamma/2)^2}{2\Gamma^2 + (\Delta M)^2 - (\Delta\Gamma/2)^2} \tag{1.25}$$

By definition (1.25) $r = 0$ corresponds to no mixing, while $r = 1$ corresponds to *complete* mixing. The integral probability of mixing χ, that is, the ratio of the number of "mixed" decays to the total number of decays ("mixed" and "unmixed") is then

$$\chi = \frac{N(\bar{\alpha})}{N(\alpha) + N(\bar{\alpha})} = \frac{r}{1+r} = \frac{\Delta M^2 + (\Delta\Gamma/2)^2}{2(\Gamma^2 + \Delta M^2)} \tag{1.26}$$

1.3 Mixing in the $B^0\bar{B}^0$ system

The values of ΔM and $\Delta\Gamma$ can be computed in perturbation theory. For the $B^0\bar{B}^0$ system ΔM and $\Delta\Gamma$ result from the "box" diagrams in fig. 1.2. ΔM corresponds to the dispersion part, while $\Delta\Gamma$ corresponds to the absorption part, i.e., it corresponds to the cases where the intermediate (virtual) particles are nearly on the mass shell (the imaginary part of the operator in (1.19)). These in turn correspond to common decay channels of the particle and antiparticle. In the case of $K^0\bar{K}^0$ these common decay channels involve transitions of the same order as for the real part while for the $B^0\bar{B}^0$ a factor of order $\sin^2\theta_c$ appears, which suppresses this common decays (Cabibbo-suppression). Consequently common decay channel of $B^0\bar{B}^0$ have branching ratios of $\mathcal{O}(10^{-3})$. Furthermore contributions are of both signs. For this reasons while in the $K^0\bar{K}^0$ case we have $\Delta\Gamma \sim \Delta M$ in the $B^0\bar{B}^0$ we have $\Delta\Gamma \approx 0$, yielding:

$$r \simeq \frac{x_d^2}{2 + x_d^2} \tag{1.27}$$

$$\chi \simeq \frac{x_d^2}{2(1 + x_d^2)} \tag{1.28}$$

where $x_d = \frac{\Delta M}{\Gamma}$. The theoretical prediction for ΔM can be obtained by computing the box diagrams in fig. 1.2; the result is:

$$\Delta M \approx 2M_{12} = \frac{{G_F}^2 {M_W}^2}{8\pi^2} < \bar{B_d}^0 | j_\mu^{V-A} j^\mu_{V-A} | {B_d}^0 > \sum_{u,c,t} \lambda_i \lambda_j A_{ij} \tag{1.29}$$

where the parameters λ_i,λ_j contain the dependance from the CKM matrix elements ($\lambda_i = {V_{ib}}^* V_{id}$). The functions A_{ij} are obtained from loop integrals and

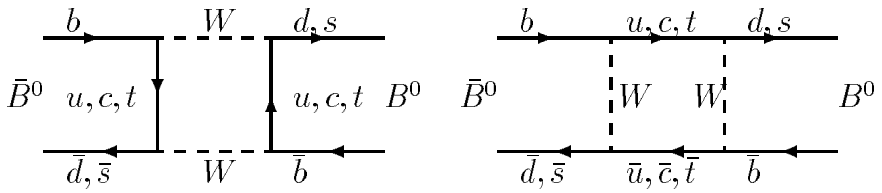

Figure 1.2: The two box diagrams contributing to $B^0\bar{B}^0$ mixing.

depend on quark masses, the most important contribution coming from the tt term [11], and thus the final expression for ΔM is proportional to $|V_{tb}{}^*V_{td}|^2$ as is the mixing parameter r. The matrix element $< \bar{B_d}{}^0|j_\mu^{V-A} j^\mu_{V-A}|B_d{}^0 >$ is the probability of finding the $\bar{b}d$ quarks ($b\bar{d}$) close together in the B^0 ($\bar{B}^0$), where $j_\mu^{V-A} = \bar{b}\gamma_\mu(1-\gamma_5)d$; using the vacuum insertion approximation:

$$< \bar{B_d}{}^0|j_\mu^{V-A} j^\mu_{V-A}|B_d{}^0 >= B_B < \bar{B}^0|j_\mu j^\mu|0 >< 0|j_\mu j^\mu|B^0 >= B_B \frac{4}{3} f_B^2 m_b \quad (1.30)$$

Where the "bag" parameter B_B describes how good the vacuum insertion approximation is. Due to the heaviness of the b quark, B_B is estimated to be ~ 1. The decay constant f_B is defined by:

$$< 0|J^\mu|B(q) >= iq^\mu f_B$$

in analogy with the pion decay constant. It is a parameter of a quark bound state and therefore cannot be evaluated perturbatively. QCD sum rules give estimates of $f_B \approx 140$ MeV, while lattice calculations yield $f_B \approx 200 - 300$ MeV [26].

Putting everything together the mixing parameter can then be predicted to be:

$$x_d \simeq \frac{{G_F}^2}{6\pi^2} B_B {f_B}^2 m_b \frac{\tau_b}{\hbar} |V_{tb}{}^* V_{td}|^2 {M_W}^2 S\left(\frac{{m_t}^2}{{M_W}^2}\right) \eta_{qcd} \quad (1.31)$$

In this equation we have used the average lifetime over all B hadrons, τ_b in place of the B_d^0 lifetime, since up to now no measurement of the lifetime from exclusive decays exist due to the low statistics. Perturbative QCD corrections to the box diagrams calculation are factorized and kept into account by η_{QCD}, while S is a slowly varying function of m_t^2/M_W^2:

$$S(x) \equiv \frac{x}{4}\left[1 + \frac{3-9x}{(x-1)^2} + \frac{6x^2 \ln x}{(x-1)^3}\right] \quad (1.32)$$

1.3.1 Measurements and constraints on x_d

Unitarity condition on the absolute value $|V_{td}|$ gives $0.002 < |V_{td}| < 0.007$ [13]; on $|V_{tb}|$ gives $0.9985 < |V_{tb}| < 0.9995$; we can insert these bounds into the result

from previous section which assumes SM. A partial list of the current knowledge on the relevant parameters in (1.31) is:

- the mass of the top quark $m_t = 176 \pm 8 \pm 10$ GeV/c^2 from direct observation of candidate events in $\bar{p}p$ annihilations [12]. There is also an indirect estimate from electroweak data [10] $m_t = 164^{+17+18}_{-16-20}$ GeV/c^2;
- the factor $\sqrt{B_B} f_B$ is estimated from $1/N_c$ expansions and lattice calculations; we use $f_B = 140 \pm 25$ MeV, and $B_B = 0.85 \pm 0.10$
- for the QCD correction factor current estimates give $\eta_{QCD} = 0.85$ [14];
- the most recent world average gives $\tau_b = (1.54 \pm 0.04) \cdot 10^{-12}$

Using these values, the current theoretical estimate of x_d is:

$$0.012 < x_d < 0.61 \tag{1.33}$$

Conversely, inserting mixing results and the parameters above into (1.31) one can extract information on the unitarity triangle from mixing measurements.

1.3.2 Combined measurements of x_s/x_d

A calculation analogous to the one in section 1.3 for the B_s mixing parameter x_s is based on the same box diagrams of fig. 1.2. It yields:

$$x_s \approx x_d \left| \frac{V_{ts}}{V_{td}} \right|^2 \tag{1.34}$$

A lower limit on x_s can be obtained by inserting into (1.34) the lower bound on V_{ts} and the upper bound on V_{td} from unitarity; an upper limit is set by considering experimental lower limits on V_{td} and the upper limit on V_{ts} from unitarity. The value of x_s is thus bracketed within

$$3 < x_s < 18 \tag{1.35}$$

Equation (1.34) and the fact that $V_{ts} \approx V_{cb}$ (see § 1.1, eqs. (1.12, 1.13) suggest that measuring x_s would give an estimate of V_{td} free of the uncertainties on m_t, on the QCD corrections and on the non perturbative factor $\sqrt{B_B} f_B$. The feasibility of such measurements will be discussed further in § 2.3.

1.3.3 Constraints on the unitary triangle from mixing and CP violation

Using experimental results on B decays, $B^0\bar{B}^0$ mixing, and CP violation it is possible to set limits on the position of the α vertex of the unitarity triangle (see fig. 1.1).

The value of $|V_{ub}/V_{cb}| = 0.08 \pm 0.02$ quoted in § 1.1.2, bounds a semi-circular segment centered in the origin of the (ρ, η) plane through the relation:

$$|V_{ub}/V_{cb}| = \lambda\sqrt{\rho^2 + \eta^2}. \tag{1.36}$$

The two boundaries from this equation are the dashed semi-circles in fig. 1.3, the allowed region being between the two.

The x_d value from $B^0\bar{B}^0$ mixing can be inserted in eq. (1.31) to obtain an allowed region in the (ρ, η) plane; the parameter $\sqrt{B_B} f_B$ is varied within its range (100-300 MeV), we take $\eta_B = 0.85 \pm 0.05$ and $\tau_B = (1.50 \pm 0.11) \cdot 10^{-12}$ s. The limiting values inserted in (1.31) bound a circular segment centered at $(1, 0)$ in (ρ, η), indicated by the solid curves in fig. 1.3.

Finally, the CP violation parameter module $|\epsilon|$ in $K^0\bar{K}^0$ is connected to the CKM parameters through the following expression:

$$|\epsilon| = 4.33 A^2 B_K \eta [\eta_3 S(x_c, x_t) - \eta_1 S(x_c) + \eta_2 A^2 \lambda^4 (1 - \rho) S(x_t)] \tag{1.37}$$

where $x_i = m_i^2/M_W^2$; η_j are QCD corrections and

$$S(x, y) = xy \left\{ \left[\frac{1}{4} + \frac{3}{2(1-y)} - \frac{3}{4(1-y)^2} \right] \frac{\ln y}{y - x} + (y \leftrightarrow x) - \frac{3}{4(1-x)(1-y)} \right\}. \tag{1.38}$$

Exploiting the most recent measurements of $|\epsilon|$ the hyperbolic boundaries shown in fig. 1.3 (dot-dashed lines) are obtained; here the values $f_K = 160$ MeV, $B_K = 2/3 \pm 1/6$, and the QCD correction coefficients $\eta_1 = 0.85$, $\eta_2 = 0.61$, and $\eta_3 = 0.36$ are used. We have used a more precise approximation than the one in (1.12) for the CKM matrix elements and the value of the parameter A from eq. (1.16).

Figure 1.3 shows all the information bounding the position of the α vertex of the unitarity triangle.

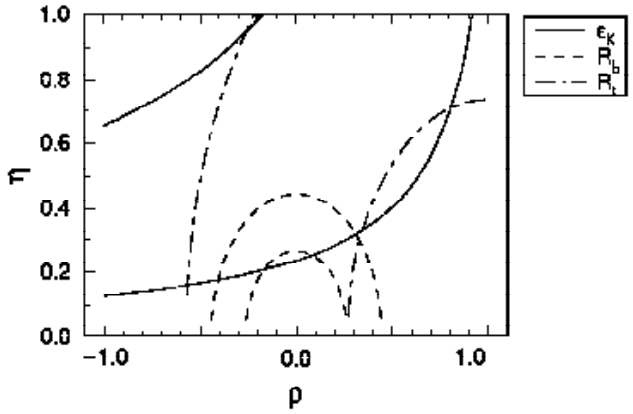

Figure 1.3: Boundaries in the (ρ, η) plane from B mixing (solid), V_{ub}/V_{td} measurements (dashed), and measurements of $|\epsilon|$, the $K^0\bar{K}^0$ CP violation parameter module (dot-dash); the allowed region is the intersection of the regions bounded by each pair of curves.

Chapter 2

Experimental Scenario

2.1 B-meson production and decay

Due to the relatively large mass of the b quark, B meson decays are well described by the so called "spectator model", in which the heavy quark decays independently into a virtual W-boson and a c or u quark (fig. 2.1) , the dominant decay being to charm. The virtual W boson can then decay either to a quark pair (hadronic modes) or to a lepton-neutrino (leptonic modes). The corresponding decays of B mesons are called nonleptonic ($W \rightarrow$ hadrons) and semileptonic, respectively. The main characteristics of the decays are:

- a relatively large lifetime. The average lifetime of B hadrons is $1.537 \pm 0.021 \cdot 10^{-12} s$ [15], which corresponds to $c\tau \simeq 400 \mu m$. This means it takes a measurable length for a B meson to decay. In fact secondary vertices with displacements of several hundreds of microns can be expected already at the PEP and PETRA e^+e^-colliders at $\sqrt{s} = 29$ GeV from the decay of b-hadrons with average $\gamma\beta \sim 2$;

- a relevant fraction of them contain a lepton. The branching fraction of the decay $B \rightarrow \ell\nu_\ell + X$ is about 20 % to either electron or muon. Since the virtuality of the W boson is of order the b mass, the lepton from b-decay is expected to have a relatively large momentum;

- a charmed hadron is expected in the decay products. It is possible to exploit the decay products of the charmed meson itself as a signature of the b.

2.1.1 B meson production facilities

B mesons can at present be produced and studied at several different kinds of facilities, each having its advantages and its drawbacks. The main distinction

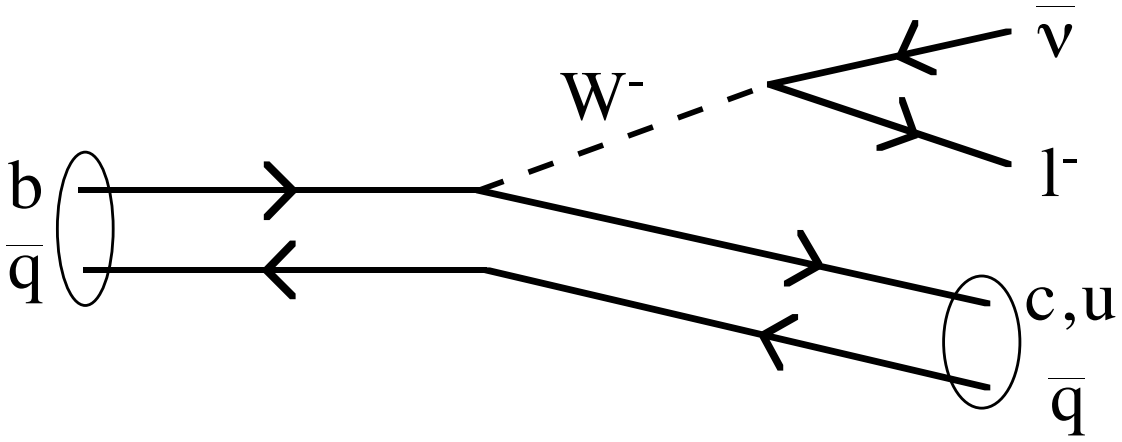

Figure 2.1: The diagram for the decay of a B meson in the spectator model

can be made between "near threshold" production at e^+e^-, and "continuum" or resonant (at the Z^0 peak) production at e^+e^-or hadron machines

2.1.2 "Near threshold" production

The threshold for the production of b-flavoured mesons (open flavour, $B = \pm 1$, as opposed to the hidden flavour of the Υ, a $b\bar{b}$ bound state with $B = 0$), is a little below the $\Upsilon(4S)$ mass, and thus experimenters working at the resonant energy $\sqrt{s} = M_{\Upsilon(4S)}$ profit of a relatively large cross-section. e^+e^-machines working near threshold for open flavour production (DORIS-II, CESR) yield B mesons as decay products of the $\Upsilon(4S)$; they are characterized by very clean events which are quite easy to reconstruct and study. The main background from hadronic "continuum" events is relatively easy to deal with because it has a jet-like topology, while B decays are nearly spherical, since the B's are produced almost at rest. Alternatively one can concentrate on exclusive decays and apply kinematical constraints to attain high levels of sample purity. Notice that when working at the $\Upsilon(4S)$ mass, this colliders cannot produce B_s or B_c mesons.

Near threshold machines are particularly suitable to study B-meson decays and branching ratios, both exclusive and inclusive, but they are unsuitable to study lifetimes because B^0 's from Υ decay at the point of production. To overcome this problem asymmetric beam B factories have been proposed and are under study and first stages of project. These colliders will have electron and positron beams with different energies in order to obtain "near threshold" E_{cm} and a longitudinal kick apt to produce measurable decay lengths. This method,

combining the advantages of higher E_{cm} with the high cross-section and cleanness of $\Upsilon(4S)$ machines promises to give relevant results in the future, when one can envisage precision CP violation measurements with high statistics runs of this colliders.

2.1.3 "Continuum" machines

e^+e^-machines in the continuum (PEP, PETRA, TRISTAN) suffered from a very small cross section for open b-flavour production (of order 0.03–0.04 nb, to be compared to the 1.15 nb at the $\Upsilon(4S)$); on the other side the few B-mesons produced have transverse momenta which allow them to cover non-negligible distances prior to the decay. This makes it possible to measure decay distances and therefore the B lifetime. The drawback is that the event topology is much less different between signal and background than in near threshold production, and other methods must be devised to "tag" the B-decay. One of the most used methods is to look for high transverse momentum[1] leptons, which are signature for a semileptonic B-decay. Thus a very pure sample can be obtained at the price of loosing statistics due to the small branching fraction, the p_t cut, and the acceptance of the detector for electrons and muons.

2.1.4 Z^0 peak colliders

Colliders at the Z^0 peak (LEP, SLC) share with "continuum" machines the problems of background rejection, while benefitting from a cross-section (7 nb) two orders of magnitude larger, which makes statistically-inefficient techniques more feasible. With the installation in many of these experiments of precision vertex detectors it has become possible to measure the B lifetime with great precision, and make the first direct observation of the time dependence of mixing (see later).

2.1.5 Hadron Colliders

Hadronic machines have a very high cross section for $b\bar{b}$ production, which is of order of 50 μb for the Tevatron collider, at $\sqrt{s} = 1800$ GeV. This means that at the current luminosity ($\geq 5 \cdot 10^{30}\ cm^{-2}s^{-1}$) about 500,000 $b\bar{b}$ events per day are produced at CDF. This has to be compared to the 1,000–2,000 events/day of LEP experiments, working at the Z^0 resonance, or the 7000–8000 events/day at CESR. On the other side the fraction of hadronic events containing a $b\bar{b}$ pair is $\sim 7 \cdot 10^{-4}$ at the Tevatron, with respect to 0.215 at LEP and 0.25 at CESR, which makes B^0

[1] The transverse momentum is measured with respect to the jet axis

identification harder at the Tevatron. Given the huge production cross section, though, it is affordable to attempt full reconstruction of peculiar signatures, such as rare decays of B-mesons, and to deal with small tagging efficiency. Another issue concerns the production angle distribution of beauty events, since at $\bar{p}p$ they are produced in a relatively wide rapidity interval and show no appreciable peaking in the central region, and this rapidity interval gets wider with increasing center-of-mass energy ($\sqrt{s}$). General purpose detectors, like CDF, only cover the central rapidity region ($|y| < 1.$), and this greatly reduces the efficiency for beauty events. On the other side it is not clear if extending detector acceptances down to small polar angles (of order $\theta \sim 500mr - 1^0$) would help, since at $\bar{p}p$ this region shows a lot of activity from the *underlying event* and other "low-x" phenomena. Disentangling b-flavoured particles signatures in this environment would probably be a formidable task even with the most sophisticated techniques available.

2.2 Mixing measurements

There are two possible ways of detecting mixing effects in the decay of B mesons.

One is to observe *time dependent* mixing effects, i.e. to observe the oscillations in the probabilities of eqs. (1.23, 1.24) as a function of the B meson proper time. In this case it is interesting to notice that: a) B mesons are produced in pairs: the quantum state in which the pair is produced is relevant; b) the experimental apparatus must have the resolution necessary to measure the expected decay lengths.

The other way is to disregard the evolution of the system and try to detect the overall effect of the mixing in the relative decay rates, eq. (1.25), i.e. make a *time integrated* measurement. In this work the latter approach will be used, therefore we will not discuss further the time dependent measurements.

2.2.1 Mixing at the $\Upsilon(4S)$

Experimentally, one measures the ratio of "mixed" to "unmixed" pairs, which is often indicated with R. The relation between R and r (which is the ratio of mixed to unmixed decays) depends on the quantum state in which the pair is generated.

In the decay $\Upsilon(4S) \to B_d^0 \bar{B}_d^0$ the pair is produced coherently, with relative orbital momentum $l = 1$ and in a state with $C = -1$. This happens because the 2-particle wave function with odd relative angular momentum is antisymmetric under particle exchange and thus the system is in a pure $B^0\bar{B}^0$ state until one of the particles decays. If at a given time one particle decays as a B^0 then at

the same time the other particle is in a pure $\bar{B}^0$ state; then the latter evolves as a one-particle system. For $B_d\bar{B}_d$ at the $\Upsilon(4S)$, therefore, R and r are exactly equal, because of the coherence of the state. One can conveniently obtain χ as the ratio of events that mixed to all events containing a $b\bar{b}$ quark pair, i.e. the integral probability of mixing:

$$\chi = \frac{N_{BB} + N_{\bar{B}\bar{B}}}{N_{b\bar{b}}} = \frac{r}{1+r} \tag{2.1}$$

where $N_{b\bar{b}}$ indicates the total number of beauty quark-antiquark pair.

The study of fully reconstructed exclusive decays at ARGUS and CLEO has led to the first observation of B^0 mixing. Although reconstruction efficiencies are tiny the high natural signal-to-noise ratio at the $\Upsilon(4S)$ make this the easiest way to detect mixing. Although any tagging techniques involving identification of some of the decay products (such as leptons) suffer here of the low statistics and have some background contamination due to the small momenta involved, nonetheless the measurement of χ_d, the *time integrated* mixing probability of B^0 mesons, by CLEO at CESR and ARGUS at DORIS [19] is currently the best measurement of mixing in the b sector. The two collaborations have measured mixing of the $B^0\bar{B}^0$ pairs using two methods. The first, less efficient, consists in looking for fully reconstructed B^0 's and then tag the other B from its semileptonic decay. The best reconstruction channel is $B^0 \to D^*\ell^+\nu_\ell$. In this case

$$r = \frac{N(\bar{B}^0\ell^-) + N(B^0\ell^+)}{N(\bar{B}^0\ell^+) + N(B^0\ell^-)}$$

although statistically limited, this method is almost free of systematic uncertainties.

The second method relies completely on the lepton-tagging for both B^0 decays. Besides the subtraction of the backgrounds due to lepton pair production, to extract the mixing parameter r one must take into account contributions from $\Upsilon(4S) \to B^+B^- \to \ell^+\ell^- + X$ decays; the factor

$$\lambda = f^+/f^- \left(\frac{\tau_{B^+}}{\tau_{B^0}}\right)^2$$

containing the ratio of the charged to neutral branching fractions, and entering the final formula for r:

$$r = \frac{N_{\ell\pm\ell\pm}(1+\lambda)}{N_{\ell^+\ell^-} - N_{\ell\pm\ell\pm}\lambda}$$

is the main source of systematic error on r.

Results from the two methods are in good agreement (table 2.1) and from them an average value $x_d = 0.71 \pm 0.06$ is obtained.

Experiment	χ_d
ARGUS: $B^0 (\to D^* \to \pi + X) + \ell^\pm$	$0.16 \pm 0.04 \pm 0.04$
CLEO2: $B^0 (\to D^* \to \pi + X) + \ell^\pm$	$0.149 \pm 0.023 \pm 0.022$
ARGUS: (leptons)	0.171 ± 0.048
World average:	0.156 ± 0.024

Table 2.1: Values of the B_d mixing parameter measured at the two experiments at CESR.

2.2.2 Mixing outside the $\Upsilon(4S)$

Outside the resonant region, $B^0\bar{B}^0$ pairs are produced incoherently from the (almost) independent fragmentation and hadronization of a $b\bar{b}$ pair produced in the annihilation of e^+e^-or the quark-quark or gluon-gluon scattering. In this case the relation between R and r is:

$$R = \frac{2r}{1+r^2} \tag{2.2}$$

The ambiguity in extracting r from the experimental value R is only apparent, since the relation between R and χ:

$$R = \frac{2\chi(1-\chi)}{\chi^2 + (1-\chi^2)} \tag{2.3}$$

is symmetric for the exchange $\chi \leftrightarrow (1-\chi)$, and the two solutions cannot be distinguished experimentally.

Using lepton tagging the sample will also be a mixture of events containing a B_d ($\bar{B}_d$) or B_s ($\bar{B}_s$), together with another B hadron ($B^\pm, B_s, \Lambda_b, \ldots$) of opposite b content, and the lepton charges will depend on the average on the fraction of mesons that may or may not mix. Since mixing occurs only in $B^0\bar{B}^0$ and ${B_s}^0\bar{B_s}^0$, what is measured is an "average" mixing parameter given by

$$\bar{\chi} = \left(\frac{BR^d{}_{s\ell}}{BR_{s\ell}}\right) p_d\chi_d + \left(\frac{BR^s{}_{s\ell}}{BR_{s\ell}}\right) p_s\chi_s \tag{2.4}$$

where p_d and p_s are the probabilities that respectively B_d^o or B_s^o be produced in the fragmentation of the quarks, $BR^d{}_{s\ell}, BR^s{}_{s\ell}$ are the individual semileptonic branching fractions and $BR_{s\ell}$ is the semileptonic branching ratio for the mixture. Results from several experiments on the measurement of $\bar{\chi}$ are summarized in table 2.2 and are in good agreement with one another. The products of p_d and p_s with the ratio of branching fractions, indicated with f_d and f_s, are taken

Experiment	$\bar{\chi}$	Reference
UA1	$0.148 \pm 0.029 \pm 0.017$	[25]
CDF	$0.176 \pm 0.031 \pm 0.032$	[17]
MAC	$0.21^{+0.29}_{-0.18}$	[20]
MARK II	$0.17^{+0.15}_{-0.08}$	[20]
Aleph	0.129 ± 0.022	[21]
L3	$0.121 \pm 0.017 \pm 0.006$	[22]
Opal	$0.143^{+0,22}_{-0.21} \pm 0.007$	[23]
Delphi	$0.121^{+0.044}_{-0.040} \pm 0.017$	[24]
World average	0.133 ± 0.011	[13]

Table 2.2: Measured values of $\bar{\chi}$. Only measurements at the Z^0 and $\bar{p}p$ are averaged

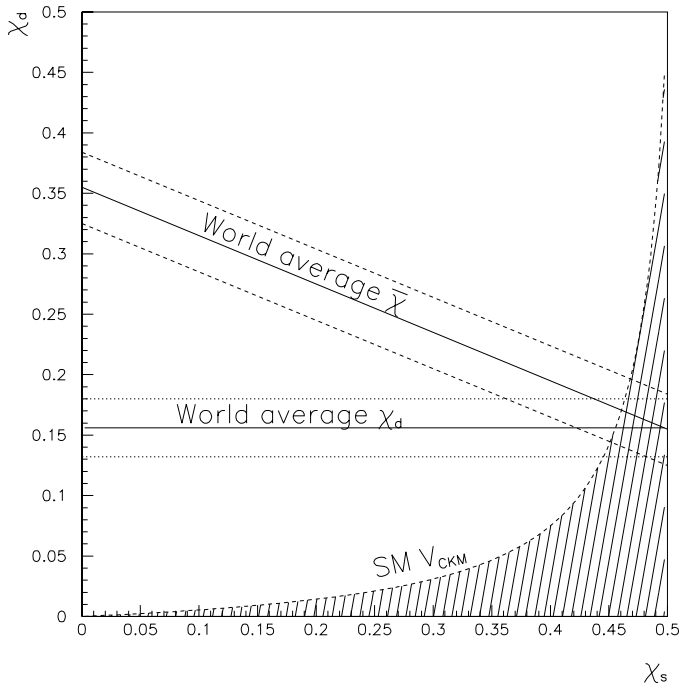

Figure 2.2: Constraints on the $\chi_d - \chi_s$ plane from ARGUS and CLEO measurements [19] of χ_d (band between dotted lines) and the world average of $\bar{\chi}$ (band between dashed lines) (see table 2.2). The hatched region is that allowed by the unitarity condition in the SM.

respectively to be 0.391 and 0.117, (from fragmentation studies [16]). Eq. (2.4) then defines a straight line in the $\chi_d - \chi_s$ plane (fig. 2.2). It is possible to extract a value for χ_s from the $\bar{\chi}$ and χ_d measurement: $\chi_s = 0.62 \pm 0.13$. On the other side the χ_d measurement and unitarity condition of the CKM matrix alone give $\chi_s > 0.44$.

Almost all the above measurements of $\bar{\chi}$ exploit lepton pairs as the decay products of a $B^0\bar{B}^0$ pair. The B mesons are tagged by their decay lepton charge, and the signature for mixing is given by an excess of like-sign dileptons.

Like-Sign as well as Opposite-Sign lepton pairs are produced by several processes other than the direct semileptonic decay of B meson pairs; processes which constitute the "physics" background to mixing. Lepton pairs can also result from a hadron faking a lepton in a single lepton event, or even from two hadrons, or from a cosmic ray impinging into the detector. Mixing must therefore be measured as an excess of LS lepton pairs over the predicted residual background passing all the cuts in the analysis.

Let's now examine the "physics" backgrounds to the double b semileptonic decay:

- Same B sequential decays. A single B hadron following the decay chain $B \to c\ell\nu$ and $c \to s\ell\nu$ always produces opposite-sign dileptons.

- Other B sequential decays. These are produced by $B^0\bar{B}^0$ pairs in which one B decays semileptonically, while the other decays hadronically, producing a charmed hadron which then decays semileptonically:

$$\begin{array}{cc} B \to c\ell^-\bar{\nu}_\ell & \bar{B} \to \bar{c} + X \\ \downarrow & \downarrow \\ c \to hadrons & c \to s\ell^-\bar{\nu}_\ell \end{array} \qquad (2.5)$$

  This is a source of same sign leptons unrelated to mixing.

- Prompt decays of hidden heavy flavour mesons. The leptonic decays of the J/ψ and Υ always produce $\ell^+\ell^-$ pairs. These can be removed by eliminating the appropriate invariant mass window.

- Semileptonic decay of $c\bar{c}$ pairs. This process always produces opposite-sign dileptons.

- Drell-Yan dilepton pairs. Always give an $\ell^+\ell^-$ and are distinguished by being "prompt", i.e. coming from the primary vertex, and by producing relatively isolated leptons with respect to b and c decays. Typically, anyway, the residual background from Drell-Yan dilepton production is non negligible and must be estimated from data and/or Monte Carlo.

Once all the selection cuts are made, it is still necessary to subtract the residual background in order to obtain a sensible result. Unlike in the $\Upsilon(4S)$ case, where the continuum outside the resonance peak may be used as an estimate of the only relevant background, it is often impossible to obtain such an estimate directly from the data. One has to rely on Monte Carlo predictions, which introduce large uncertainties on the final number due to their dependance on several unknown parameters.

In chapter 4 we will come again on this problem when discussing the CDF measurements of $\bar{\chi}$.

2.3 Direct measurements of $B_s^0\bar{B}_s^0$ mixing

As discussed above the only evidence on B_s mixing we have comes indirectly from the measurement of $\bar{\chi}$. It may be argued if a direct measurement of this phenomenon would be feasible at current experiments. The low sensitivity of the time integrated measurement, as discussed above, is mainly due to the poor knowledge about the production fractions p_d and p_s. It must be noticed, anyway, that the expression of χ_s in terms of x_s:

$$\chi_s = \frac{{x_s}^2}{2 + 2{x_s}^2} \tag{2.6}$$

quickly saturates to $\chi_s = 0.5$, and already gives $\chi_s = 0.45$ for the lower limit $x_s > 3$ from (1.35). This means that an estimate of x_s from the time integrated measurement of $\bar{\chi}$ is probably already impossible if $x_s > 4$. On the other side selectively tagging the B_s decay, although not helping to further constrain x_s, would make it possible to give a *direct* evidence for the mixing of the B_s.

Time dependent studies are, therefore, the only hope to obtain a measurement of x_s. These studies will need a very large statistics, due to the poor efficiency of the B_s tag and the large background contamination, and, with current resolutions will only explore up to $x_s \approx 15$. In fig. 2.3 the oscillating behaviour of the mixing ($B \to \bar{B}$) and non-mixing ($B \to B$) probabilities for the B_d and B_s are examined as a function of the proper time in units of the b lifetime. For x_d the world average is used, whereas the value $x_s = 5$ is used as an example; the fast oscillation rate will require a high spatial resolution on the position of the decay vertex to avoid "smearing" away the oscillations.

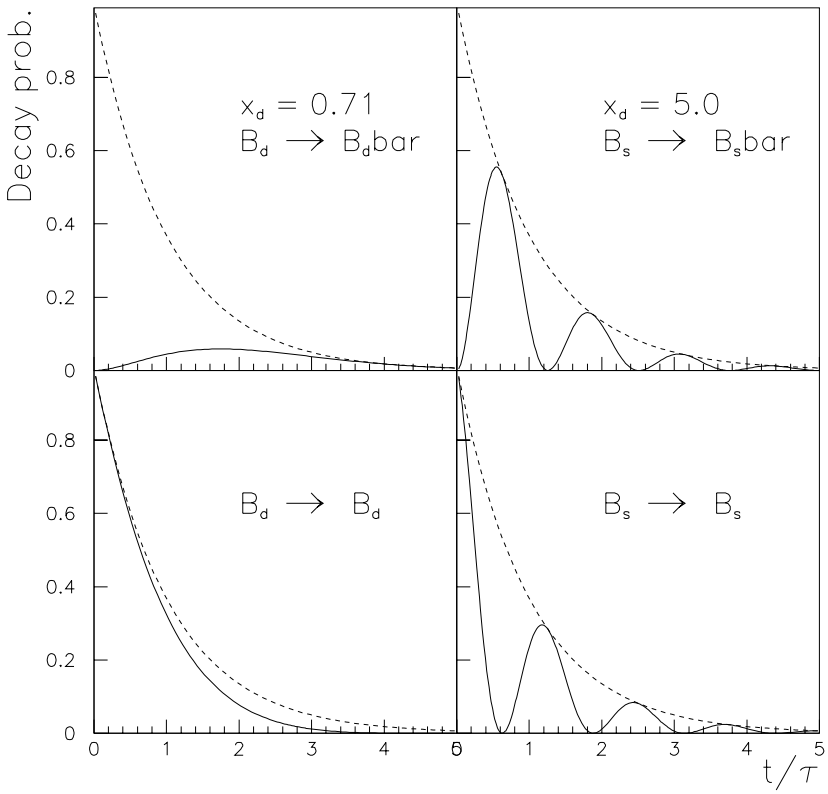

Figure 2.3: Time evolution for the B^0 and B_s systems. The top plots show the mixing probability for the B_d (left) and B_s (right) respectively using the value $x_s = 5$ which is a good lower bound for this quantity; the bottom plots show the non-mixing probabilities. An exponential decay (dashed) is superimposed "to guide the eye"

Chapter 3

The CDF Detector

3.1 Overview

The Collider Detector at Fermilab (CDF) is a large general purpose detector designed and built to study $\bar{p}p$ collisions at the Fermilab Tevatron collider at center of mass energy $\sqrt{s} = 1.8$ TeV, at present the highest in the world. The detector covers a large angular region, down to 1.7^o from the beam, and over the entire 2π range of the azimuthal angle[1].

The basic goals of the Collider Detector at Fermilab are:

- detect charged particles and measure their momentum;
- measure the position and energy of electromagnetic as well as hadronic showers;
- identify leptons;
- observe secondary vertices from decays of (relatively) long-lived particles and measure the decay length;
- observe indirectly non-interacting particles like neutrinos, by measuring the missing transverse momentum;
- perform flexible selections of events to be recorded on tape by means of functions of all the measured quantities listed above.

[1]CDF uses a conventional coordinate system with origin in the center of the detector, the z axis along the beam and $z > 0$ in the proton direction. The polar angle θ is measured with respect to the beam axis ($\theta = 0$ is the proton direction) while ϕ is the azimuthal angle ($\phi = 90^0$ is the vertical upward direction). Often the pseudorapidity $\eta = -ln(tan(\theta/2))$ is used in place of the angle θ.

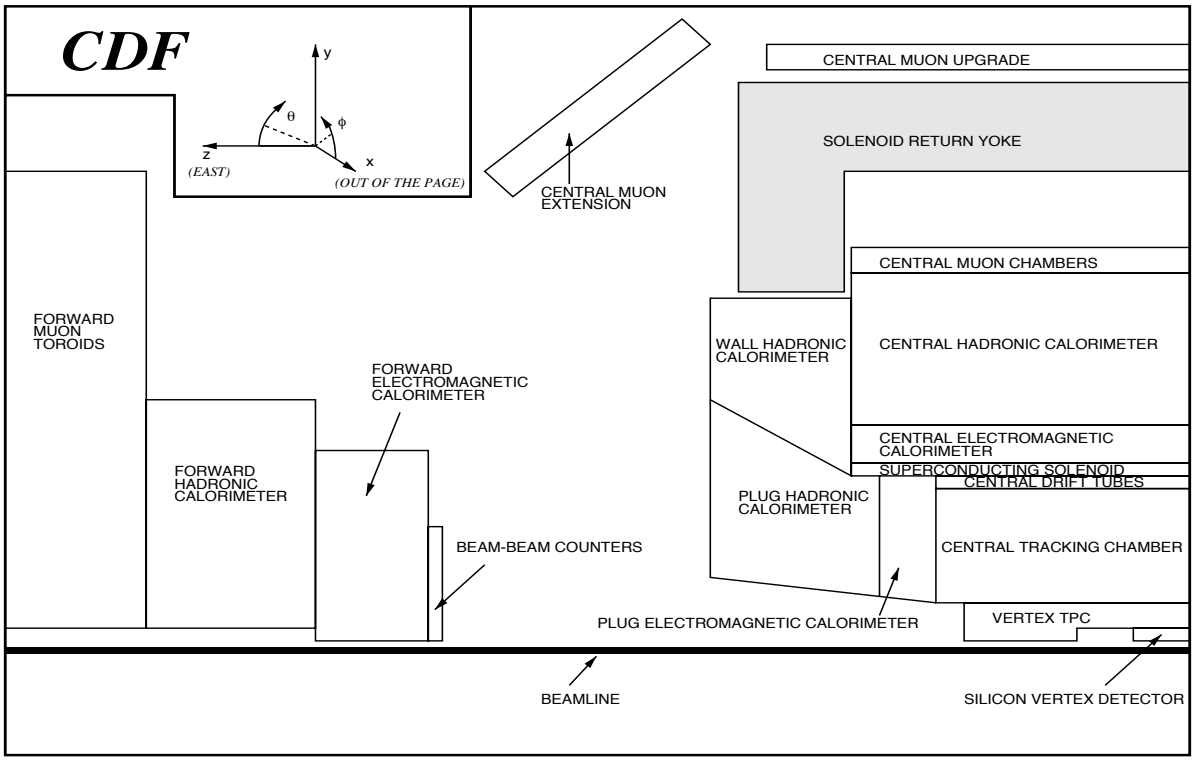

Figure 3.1: Side view of the forward half of the central CDF detector and of the entire forward detector

In order to achieve this, the interaction region is surrounded by layers of different detector components. Particles encounter in a sequence tracking detectors, sampling calorimeters and muon detectors. Events are analysed in a very short time (few microseconds) by a powerful and flexible trigger system.

The CDF detector (fig. 3.1) is divided into three main subdetectors: the central detector, also called *barrel*, a forward detector and a backward detector, the last two being totally symmetric with respect to the $z = 0$ plane.

A particle produced at the B0 collision point traverses first a Vertex detector (VTPC/VTX), followed by the core of the CDF tracking, the Central Tracking Chamber (CTC), a large cylindrical wire chamber. The whole tracking is immersed in the ≈ 1.5 Tesla magnetic field produced by a superconducting solenoid, which has the bending power necessary to allow the measurement of the large transverse momenta of particles produced in the interactions.

In the central region the barrel is completed by the Central ElectroMagnetic calorimeter (CEM) consisting of several alternating layers of lead and scintillator,

by the Central HAdron (CHA) calorimeter (iron with scintillators) and by the endWall HAdron calorimeter (WHA) at larger rapidities; the CEM includes at the shower maximum a layer of CEntral Strip chambers (CES) necessary to measure accurately the shower shape. At larger angles a Plug ElectroMagnetic (PEM) and Plug HAdron (PHA) calorimeter complete the coverage. The barrel is enclosed by the Central MUon chambers (CMU) which identify the highly penetrating muons which traverse the material of the rest of the detectors. The forward (backward) detector includes a Forward ElectroMagnetic (FEM) and Forward HAdron (FHA) calorimeter, completed by the magnetized steel toroids which, together with the Forward MUon chambers (FMU), help to detect muons produced at small angles with respect to the beam line. At $|z| = 582cm$, two sets of Beam-Beam Counters (BBC [31]) are found. These are scintillator hodoscopes close to the beam pipe used to provide the tracking chambers with an accurate measure of the interaction time ($\pm$200 ps) and of the vertex z position ($\pm$4 cm), to reject unwanted triggers and to measure the luminosity.

In the configuration described above, the CDF had a successful physics run in 1988-89. In the following years several upgrades have been made to the detector:

- a Silicon VerteX detector (SVX) built with single sided silicon microstrip detectors has been added, in order to precisely reconstruct displaced secondary vertices;

- the Vertex TPC has been replaced with a new Vertex detector (VTX), still consisting of time projection chambers, but capable to cope with the improved accelerator luminosity;

- a Central PreRadiator (CPR) detector, consisting of a set of drift chambers, has been placed around the coil of the superconducting solenoid: this detector is used in the photon/electron separation and identification;

- the muon system has been complemented with the Central Muon eXtension (CMX) which extends the angular coverage of the CMU to $|\eta| = 1.0$, and a Central Muon uPgrade (CMP) which adds an outer layer of proportional drift chambers behind an additional 60 cm of steel, with a coverage which is about 60 % of that of the CMU, thus improving the fake muon rejection in the central region.

In this configuration the CDF has taken data in 1992-93 collecting an integrated luminosity of about 21 pb^{-1}. For the work discussed in this thesis data from the 1992-93 run will be used, while in chapter 4 we discuss briefly an analysis made on 1988-89 data.

In the following we describe the CDF subdetectors mainly used in the analysis subject of this thesis, i.e. the tracking and the muon system. The trigger systems are also shortly described, with emphasis on the muon trigger. Details on other subdetectors and a full description of the whole CDF can be found in the literature [27].

3.2 The Central Tracking Chamber

The Central Tracking Chamber (CTC) [29] is a cylindrical wire chamber of inner radius 30 cm and outer radius 140 cm and 2 meters long. It consists of 84 layers of sense wires organized in five axial superlayers, providing $r-\phi$ information, and four stereo superlayers with alternate tilt angles of $+3^o$ and -3^o, which combine with the axial superlayers to provide $r-z$ information. Each superlayer consists of cells of sense wires tilted 45^o relative to the radial direction so that, once the effect of the solenoid field is taken into account, the actual drift direction is perpendicular to the radial direction. The outermost superlayer covers the region $40^0 \leq \theta \leq 140^0$ whereas the innermost one covers the region $14^0 \leq \theta \leq 166^0$. The resolution within a superlayer is $\approx 200\mu m$. The z resolution obtained combining axial and stereo wires is about 4 mm. The system can resolve double tracks within less than 5 mm. The momentum resolution for tracks passing through all the superlayers is

$$\frac{\delta p_t}{p_t} \leq 0.0011 p_t$$

in the region $20^o \leq \theta \leq 40^o$ and $140^o \leq \theta \leq 160^o$ this resolution is degraded.

The arrival time and pulse width of the shaped signal from the sense wires are measured by means of a TDC. In this last run the CTC electronics has been changed in order to make the discriminated pulse width proportional to the original pulse height to allow dE/dX measurement and particle identification.

3.3 Muon systems

The Central MUon system lies outside of the body of the central detector, at ~ 5 nuclear interaction lengths from the collision point. The Central MUon chambers cover the region $55^0 < \theta < 125^0$ and are segmented in ϕ into wedges 12.6 degrees wide, separated by *cracks* 2.6 degrees wide. The chambers are arranged in sets of three for each wedge, and have 4 layers each, in the radial direction, for a total of 16 cells (fig. 3.2).

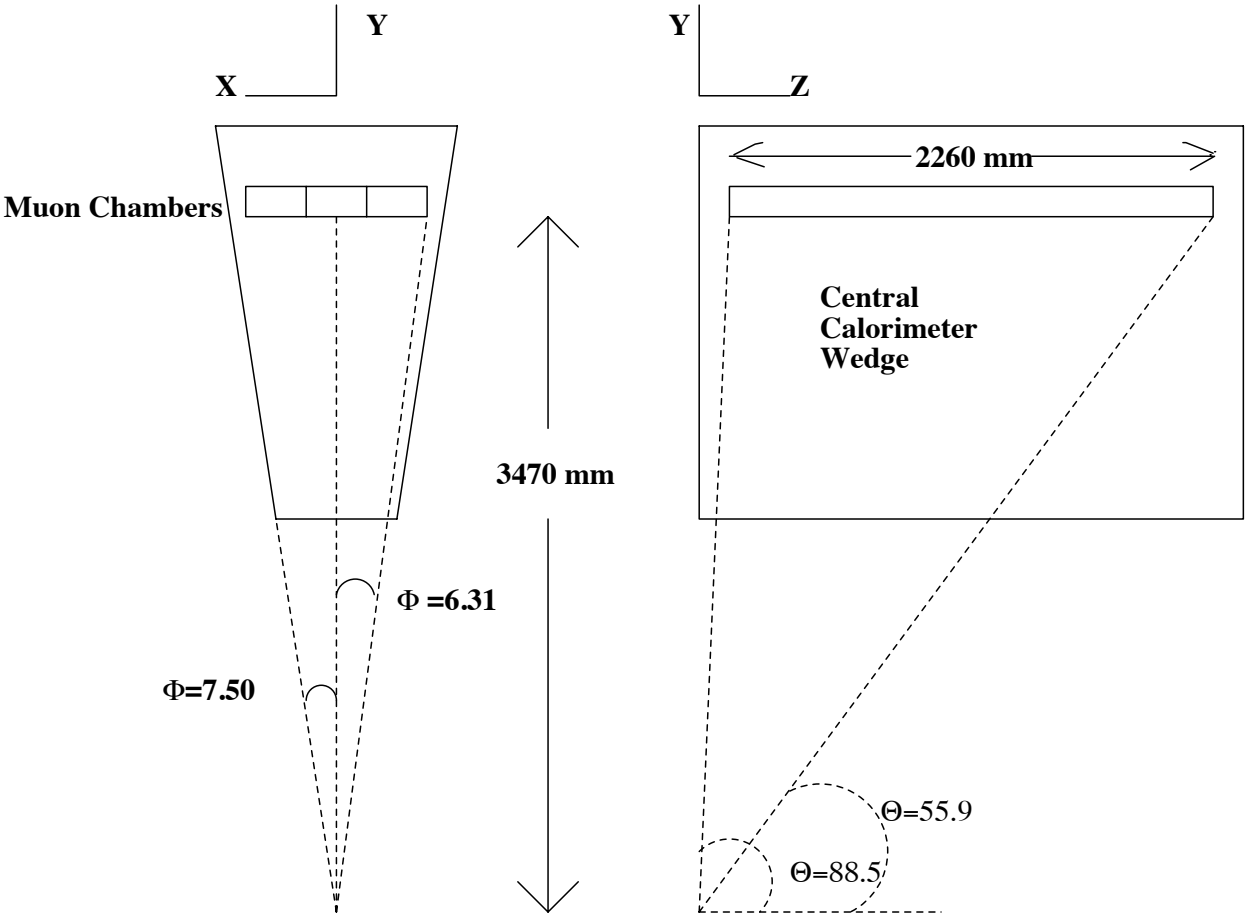

Figure 3.2: The CMU chambers are arranged in sets of three for each wedge in Φ, and each chamber run the whole length of one half of the calorimeter barrel.

Figure 3.3: Sectional view of a muon chamber.

The wires in each cell run the length of the wedge, about 230 cm, and wires from alternating cells in the same layers are connected together at $\theta = 90^o$. Fig. 3.3 illustrates a single chamber. The Central Muon uPgrade (CMP) consists of four layers of drift chambers which enclose the central portion of the CDF detector (fig. 3.1). An additional 60 cm of steel are interposed between the CMU and the CMP, steel provided in part by the return yoke of the CDF solenoid. This adds on the average 3.0 interaction lengths, thus improving the rejection of hadron punch-through.

The CMU covers approximately 84% of the solid angle $|\eta| < 0.6$; 63% is covered by the CMP and 53% by both. Fig. 3.4 shows the regions covered by the various systems.

The Central Muon eXtension (CMX), consists of sets of drift chambers arranged in free standing conical arches around each side of the central detector (fig.3.1) and sandwiched by scintillators to give timing information. They cover the angular region 42^o to 55^o and 125^o to 138^o in θ, extending the pseudorapidity coverage down to $|\eta| = 1$.

Due to multiple scattering in the calorimeter material, muons with p_t below a certain threshold (p_t^{min}) are not identified by muon chambers, because their trajectory is deflected so that they do not reach the chambers themselves. The minimum muon p_t to reach the CMP is $p_t^{min} = 1.8$ GeV/c, to be compared to $p_t^{min} = 1.5$ GeV/c in the CMU. In the CMX $p_t^{min} = 1.4$ GeV/c.

A charged particle traversing a chamber *hits* one wire in each layer; the pulse propagates on the (resistive) wire and is read out at each end of it. The integral charges at the two ends give the z position of the particle. The drift time gives the position of the track in the transverse plane (the direction transverse to the

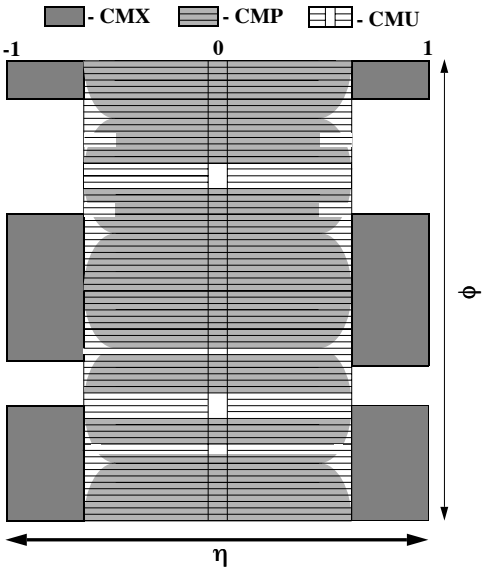

Figure 3.4: Angular regions covered by the various muon systems.

wire). The drift time is counted from the t_0 given by the beam crossing, corrected for the transit time of the particle and the length of the wires. An ADC/TDC module reads out the integrated pulses at each end. Tracks in the muon chambers (*stubs*) are assumed to be straight lines. A stub must have a minimum of two TDC *hits* associated with it to be considered good. The angle formed by (or the *slope* of) the track in the chamber with respect to the radial direction, is obtained by comparing the two drift times t_2 and t_4 (see fig. 3.3); it measures the total deflection suffered by the particle in the magnetic field of the solenoid, which is inversely proportional to the track momentum. Though momentum resolution is degraded by multiple scattering and is only $\delta p/p \simeq 60$ %, still this information is sufficient to be used in the trigger.

3.4 Trigger and data acquisition

The CDF data acquisition system (DAQ) consists of three main parts: the analog front end electronics, the FASTBUS-based digital control and readout system and the VAX-resident configuration and control system software [30]. The front-end electronics is designed to readout the $> 10^5$ channels of the CDF detector, digitize and transfer this information to the FASTBUS system and Event Builder. The main body of the FASTBUS system coordinates timing and data transfer from

front-end electronics and trigger systems to the VAX which logs the data on tape.

At a $\bar{p}p$ collider, physically interesting events are extremely rare compared to the number of bunch crossings. The task of a trigger system is to analyse the event structure and select this rare events. This is also absolutely necessary since while the bunch crossing rate is about 50 kHz, events can be recorded on tape only at a rate of a few Hz.

The CDF trigger [31] is structured in three levels which progressively reduce the rate, allowing the subsequent level to take decisions of growing sophistication, without this introducing a "deadtime" in the data acquisition. This decisions range from fast coincidence of scintillation counters, providing a *minimum bias* trigger in "level 1", to a full FORTRAN language elaboration on commercial Silicon Graphics multi-cpu unix processors in level 3, which is operated only at the end of the detector readout. At each level many concurrent decisions are taken in parallel, and each level is a logical OR of a number of triggers designed to select events with electrons, muons or jets.

Preamplifiers on detector channels provide two outputs: one, the "fast output", for immediate use by the trigger system, and the other for temporary front-end data storage until the trigger decision is made. The level 1 trigger uses fast output from the muons system and all the calorimeters. It shares a large part of its electronics with the level 2. The information available at level 1 contains BBC coincidence, muon candidates with p_t above a given threshold in the muon chambers, and the total transverse energy in EM and Hadron calorimetry for jet and electron triggers. The input rate of about 50 kHz at a typical instantaneous luminosity of 5×10^{30} cm^{2}s^{-1}, drops to about 1 kHz downstream of level 1.

The level 2 electronics decision is based on a list of energy clusters in the calorimeters from an hardware cluster finder, which is associated to fast $r - \phi$ tracking provided by the Central Fast Tracker (CFT) for electron - π^o discrimination; the CFT is a hardware track processor, using fast timing information from the CTC as input. The CFT resolution is $\delta P_T/P_T \sim 0.035 \times P_T$. The same CFT tracks are associated to muon chamber segments for muon identification. The rate out of level 2 is approximately 12 Hz.

The level 3 hardware is a "farm" of unix multi-cpu computer servers which run FORTRAN compiled programs, performing an high level offline-type analysis to reconstruct and select events with interesting physical "objects", make quality cuts on them, reject background events like bursts of noise, cosmic rays, etc. The consequent reduction of rate decreases the number of useless events written to tape. The rate downstream to the data logger is reduced to about 5 Hz.

Muon triggers

A muon is characterized by a highly penetrating charged track. To trigger on muons it is necessary to exploit information from tracking and the muon chambers.

At level 1 the information from the CTC is made available to the Central Fast Tracker (CFT) which identifies high p_t tracks. The CFT can complete a search for all the high momentum tracks in an average 2.5 μs/event, with a p_t resolution of 3.5 %, and an efficiency independent of the multiplicity.

Muon "brass" candidates ("stubs") above a certain p_t threshold (as measured by the chambers alone, see above) are defined as a series of hits in the four layers. At level 1 one or more muon "brass' candidates can be requested above a given p_t threshold as measured in the chambers (see §3.3). To reduce the rate of the level 1 single muon trigger, CMU stubs are ANDed with CMP.

At level 2 the CFT track parameters (p_t, ϕ) are correlated to the muon stubs by a dedicated level 2 trigger hardware, taking into account the ϕ spread introduced by multiple scattering, to extract the "golden" muon candidates. At level 2 one can then request one or more gold muons above a certain threshold, to form single (inclusive) muon triggers, or triggers on specific physics (e.g. J/ψ decays).

The information flow in the muon trigger is schematically shown in figure 3.5

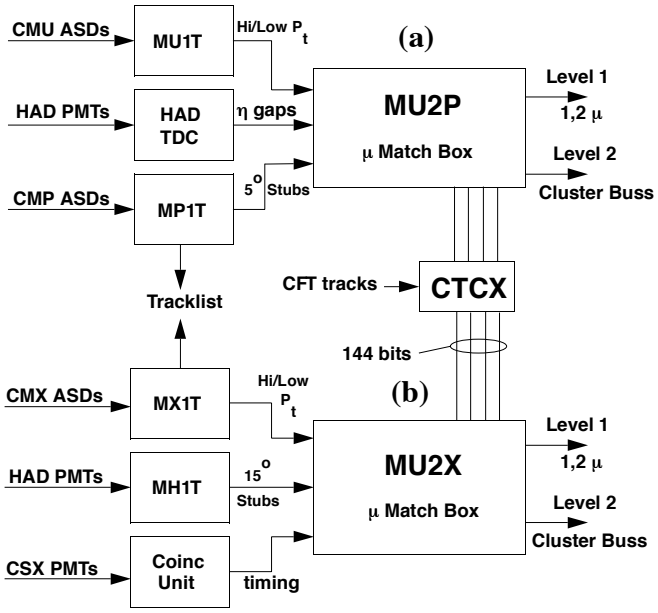

Figure 3.5: a) the original μ components with the upgrade (CMP) and the hadron TDC outputs used for filling the η gaps; b) the extension chambers (CMX) with the Hadron TDC outputs and CSX timing.

Chapter 4

Mixing at CDF

This chapter contains a comparative discussion of the previous measurements of $\bar{\chi}$ made at CDF from dilepton channels. This is done in order to gain some insight into problems common to these analyses. Implications on the measurement of $\bar{\chi}$ using dimuon data from 1992-93 run will then be discussed.

The time-integrated mixing parameter of B mesons has been measured at CDF in the 1988-89 run using electron-electron and electron-muon events from dilepton triggers[17]. In the absence of mixing the direct semileptonic decays of $B^0\bar{B}^0$ pairs (cfr.§ 2.2.2) will result in Opposite Sign (OS) lepton pairs, while the signature for mixing is the presence of Like Sign (LS) lepton pairs. An operative definition of the magnitude of mixing is given by the ratio of LS to OS dileptons:

$$R = \frac{N(\ell^+\ell^+) + N(\ell^-\ell^-)}{N(\ell^+\ell^-)} \tag{4.1}$$

For a sample of leptons from direct B meson pair decay, this would correspond to the R parameter of equation (2.2). In terms of $\bar{\chi}$ it would be expressed by:

$$R = \frac{2\bar{\chi}(1-\bar{\chi})}{(1-\bar{\chi})^2 + \bar{\chi}^2} \tag{4.2}$$

where $\bar{\chi}$ is expressed in terms of the specific B meson flavour as in (2.4), and measuring $\bar{\chi}$ would be a simple matter of counting. In real life we must face the fact that a dilepton sample is contaminated by certain kinds of background which must be accounted for:

- "physical" background: events in which real lepton pairs are originated in the processes listed in §2.2.2;
- conversions: events in which photons originated in the collision point convert into an electron pair in the detector material. π^o's Dalitz decays into $\gamma e^+e^-$are put in this class;

- decays in flight: hadrons (kaons, pions) decaying in flight into μ+ X;
- cosmic rays: high energy non-interacting cosmic rays traversing the interaction region in time with the bunch crossing window can fake a pair of opposite charge muons;
- "fakes": events where one or both leptons are in fact hadrons which fake the experimental signature of a real lepton.

From a naïve point of view one could think of making cuts in order to obtain a pure sample of direct B decay dileptons, then extract a value for $\bar{\chi}$ from the above expression for R. This would only work if there were cuts giving perfect rejection for background events, and high enough efficiency for signal events. On the other side even having an exact prediction of the fraction of each background process it would still be necessary to suppress part of it. In fact take the case were a background process with no sign correlation yields a very large number of events of both LS and OS: then R would equal 1. Whatever the sign correlation from mixing (or any other source) might be, it would be "submersed" by this background. In conclusion one can subtract the residual background, at the condition that it is a small enough fraction of the whole sample. The program is therefore: a) make cuts which compromise between background rejection and signal efficiency, b) estimate the residual background which must be accounted for in the final result. The last operation is done on real data whenever possible, otherwise resorting to Monte Carlo calculations.

In the list of §2.2.2 two entries are special: "other b" sequential decays and $c\bar{c}$ direct semileptonic decays. Both of these have topologies very similar to direct $B^0\bar{B}^0$ decays and cannot be statistically distinguished from them; a Monte Carlo must be used to estimate their fractional importance with respect to direct decays. Sequential decays are also special in the sense that they enter the expression of R with factors containing $\bar{\chi}$. Therefore the final expression for R is:

$$R = \frac{2\bar{\chi}(1-\bar{\chi}) + [(1-\bar{\chi})^2 + \bar{\chi}^2]N_s/N_f}{[(1-\bar{\chi})^2 + \bar{\chi}^2] + 2\bar{\chi}(1-\bar{\chi})N_s/N_f + N_c/N_f}. \tag{4.3}$$

where N_s/N_f is the ratio of sequential decays (N_s) to first generation decays (N_f) and N_c/N_f the fraction of direct $c\bar{c}$ semileptonic decays yielding lepton pairs, which always give OS lepton pairs. The ambiguity in obtaining $\bar{\chi}$ from this second degree equation is only fictitious, since the "non-mixed" decay is always defined as the most probable, therefore the mixing probability $\bar{\chi}$ is always the minimum between $\bar{\chi}$ and $(1-\bar{\chi})$.

4.1 The Dielectron Channel

Dielectron data came from a trigger requesting at least two candidate electrons with E_T (as measured in the EM calorimeter) ≥ 5 GeV. Candidate electrons are calorimeter clusters with a ratio of hadronic to electromagnetic energy (Hadronic Fraction, HF) less than 0.125. Events from the dielectron trigger are selected applying quality cuts to the single electron. These cuts use the energy release in the calorimeter and the matching of tracks with the strip chambers (CES) and the CEM shower position. Both electrons must be inside the central region ($|\eta| < 1.0$), and have HF< 0.05. The lateral shower shape must be consistent with an electromagnetic shower. The electron must also be within the fiducial volume (84% within $|\eta| < 1.0$) to avoid calorimeter cracks. The ratio of energy to track momentum must be less than 1.5 and the azimuthal and longitudinal shower shape, as from the CES, must be consistent with that of an electron. These requests are quite efficient for real electrons, and have a good rejection factor for fake ones.

Electrons produced by photon conversion and Dalitz decay are rejected by cutting on the distance of closest approach (d.c.a.) of the two tracks[1]. This cut is inefficient when one electron has very low p_t (tracks with $p_t < 0.4$ GeV/c are not reconstructed [32]).

J/ψ and Υ decays are removed by means of invariant mass cuts: $M_{ee} > 5.0$ GeV removes J/ψ's while $M_{ee} < 8$. .or. $M_{ee} > 10.8$ GeV removes Υ's. The lower limit on the invariant mass also rejects sequential decays of a single B meson into a lepton pair.

Electron pairs produced by the Drell-Yan mechanism are known to have little or no hadronic activity accompanying them; an isolation cut was used to reduce this background. The variable E_T^{iso}, defined as the difference between the total transverse energy deposited in a cone of radius $R = 0.7$ and that in a cone of radius $R = 0.4$ drawn around the electron direction in the $\eta - \phi$ space ($R = \sqrt{(\Delta\eta)^2 + (\Delta\phi)^2}$), was used; assuming E_T^{iso} independent of the electron p_t a fixed cut was applied on it and events with at least one electron which does not satisfy ${E_T}^{iso} > 2.4$ GeV were discarded as candidate Drell-Yan events.

The selection cuts are summarized in table 4.1.

The first three entries in table 4.1 represent sources of background which are completely eliminated by the corresponding cuts.

[1]First each electron was paired to every charged track in the event within a polar angle $\Delta\theta < 5^0$. If there was at least a track with a d.c.a. less then 0.5 cm and the point of closest approach was within the radius of conversion (50 cm), then the event was rejected

Bkg	Cut	Comment
Same B sequential decays	$M_{ee} > 5.0$ GeV/c^2	Also J/ψ removal
$J/\psi \to e^+e^-$	"	
$\Upsilon \to e^+e^-$	$M_{ee} < 8.$ .or. $M_{ee} > 10.8$ GeV/c^2	
$\gamma \to e^+e^-$, $\pi^0 \to e^+e^-$	d.c.a < 0.5 cm	explained in text
Drell-Yan	$E_T^{iso} > 2.4$ GeV	both electrons

Table 4.1:

Residual background from photon conversion and π^0 decays[2] was estimated by measuring the selection efficiency for conversions of the d.c.a. cut using a Monte Carlo simulation and correcting the number of events removed in the sample by this efficiency to obtain the total number of conversions before the cut. The difference of 19 ± 14 is expected to be equally distributed between LS and OS.

The number of Drell-Yan events surviving the cuts can be estimated fitting to the E_T^{iso} data distribution for OS events a combination of the distribution for a pure Drell-Yan sample and that for LS events, which are assumed to be Drell-Yan-free. A $Z^0 \to e^+e^-$ sample was used to obtain an approximation to the D.-Y. E_T^{iso} distribution. This procedure relies on the assumption that E_T^{iso} is independent of the electron p_t. From it 15.4 ± 4.5 residual Drell-Yan events are estimated in the sample.

Removing the matching and HF cut a sample of *pure fakes* was selected and a combination of the HF distribution of the pure fake sample and that of a pure electron sample from J/ψ decays fitted to the data distribution. The number of residual fakes expected to pass the selection was estimated to be 27.1 ± 9.2.

On the whole 38.4 events were subtracted from 134 OS events, representing about 28 % of all the OS, while 23 events were subtracted from the 78 LS events, i.e. 29 % of all the LS. After subtracting the estimated residual backgrounds in the expression of R

$$R = \frac{LS_{obs} - N_{fake}/2 - N_{conv}/2}{OS_{obs} - N_{fake}/2 - N_{conv}/2 - N_{DY}} \tag{4.4}$$

it resulted $R = 0.573 \pm 0.116(\text{stat.}) \pm 0.047(\text{sys.})$. The systematic error came from uncertainties on the subtracted background (table 4.2).

Although desirable, it is not always possible to extract residual background

[2]events where one of the electrons is produced via b or c decay, and the other is one leg of a conversion or Dalitz pair which was not identified either because it passed the cut, or having momentum below 0.4 GeV/c

Source	Absolute error	Error on $\bar{\chi}$
Conversions	72 %	9 %
Fakes	34 %	5 %
Drell-Yan	30 %	9 %
B semileptonic BR	15 %	8 %
MC Fragmentation	10 %	5 %
MC Statistics	22 %	11 %
$c\bar{c}$ fraction	100 %	4 %
Other MC events	62 %	5 %

Table 4.2: Contributions to the Systematic Error

fractions from data. In this instance simulations must be used, as in this case. The ISAJET Monte Carlo [33] was used, along with the detector simulation CDFSIM, to simulate a large sample of electron pair events from heavy flavour decays, in order to obtain the fractions N_s/N_f and N_c/N_f introduced in eq. (4.3). After the same selection as for real data the fraction of sequential decays was extracted from the 2.2 pb^{-1} of simulated events. The relative semileptonic branching fraction from PEP and PETRA experiments [34], which averaged to 0.115, was used; it was assigned a 15 % systematic uncertainty. Fragmentation of b quarks also contributed to the MC systematic error. The $c\bar{c}$ fraction resulting from simulation was small; although it was assigned a 100% uncertainty its contribution to the systematic error is 4%. Notice that the absolute cross section for $b\bar{b}$ production, which is not well known, cancels out everywhere.

To extract the value of the mixing parameter the ratio R as defined in eq. (4.4) is substituted into (4.3). The contribution from each source is listed in table 4.2. The final result for $\bar{\chi}$ is:

$$\bar{\chi} = 0.172 \pm 0.060(\text{stat}) \pm 0.024(\text{sys}) \pm 0.026(\text{MC})$$

4.2 The Electron-Muon Channel

The data for this analysis came from a dilepton trigger, i.e. a trigger requiring one candidate electron with $E_t > 5$ GeV/c and one candidate muon with $p_t > 3$ GeV. The electron-muon channel is free from Drell-Yan, conversions, Dalitz pairs and meson $(J/\psi, \Upsilon)$ decay background.

Quality cuts on the electron are the same described in the previous section.

The following quality cuts were applied to the muon candidates:

1. energy in the calorimeter tower corresponding to the muon track consistent with a minimum ionizing particle (mip);
2. track - stub matching within 20 cm;
3. combined track - stub $\chi^2 \leq 10.0$;
4. track quality cuts: number of CTC hits ≥ 50, $z_{trk} - z_v \leq 5.0$ cm.

Again an invariant mass cut was applied on the electron-muon pair, $M_{e\mu} > 5.0$ GeV, to get rid of sequential decays.

Even after selection cuts the sample will contain fake as well as real leptons. This residual background from fake leptons was determined using an inclusive electron sample, of which e-μ events are expected to be a subset. The sum of real-e fake-μ and fake-e fake-μ events expected in this sample is the product of the number of tracks satisfying the muon selections (m-tracks) by the fake-μ-per track rate F_μ. The number of fake-e real-μ events is the product of the number of m-tracks by the real-μ-per-track rate R_μ. The probability of an m-track being identified as a muon, f_μ, was determined experimentally using a *minimum bias* sample resulting in $f_\mu = 0.27$ %. For this sample a probability of real muon production from heavy-quark similar to the inclusive low-E_T electrons was assumed, implying that the presence of a fake electron does not change the probability of finding a real muon. Since by definition $f_\mu = F_\mu + R_\mu$, the product of f_μ by the number of m-tracks contains an extra term with respect to the number of events containing a fake lepton; this arises from R_μ times the number of tracks in *real* electron events. A comparison of the quality of muons in the minimum bias sample to a J/ψ sample showed that a large fraction of the muon candidates in the minimum bias sample is background. Therefore this extra term is small compared to the other terms.

Since an inclusive electron sample with the same E_T threshold as the e-μ sample was not available, samples collected with trigger thresholds $E_T > 7$ GeV and $E_T > 12$ GeV were used. The product of the number of m-tracks in the inclusive electron sample multiplied by f_μ gave a background fraction of 19 ± 9 %, independent of the E_T threshold.

Using a minimum bias sample to determine f_μ relies on the assumption that m-track properties in minimum bias events be similar to those in events with electron candidates. In fact the difference in K/π ratio, and p_t spectrum could change f_μ substantially. Varying the K/π ratio from 0.12 to 0.32 [35], induced

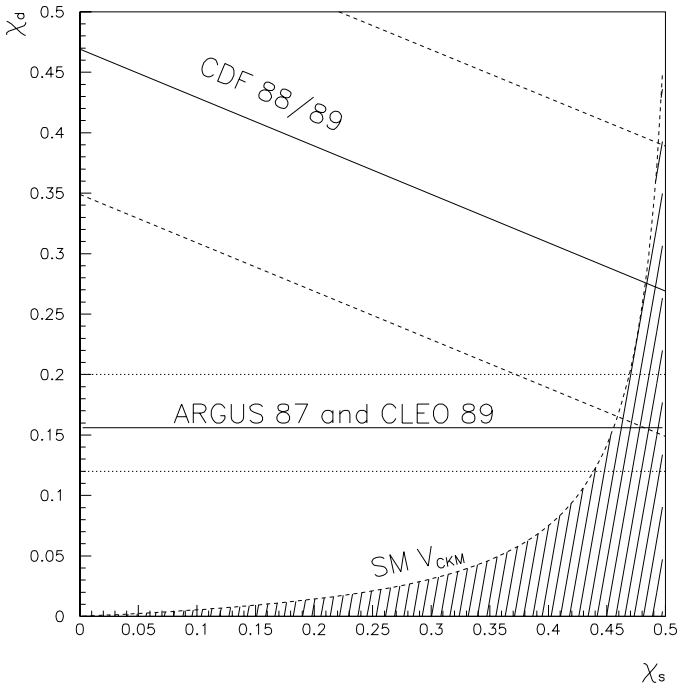

Figure 4.1: The mixing probability of B_d^o vs. that of B_s^o from 88/89 CDF published result, assuming B_u, B_d and B_s are produced in the ratio 0.375:0.375:015 [17]. The band between dotted lines is the ARGUS and CLEO measurement of χ_d which was current at the time of publication. Bands represent $\pm 1\sigma$ uncertainty. The hatched region is that allowed by the SM unitarity condition.

a 15 % variation on f_μ. Varying the track p_t between 3 and 12 Gev a 20 % variation. This effects were included in the systematic error. No sign correlation is expected within the fake muons from the inclusive electron sample, therefore a symmetric subtraction is made, resulting in:

$$R(e\mu) = 0.556 \pm 0.048(\text{stat})^{+0.035}_{-0.042}(\text{sys}).$$

Sequential and charm fractions were estimated using ISAJET as above. The systematic from the Monte Carlo is common to the two channels. The result for the e-μ channel is:

$$\bar{\chi} = 0.179 \pm 0.027(\text{stat}) \pm 0.022(\text{sys}) \pm 0.032(\text{MC}).$$

The average of the measurement in the two channels can be used to extract a constraint on the values of χ_d and χ_s as in fig. 2.2. Constraints obtained using only the CDF results are shown in fig. 4.1.

4.3 The dimuon channel

The attempt to measure $B^0\bar{B}^0$ mixing in the dimuon channel is justified by the interest of completing the set of possible independent channels. We discuss the possibility to apply to the dimuon case some of the techniques employed in the other channels, leaving to the following chapter a detailed discussion of the analysis procedure.

First of all the sources of dimuons with various charge correlations in $\bar{p}p$ collisions are listed for further reference:

1. $B\bar{B} \to \mu\mu + X$ both direct or both sequential, will contribute to LS and OS with the charge correlation from mixing;

2. $B\bar{B} \to c + \mu$, $c \to \mu + x$ will contribute to LS and OS with inverse charge correlation from mixing;

3. $\bar{B}B \to \bar{c} + \mu$, $\bar{c} \to \mu + x$, the C conjugate process of the one above, will contribute to LS and OS as well with inverse correlation;

4. $c\bar{c} \to \mu\mu$ will contribute to OS only;

5. Drell-Yan dimuon production will contribute to OS only

6. $\Upsilon \to \mu\mu$ will contribute to OS only

7. Same-Side sequentials, $B \to c + \mu$, $c \to \mu + x$ will contribute to OS only (this will actually be completely eliminated by a lower cut on the invariant mass);

8. Residual cosmic rays will contribute to OS pairs.

9. hadron decay in flight and punchthrough are expected to give equal amounts of LS and OS dimuons.

Let's now examine each step of the procedure from raw data to the final number, and the methods to deal with the various backgrounds:

1. cuts.

   The muon selection principles are basically unchanged: they are based on the combination of tracking and muon chambers as already discussed for the e-μ channel. A new handle to improve the rejection of fake muons in the central region is offered by the CMP (see chapter 3).

   Several backgrounds in the dimuon channel are common to the dielectron channel: resonance decays, same-side sequential decays and Drell-Yan pairs. For what concerns J/ψ, Υ and same-side sequential decays, invariant mass cuts are effective, and can be applied in this case as well. Drell-Yan muon pairs will be handled by looking at the lepton isolation, similarly to what was done for the dielectron channel.

2. estimate of residual background.

   To evaluate the residual background two methods have been applied in the analysis just described. The first relies on quantities which are differently distributed for signal and background, and the availability of pure-background and background-free samples. It is exemplified by the Drell-Yan evaluation in the dielectron measurement. We will use this technique for the Drell-Yan subtraction, although other quantities can be studied besides E_T^{iso} and samples with p_t spectra more similar to Drell-Yan should probably be used (one such sample is $\Upsilon \to \mu^+\mu^-$).

   The second technique was used for the fake muon subtraction (including decays in flight). This consists, as described in §4.2, in determining f_μ, the probability of a track being identified as a muon, and using it to determine the fake dimuon fraction in a single muon inclusive sample. To do this a large sample of single muon events from an independent trigger is needed, in which the muon satisfies the same selection criteria applied in the dimuon case.

   For the present di-muon channel, such a large sample from an independent trigger is not available, since the p_t threshold of the single muon trigger was much higher then for the di-muons. Therefore we will resort to a new technique, described in the next chapter, that exploit the presence of the new CMP detector to achieve a statistical subtraction of the fake muons background.

3. sequential and charm fractions evaluation using Monte Carlo.

   As for the previous measurement, the ISAJET Monte Carlo and CDF detector simulation will be used to generate a sample of muon pairs from

heavy flavour decays. Systematic errors due to the Monte Carlo statistics and branching ratios (bottom of table 4.2) are expected to be reduced since: a) it is much easier to produce a large Monte Carlo sample and b) the use of recent measurements of the B semileptonic branching fractions from the CLEO experiment, with errors smaller by a factor 5, will reduce the systematics from this source (The current PDG average is $\Gamma(\mu^{\pm}\nu_{\mu}hadrons)/\Gamma_{tot} = 0.103 \pm 0.005$ with ~ 5 % error, to be compared to those from older experiments, which had an error of order $10 \div 20$ % [34]). Fragmentation effects, structure function choice and detector response must be investigated, but are not expected to improve.

4. obtaining $\bar{\chi}$ from the LS to OS ratio.

   Statistical errors and systematic errors from steps 2 and 3 contribute in similar amounts to the final error of the "old" measurements. Although 1992-93 dimuon data has higher statistics due to the very low thresholds ($p_t > 3$ GeV/c) and can profit of about six times more integrated luminosity than previous measurements, we will see the statistical error on $\bar{\chi}$ using dimuon data is not substantially better, with respect to the combined error from the ee and $e\mu$ samples of 1988-89. The reason for this is the statistical subtraction of the large background from fake muons which will be discussed in the next chapter. With respect to the $e\mu$ sample the dimuon sample is much less clean, partially canceling the advantages of the larger statistics.

Chapter 5

Real muon pairs in CDF dimuon data

In this chapter a procedure is described to measure the number of real muon pairs in the CDF dimuon sample. As CDF dimuon sample we take the inclusive CMU-CMU sample, i.e. all the events in which two muons (at least) have been reconstructed in the CMU chambers. Therefore our goal is to measure the number or real muon pairs which give stubs in the CMU, irrespective of the CMP. In order to distinguish muon candidates that have a stub in the CMU only, from muon candidates that give a signal in the CMP as well, we introduce the following definitions, that will be used throughout this chapter:

CMU muon A muon object in CMU is defined as a track pointing to a CMU stub, including all cuts on track and stub quality and their matching, as defined later on. A CMU muon may have a matching CMP stub, but this condition is not required.

CMP muon A CMU muon (including cuts) with a matching CMP stub is called a CMP muon.

We choose to use the CMU muons, even though it is clear that this sample contains a larger amount of fake muons, compared to a sample of CMP muon pairs, so that we can exploit the CMP signal to evaluate the number of fake pairs in the CMU sample. The strategy to measure the number of real muons (M) in the CMU detector exploits the different probability for real muons and fake muons (F) detected in the CMU, to be observed also in the CMP detector. In fact, since the two detectors are separated by a large amount of material, real muons have a much higher probability than hadrons to reach the CMP once detected in the CMU.

Since the measurement is based on the different *relative efficiencies* of real and fake CMU muons to be detected in the CMP, only CMU muon candidates which are able to reach the CMP (i.e. with $P_t > 3$ GeV/c) and with an extrapolated track pointing to the CMP *fiducial* volume (i.e. within 5 cm of the chambers' active volume borders) will be considered.

Let N_U be the total number of these CMU muon candidates, M and F the (unknown) numbers of true and fake muons observed in the CMU, ϵ_μ and ϵ_f respectively, their relative probability to be observed also in the CMP. The following relation holds:

$$N_U = M + F \tag{5.1}$$

$$N_P = \epsilon_\mu M + \epsilon_f F \tag{5.2}$$

where N_P is the total number of muon candidates observed in the CMP. Even in this simple case, we are not able to isolate the sample of real muons, but from the two measured numbers N_U and N_P and the two measured efficiencies ϵ_μ, ϵ_f, the number of real muons in the CMU, M can easily be extracted:

$$M = \frac{N_P - \epsilon_f N_U}{\epsilon_\mu - \epsilon_f} = \frac{\epsilon - \epsilon_f}{\epsilon_\mu - \epsilon_f} N_U \tag{5.3}$$

where $\epsilon = N_P/N_U$.

These simple equations that determine the number of single real muons, can be extended to the case of muon pairs, i.e. to the case when events with at least two muon candidates are considered, and one wants to determine how many candidate pairs are formed by two real muons. This chapter is devoted to the measurement of the number of true CMU muon *pairs*, which we will also indicate with M. The formal derivation of M from the measured quantities is only slightly more complicated because we are dealing with muon pairs. It will proceed through the measurement of the quantities corresponding to N_P, and N_U, and the extraction from data of the values of ϵ_μ, ϵ_f.

In § 5.1 the data samples used in the analysis are discussed, from the trigger definition to the offline selection. First of all the dimuon sample used to evaluate R is described. Since, as will be seen in detail in § 5.2, one of the main problems is that the uncertainty on ϵ_f affects the determination of M proportionally to F (see eq. 5.2), it is important that the number of fake CMU muons F be kept as small as possible, to reduce the uncertainty on M (eq. 5.3). In this section a set of cuts is studied to provide a CMU sample as pure as possible ($M \simeq F$ or larger). Other samples are introduced, even though they are only used later in the analysis:

a) a J/$\psi \to \mu^+\mu^-$ sample used to measure the real muon CMP relative efficiency ϵ_μ;

b) a $K_s^0 \to \pi^+\pi^-$ sample used to obtain a lower limit on the fake muon CMP relative efficiency ϵ_f;

In § 5.2 the technique to obtain the number of real muons is discussed in deep. The final, more complicated set of equations to be solved to evaluate the number or real muon pairs is then introduced.

In § 5.3 the numbers corresponding to N_U, N_P in the case of muon pairs are measured using the selection cuts described in 5.1.

In § 5.4 ϵ_μ is measured from the J/ψ sample and inserted, along with numbers from the preceding section, into the formal solutions of the dimuon equations, thus obtaining the numbers of real muon pairs (M's) as functions of the fake CMP relative efficiency ϵ_f. The observed dependence of the solutions on ϵ_f then suggests an approximate way to evaluate M using only a lower limit on ϵ_f, obtained from a sample of pions from the decay $K_s^0 \to \pi^+\pi^-$. The extraction and checking of this lower limit are discussed in § 5.5.

Finally, in § 5.6 all the measured quantities are put together to extract the numbers of true CMU muon pairs with their errors.

5.1 Data samples and selection cuts

The main data sample used for this analysis was collected during the 1992-93 Tevatron collider run by CDF. It is an inclusive dimuon "high mass" sample, since it contains events with at least two candidate muons above an invariant mass threshold of 4.6 GeV/c^2.

Events were selected which passed dimuon triggers. General features of the muon trigger have been discussed in chapter 3:

- At level 1, two CMU or one CMU and one CMX stubs are required with more than 2 TDC hits. The CMP is not included in the trigger since the CMU rate is already acceptable.

- In the level 2 dimuon trigger, two muon candidates are required, one of which must be a *gold* muon matching a track with $p_t > 3.0$ GeV/c in the CFT. CMX-CMX pairs were not included at level 2 since the trigger rate is too high.

- The first level 3 requirement is the confirmation of the level 2 decision, therefore at least two muon candidates (muon "objects") must exist in the

event. A FORTRAN filtering procedure is then run which associates a track with the second muon stub and imposes a χ^2 cut for the matching of each track with the associated stub. Events from the dimuon triggers may in general have triggered other selections as well.

During offline processing, a general "production" code is run on the event, performing a systematic search for interesting physics objects, such as muon candidates, even if they were not identified by the triggers. The small fraction of events passing triggers other than the dimuon ones but satisfying the same level 3 requirements ("volunteers") were included in the sample at production time in order to allow trigger efficiency studies on an unbiased sample.

The muon candidates are selected by applying quality cuts [36]. Data is then "splitted" into different sets depending on the triggers satisfied and/or on the physical objects they contain. Out of these different sets, the one we used for the mixing analysis is one called "High mass dimuon" sample. The "High mass dimuon" dataset thus selected consists of $17.43 \pm 0.63\ pb^{-1}$ of integrated luminosity, corresponding to 505,196 events.

The sample of the "High mass dimuon" is defined by the requirement of at least two muon objects with an invariant mass between 4.6 and 150 GeV/c^2, with a P_t above 1.4 GeV/c. The originating vertex of the two muons must be within 30 cm of the nominal center of the detector in the z coordinate ($|Z_{vx}| < 30$ cm). On an run by run basis it was also checked that the muon systems involved in the analysis (CMU and CMP) and the CTC were fully operational, and events from runs that were declared bad because of malfunctions in these detectors were discarded (BADRUN flag [38]).

A basic quality requirement for a muon is that the corresponding CTC track is of good quality: at least two axial and two stereo CTC superlayers were required to have fired in order to accept the muon ($N_a \geq 2$, $N_s \geq 2$). The track was also required to give a good three-dimensional fit. Loose cuts are then applied on the CTC-stub matching, in order to avoid improper or double links between the track and the stub. Since the analysis is based on the relative efficiency of a CMU candidate muon to be detected in the CMP only muons with $P_t > 3.0$ GeV/c and with extrapolated track pointing within 5 cm of the borders of the CMP fiducial volume are considered. A real muon that satisfies these requirements has $> 99\%$ probability of giving a stub in the CMP.

5.1.1 Muon quality cuts

We have mentioned in the introduction that it is necessary to have such a set of selection cuts as to keep F as small as possible. In section 5.2 we will see in

detail how keeping F small results in less sensitivity of M on the error on ϵ_f.

In the following the cuts chosen to enhance the muon candidate quality are discussed, their efficiency for real muons and their rejection power for "fake" muons (both PunchThrough [PT] and Decay-In-Flight [DIF]) are analysed using a Monte Carlo. It is now appropriate to give a precise definition of these two categories of fake muons:

DIF we include in this category all cases in which an hadron (π or K meson) decays into a $\mu\nu$ pair before reaching the calorimeter iron.

PT this category contains all cases in which the hadron gives a stub in the muon chambers without decaying. It therefore includes both the case where the hadron simply does not interact in the absorbing material (non-interacting punch through) and the case where the hadron produces a shower in the calorimeter and a charged track from the shower leaks into the muon chambers.

A single particle Monte Carlo was used to find the optimal cuts in order to preserve prompt and non-prompt muons and reject as many as possible fake muons from PT and DIF. Motivation, efficiency on real muons and rejection power for fakes are studied for each cut using the simulation.

A control sample of "true" prompt muons was generated to check the efficiency of the cuts. Five other samples were generated: a sample of π and a sample of K DIF, a sample of pion, a sample of K^- and a sample of K^+ PT. The particles were generated with a P_t spectrum parameterized on the P_t spectrum of charged particles measured at CDF [37].

First the stub quality is studied, irrespective of the matching track.

In figure 5.1 the distributions of the number of TDC and ADC hits in the CMU chambers associated to the muon candidate by the pattern recognition are shown. The cuts are indicated by arrows. Requiring at least three hits both in the TDC and ADC rejects some PT (whose reconstructed stub may not include hits on all of the four wires because of energy loss by interaction with the material, or bad pattern recognition due to nearby jet activity) while being very efficient for real muons. Notice that at least two TDC hits are implicitly required to define the stub's transverse momentum.

The variable N_{CLUS} is defined for a CMU stub as the number of TDC hits clustered around the stub, including the hits forming the stub itself. For a perfect muon the ideal value of N_{CLUS} is 4, while an hadron interacting in the calorimeter and punching through it will generate a splash of hits (fig. 5.2). A real muon emitting a delta ray or crossing two neighboring cells can give $N_{CLUS} = 5$, so as

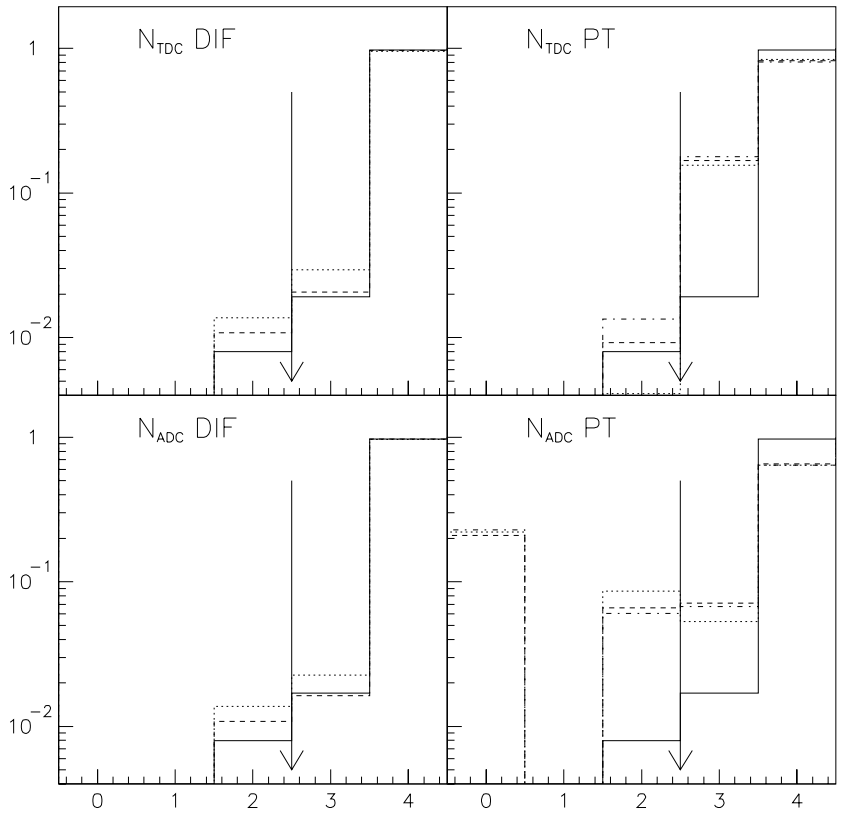

Figure 5.1: N_{TDC} (top) and N_{ADC} (bottom) respectively for pion (dashes) and kaon (dots) DIF (left), and pion (dashes), K^- (dots), and K^+ (dot-dash) PT (right) from a single particle Monte Carlo, compared to muon simulation (solid).

muons from b decays inside a broad jet. Therefore accepting $N_{CLUS} < 6$ gives a moderate rejection to punchthrough, while being highly efficient on the signal [39].

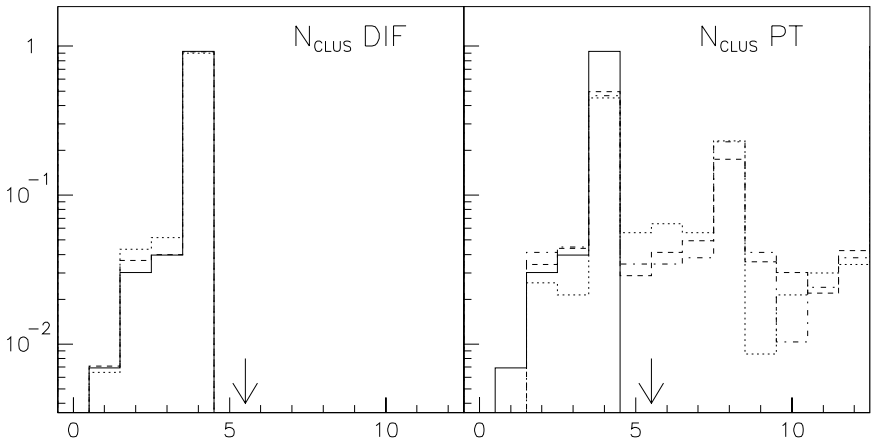

Figure 5.2: N_{CLUS} respectively for pion (dashes) and kaon (dots) DIF (left), and pion (dashes), K^- (dots), and K^+ (dot-dash) PT (right) compared to muon simulation (solid).

A cut on the impact parameter of the matching CTC track is useful to reject cosmic rays faking a muon pair and has some effect on DIF muons where a kink can cause the track to be split in two by the reconstruction algorithm or to be distorted, in both cases simulating a large impact parameter. On the other side muons from B meson decays are expected to have an average impact parameters of a few hundred microns, and therefore one must use caution in cutting on this quantity to avoid the risk of biasing the final mixing result. For these reasons we choose a very conservative cut at $|d| < .3$ cm (see fig. 5.3), which still has a good rejection power on cosmics (see section 6.1) and some on DIF, while preserving essentially all the B decays.

The matching between the CTC track and the CMU stub is of paramount importance as a quality cut. It allows to reject both DIF and PT: for DIF tracks the matching is worsened by the decay kink, even for decays outside the CTC, for which the track has been reconstructed properly; for PT tracks the effect of interaction in the material will widen the matching distance distributions. This is shown in fig. 5.4 for the two variables $n(\sigma_x)$ and $n(\sigma_z)$ defined as the distance between the extrapolated CTC track and the stub position in the CMU respectively in the transverse plane and in the z direction, divided by the sigma of the multiple scattering angle distribution for a muon of that P_t. In the z direction a fixed cut is made at 3σ, unless in cases where this corresponds to

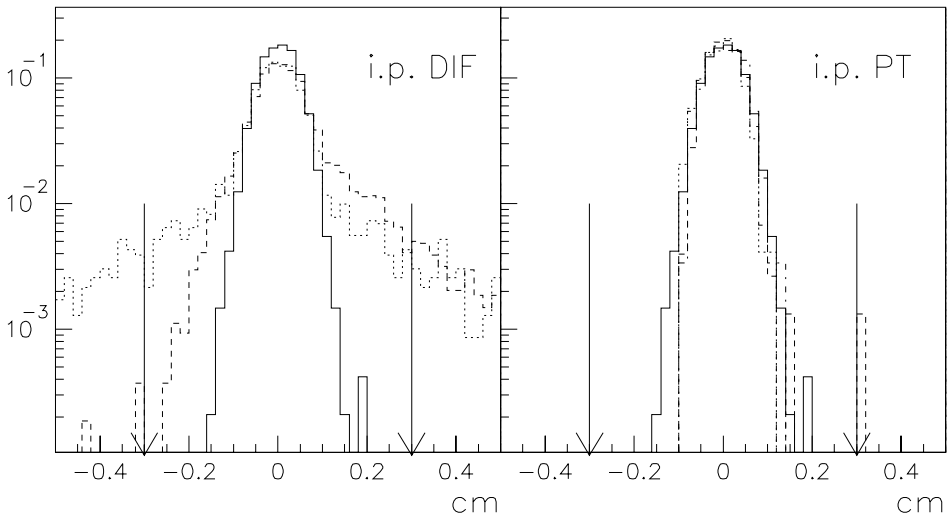

Figure 5.3: Impact parameter distributions for left: DIF pions (dashes) and kaons (dots) compared to prompt μ (solid); right: PT pions (dashes) and K (dots) compared to prompt μ (solid).

less than 8 cm; this is to preserve the efficiency when non gaussian tails in the multiple scattering may be important. In the transverse plane the combined χ^2 for the matching of the extrapolated track and the CMU stub position and slope is exploited for low muon momenta (fig. 5.5). Since the slope measurement has non-gaussian tails at high momenta, the χ^2 cut is released for $P_t > 20$ GeV/c, and a transverse distance cut at 3σ of multiple scattering (or 2 cm, whichever is larger) is applied instead (see fig. 5.4).

From the discussion above we can classify the applied cuts in three sets: "stub quality" cuts, the impact parameter cut, and muon "matching cuts". For these three sets the effect on the various simulated samples is summarized in table 5.1 for DIF and 5.2 for PT. The values in each row of these tables are the fraction of events remaining after the cut in that row and all those in preceding rows. From the first table it is clear that the impact parameter cut is mostly effective on DIF, especially on kaon; the matching cuts reject a fraction of the kaon DIF. On the other side the matching cuts and the stub quality cuts are mostly efficient on PT as can be inferred from table 5.2.

Selection cuts are summarized in table 5.3.

5.1.2 The J/ψ sample

Another sample derived from the same dimuon trigger described in section 5.1 will be used in this analysis. The J/ψ sample is obtained by imposing the same

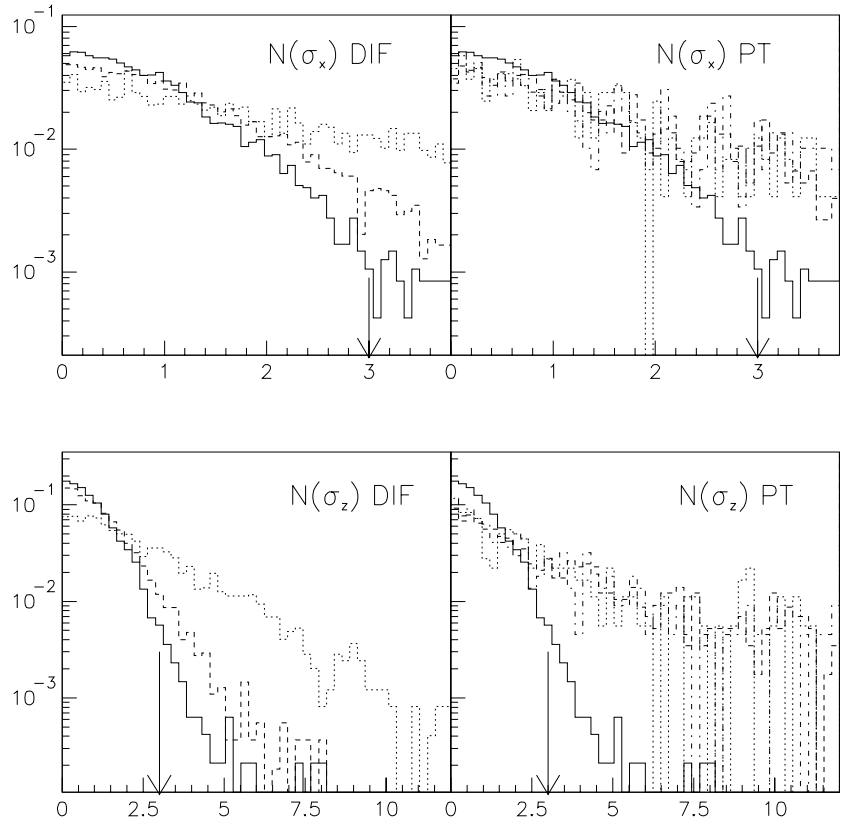

Figure 5.4: The distances of extrapolated CTC track to the CMU stub measured in sigmas of the multiple scattering distribution in the transverse plane ($N(\sigma_x)$, top) and the z direction ($N(\sigma_z)$, bottom). Again on the left are distributions for pion (dashed) and kaon (dotted) DIF compared to prompt muons (solid), and on the right distributions for pion (dashed), K^- (dotted), and K^+ (dot-dashed) PT. For the z coordinate arrows indicate the cut (unless $\delta z < 8$ cm). For the x coordinate arrows indicate 3σ but the cut is only applied to muons with $P_t > 20$ GeV/c.

	$\pi^{\pm}$		$K^{\pm}$		$\mu^{\pm}$	
cut	CMU	CMP	CMU	CMP	CMU	CMP
stub quality	0.99	0.99	0.99	0.99	0.99	0.99
impact parameter	0.94	0.93	0.87	0.84	0.99	0.99
matching cuts	0.88	0.93	0.54	0.65	0.97	0.98

Table 5.1: Cumulative efficiency of the three groups of cuts studied for Monte Carlo DIF samples and for the prompt muon sample.

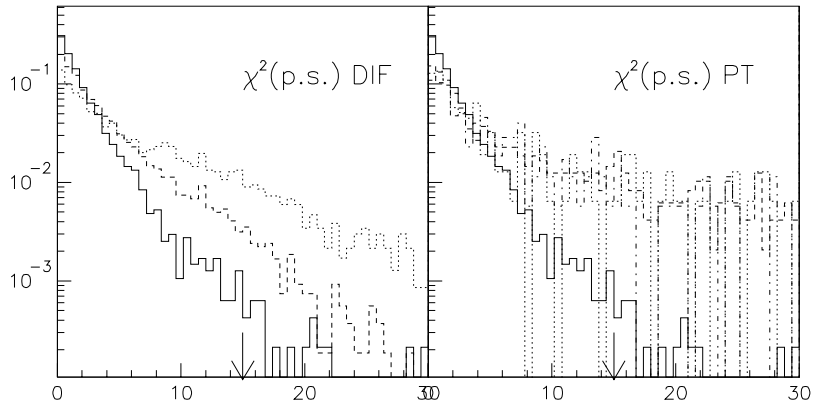

Figure 5.5: χ^2 for the consistence of the extrapolated track with the associated stub position and slope in the transverse plane. On the left are distributions for pion (dashed) and kaon (dotted) decay in flight, compared to prompt muons (solid). On the right distributions for pion (dashed), K^- (dotted), and K^+ (dot-dashed) punch- through are again compared to prompt muons (solid histogram). For muons with P_t below 20 GeV/c the cut is placed where indicated by the arrow

cut	$\pi^{\pm}$	K^-	K^+
stub quality	0.64	0.58	0.61
impact parameter	0.64	0.58	0.61
matching cuts	0.31	0.30	0.29

Table 5.2: The cumulative efficiency of the three groups of cuts studied on Monte Carlo PT samples. Only CMU numbers are reported since a very small fraction of the PT can reach the CMP. As expected the impact parameter cut has no effect on PT.

Type	Cuts	Notes
Event	$\|Z_{vx}\| < 30$ cm	(1)
	CTC,CMU and CMP in running order	
	2 CMU objects	
Track	$\|d\| < 3$ mm	
	$P_t > 3.0$ GeV	
	$N_{\text{CTC axial layers}} \geq 2$	
	$N_{\text{CTC stereo layers}} \geq 2$	
	CMP fiducial	(2)
CMU stub	$N_{TDC} \geq 3$	
	$N_{ADC} \geq 3$	
	$N_{CLUS} < 6$	
	$\|\delta z\| < \max(3\sigma, 8cm)$	
	$\chi^2(x, slope) < 15$	$p_t < 20$ GeV/c
	$\|\delta x\| < \max(3\sigma, 2cm)$	$p_t > 20$ GeV/c

Table 5.3: List of all cuts used to select the dimuon sample. (1) The cut on the event vertex position was built in the sample to ensure full SVX acceptance; (2) The extrapolated track must fall into the CMP fiducial volume within 5 cm;

requests on the event as listed in table 5.3, except for the Z_{vx} cut. It will be used as a sample of "almost pure" real muons on which the relative CMP efficiency for real muons is determined. This sample includes all the J/ψ candidate decays to dimuons. In our analysis only a fraction of the full run Ia sample is used, corresponding to 11.6 pb^{-1}.

On the J/ψ dimuon candidates, a dimuon invariant mass window cut ($2.8 < M_{\mu\mu} < 3.4$) and the request that muons have opposite charge are imposed.

For what concerns the muon quality cuts (second and third part of table 5.3) since we are interested on the relative CMP efficiency of a single real muon we will distinguish the two decay legs of the J/ψ candidate into a muon_leg, which is only used to establish the J/ψ mass peak, and a test_leg which is our "almost always real" muon. We select events where one of the muons passes the track and stub cuts in table 5.3 (test_leg), while the other (muon_leg) is required to pass the standard CDF Soft Lepton Tagging (SLT) selection [1] [41]. This is done to have a sample of higher statistics while retaining maximum purity; it has

[1]The Soft Lepton Tagging (SLT) selection is used to tag soft leptons from b decays in top candidate events; the main difference from our selection is that non CMP-fiducial muons are also accepted on the basis of tighter quality cuts

been seen in Chapter 3 that the CMU-CMP coverage is about 53% of the region $|\eta| < 0.6$, while the SLT covers about 90% of $|\eta| < 0.6$. The two muon tracks are then vertex-constrained. The test_leg candidate muons are thus an almost pure sample of real CMU muons, whose fake background can easily be estimated using a fit to the J/ψ invariant mass peak.

5.1.3 The $K_s^0 \rightarrow$"μ"π sample

Within the main dimuon "high mass" sample, we select a sample of pure fake single muon candidates by reconstructing K_s^0 decays into two pions where one of the decay legs has been identified as a muon.

First single muon candidates are selected passing all the cuts described in table 5.3 except the impact parameter cut (test_leg). Each muon candidate is then paired with all the tracks with P_t above 0.4 GeV, and impact parameter in excess of 0.1 cm (pion_leg); a vertex-constrained fit is subsequently performed between the two. The pair is accepted if the vertex constrained fit succeeds and if the reconstructed secondary vertex has a projected distance from the beam position larger than 5 cm and smaller than 25 cm. The 5 cm lower cut reduces the combinatorial background, whereas the upper 25 cm cut is meant to reject pion decay-in-flight within the CTC, and will be discussed later on.

The selection cuts and reconstruction procedure for the K_s^0 selection are summarized in table 5.4.

TEST LEG
As in table 5.3 except for the i.p. cut
PION LEG
$P_t > .4$ GeV $\|d\| > 0.1$ cm
SECONDARY VERTEX
$5 < \vec{d} \cdot \hat{P}_t < 25$ cm

Table 5.4: The K_s selection.

When the invariant mass of the "μ"-track pair is selected in a window around the K_s mass, the "μ" legs of the candidate K_s provide a sample enriched in fake muon. Furthermore the fraction of real and fake muons in this sample can be estimated by fitting the K_s mass peak.

5.1.4 Study of selection cuts on real data

The distributions examined in § 5.1.1 on single particle Monte Carlo samples can be studied on real data. To this purpose the J/ψ and K_s test_legs, which are somewhat representatives of the real and fake muon categories, will be used.

In figure 5.6 the distributions for the number of TDC and ADC hits, and the number of CMU clusters are compared for the two samples.

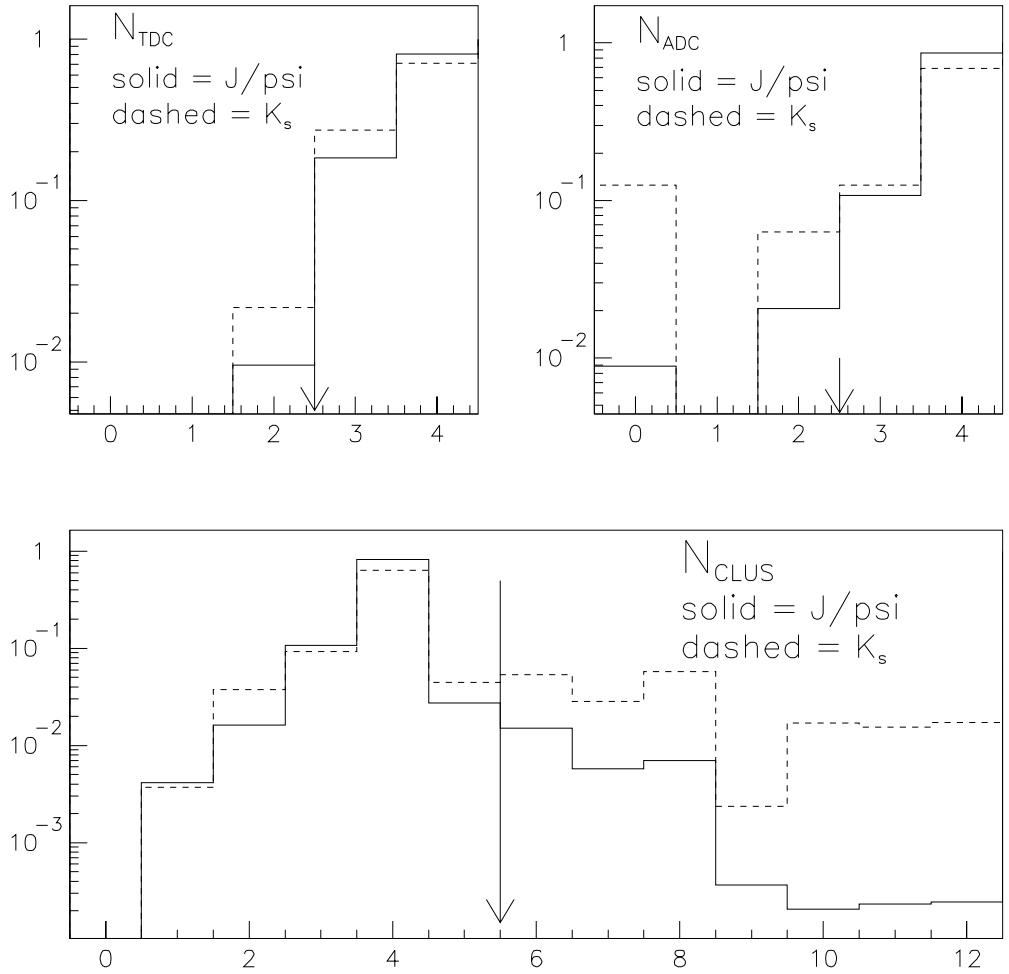

Figure 5.6: Top: The distribution of the number of CMU TDC (left) and ADC (right) hits for K_s test_leg candidate muons (dashed) which are fake-enriched, compared to that for J/ψ test_leg candidate muons (solid), which are true-muon-enriched. Bottom: The distribution of the number of CMU clusters for K_s test_leg's (dashed) compared to that for J/ψ test_leg's (solid).

In figure 5.7 the distributions of $N(\sigma_x)$, $N(\sigma_z)$ are examined and finally in fig. 5.8 the χ^2 distribution for the position/slope matching in the transverse plane is examined.

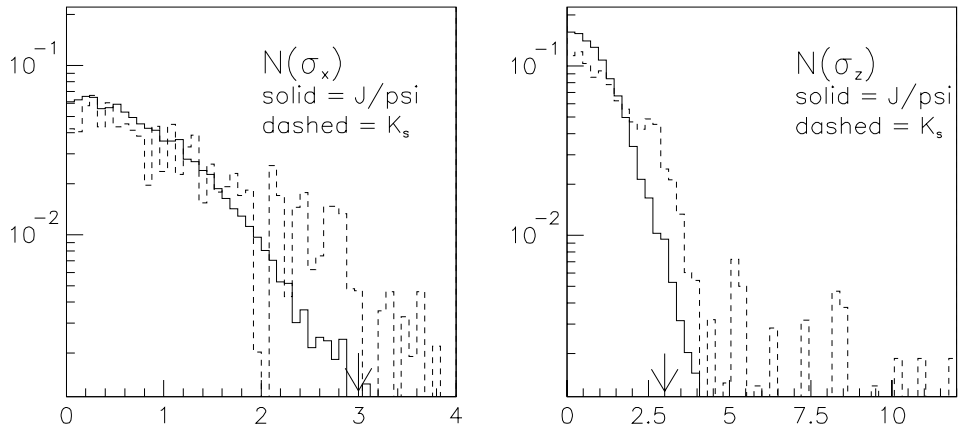

Figure 5.7: The distribution of the distance between the extrapolated CTC track and the CMU stub measured in σ's of multiple scattering in the transverse plane (left) and the z direction (right). The solid histograms are for J/ψ test_legs, the dashed ones for K_s test_legs.

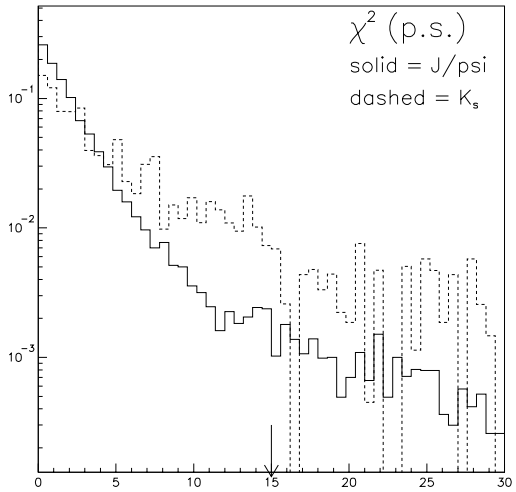

Figure 5.8: The distribution of the χ^2 for matching the position and slope of the extrapolated CTC track and the CMU stub. The solid histogram is for J/ψ test_legs, the dashed one for K_s test_legs

We observe differences between the J/ψ distributions and the K_s^0 ones which are similar to those between real and fake muons from the Monte Carlo. This had to be expected, since the J/ψ muons are enriched in real muons, while the K_s^0 ones are enriched in fake muons.

Finally the J/ψ and K_s samples are exploited to check the efficiency and rejection power of our selection cuts. To this purpose the cuts are applied one group at a time to the test_leg of J/ψ and K_s candidates; after each cut the pertinent invariant mass distribution is fit and the number of signal events is extracted by subtracting the background. The tables 5.5, 5.6 summarize the effect of the various cuts on the test_legs.

Note that the impact parameter cut cannot be tested on the K_s sample since a minimum impact parameter is required in the selection (see above).

	J/ψ test_leg +		J/ψ test_leg -	
cut	CMU	CMP	CMU	CMP
N_{TDC}	0.99	0.99	0.99	0.99
N_{ADC}	0.98	0.98	0.98	0.98
N_{CLUS}	0.95	0.95	0.95	0.96
impact parameter	0.94	0.95	0.95	0.95
matching cuts	0.88	0.89	0.89	0.90

Table 5.5: Cumulative cut efficiencies studied on real muons from J/ψ test_leg.

	$K_s \rightarrow$"μ^+"π^-		$K_s \rightarrow$"μ^-"π^+	
cut	CMU	CMP	CMU	CMP
N_{TDC}	0.99 ± 0.06	1.00 ± 0.09	0.98 ± 0.06	0.99 ± 0.09
N_{ADC}	0.95 ± 0.06	0.98 ± 0.09	0.93 ± 0.06	0.96 ± 0.09
N_{CLUS}	0.79 ± 0.05	0.88 ± 0.08	0.84 ± 0.05	0.92 ± 0.08
matching cuts	0.61 ± 0.04	0.78 ± 0.08	0.70 ± 0.08	0.80 ± 0.08

Table 5.6: Cumulative cut efficiencies studied on fake muons from $K_s^0 \rightarrow$ "μ"π.

5.2 Technique to evaluate the number of real muon pairs

We have previously introduced a technique to evaluate the number of real CMU single muons involving the relative efficiency of real and fake muons seen in the CMU to give a CMP stub. Before discussing this technique in detail, in order to extend it to the more complex case of events with muon *pair* candidates, we try to get a rough estimate of the probability for a hadron to give a CMU or a CMP stub. This will be used to justify various assumptions in the subsequent discussion.

With a very crude approximation we compute the probability for a given hadron to reach the CMU chambers when exiting the interaction region at $\theta = 90^o$, neglecting the effect of ionization losses and the trajectory straggling due to multiple scattering. To this purpose the number of interaction lengths traversed in the material is computed as a function of the initial energy of the particle, using measurements and extrapolations from higher energies of the hadron-Fe and hadron-nucleon cross sections [40], and an average composition of the calorimeter material. Hadrons that decay in flight to $\mu\nu$ prior to reach the calorimeter (DIF), and hadrons traversing a length in the material and then decaying to $\mu\nu$ are also considered in this computation. The total fake probability as functions of P_t is shown in fig. 5.9a for pions and kaons separately. In fig. 5.9b the probability of noninteracting punchthrough is shown separately for K^+, K^- and $\pi^\pm$ as a function of the particle P_t. These plots are obtained assuming that no muon track is lost due to bad track reconstruction or poor matching of the track with the stub. Because of all the approximations made, the plots are overestimates of the true probabilities of these particles being identified as muons.

From fig. 5.9a and 5.9b we learn that:

1. the DIF and PT will contribute a relevant fraction of the low-P_t muons, since the overall fake probability is of order few percent;

2. a non-negligible fraction of the CMU fake muons are PT;

3. K^+ fakes have the highest contribution from PT, while K^- and $\pi^\pm$ has a much smaller contribution (this is due to the much smaller interaction cross section for K^+ with respect to K^- or pions, which in turn is due to the K^+ quark composition $K^+ = \bar{s}u$).

We then proceed to explore the possibility that hadrons give a signal in the CMP chambers. To obtain the overall probability of a hadron to hit the CMP

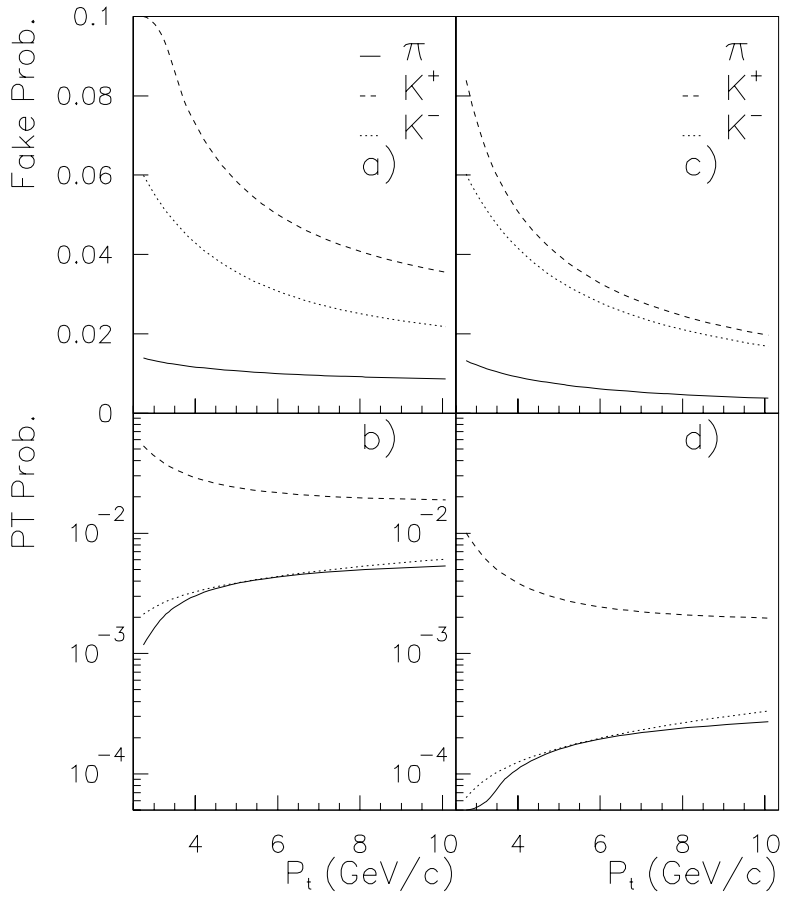

Figure 5.9: a) The overall probability for a hadron to reach the CMU as a function of P_t; b) Non-interacting punchthrough probability to CMU as a function of P_t. c) The overall probability for a hadron to reach the CMP as a function of P_t; d) Non-interacting punchthrough probability to CMP as a function of P_t.

either as PT or DIF, the CMP is schematized as a 60 cm iron plate and a system of chambers at 5 m from the interaction point (strictly true only at $\theta = 90^o$), and resulting probabilities are shown in fig. 5.9c for the overall fake probability and 5.9d for the PT probability.

The PT probability in the CMP (fig. 5.9d) is reduced by more than one order of magnitude with respect to the CMU (fig. 5.9b), so that it is reasonable to expect PT to be negligible at the CMP level. Therefore the category of fake muons as a whole is expected to have a lower average relative CMP/CMU efficiency with respect to real muons from any "prompt" source[2], which should be nearly 100 % efficient. However it is clear that the value of this efficiency is different for different hadrons. In real life neither real muons nor DIF fakes will have 100 % CMP relative efficiency. In general it is expected that the DIF efficiency be slightly less than that for real muons because of the effect of the decay kink. The bottom line is that the CMP is able to distinguish real muons from fakes because of their different relative efficiencies, and that *each* hadron species has a relative efficiency smaller than real muons.

The other relevant conclusion is that, because of the smaller interaction cross-section of K^+, we must expect a larger amount of positively charged candidate muons in the CMU which are actually kaon punchthrough, and since they have a different probability than K^- to reach the CMP, we will have to handle positive and negative fakes separately.

Although in high energy $\bar{p}p$ collisions a fair amount of protons and anti-protons is also produced, only pions and kaons have been discussed as sources of PT and DIF. This is because the kaons and pions constitute indeed the bulk of the fake muons. This statement will be discussed and justified later on (§ 5.5.3).

5.2.1 Single muon equations

We first consider the case of single muons, already discussed in the introduction to this chapter.

Because of the different fake probability for K^+ and K^-, it is expected, in general, that the fake CMP relative efficiency be different for positive and negative charges, therefore the set of equations (5.1, 5.2 and 5.3) will be extended, using the same notation. For each sign the total number of events ($N_U^{\pm}$) is the sum of the number of events where the muon is fake ($F^{\pm}$), plus the number of events where the muon is true ($M^{\pm}$). Let then ϵ_μ be the relative probability of a true CMU muon to reach the CMP (this is irrespective of the electric charge), ϵ_f^+ and

[2]Here prompt indicates truly prompt sources such as Drell-Yan, Υ and Z^0, as long as short lived particles such as b hadrons

ϵ_f^- those for positively and negatively charged fakes, respectively. The numbers of events in the CMP ($N_P^\pm$) are given by:

$$\begin{cases} N_P^+ = \epsilon_\mu M^+ + \epsilon_f^+ F^+ \\ N_P^- = \epsilon_\mu M^- + \epsilon_f^- F^- \end{cases} \tag{5.4}$$

whereas, as stated above:

$$N_U^+ = M^+ + F^+$$

$$N_U^- = M^- + F^-$$

Let us assume that ϵ_μ has been measured (it is relatively easy to measure it from data); then if $M^+ = M^-$ is assumed, as is natural, there are four equations and five unknowns, $M^+ = M^- = M$, F^+, F^-, ϵ_f^+, ϵ_f^-. The set of equations can be solved for M with respect to ϵ_f^-, ϵ_μ, N_U^-, and N_P^-:

$$M^- = \frac{N_P^- - \epsilon_f^- N_U^-}{\epsilon_\mu - \epsilon_f^-}; \tag{5.5}$$

F^- and F^+ can then be obtained by subtraction. Therefore we do not need to measure ϵ_f^+ in order to calculate M; ϵ_f^+ itself can instead be obtained from the equations themselves as a function of ϵ_f^-, ϵ_μ, N_U^-, N_P^-, N_U^+, and N_P^+ :

$$\epsilon_f^+ = \frac{N_P^+ - N_P^- - \epsilon_f^-(N_U^- - M^-)}{N_U^+ - M^-}; \tag{5.6}$$

To solve the system we need $\epsilon_\mu \neq \epsilon_f^\pm$. The type of fake muons is not relevant, as long as a common (average) relative efficiency $\epsilon_f^\pm$ can be defined, and the relative efficiency for each type of fake is appreciably different from the one for true muons (otherwise that type of fakes is completely indistinguishable from real muons).

This technique involves the problem of determining ϵ_μ and ϵ_f^-. It is possible to obtain ϵ_μ from a J/ψ sample, studying the relative efficiency of a fiducial decay leg. The determination of ϵ_f^- can be more critical. It is in fact the weighted average of the relative CMP efficiency over several species: PT and DIF respectively from π^- and K^-. These can and will have very different values, as one can infer from fig. 5.9; therefore, using a sample with e.g. only pion fakes, or with a different proportion of DIF and PT to measure ϵ_f, will give an experimental value which is different from the "true" one for the fake composition in our sample.

The stability of the above equations under a mismeasurement of ϵ_f^- can be studied as follows. Consider an hypothetical experiment in which the number of fake muons at the CMU is $\bar{F}$ (the charge superscript is omitted everywhere for

simplicity); then we define $\bar{f} = \bar{F}/N_U$, so that $\bar{M} = N_U(1-\bar{f})$ is the number of real muons. From these we obtain the total number of muon candidates we expect in the CMP as

$$N_P = N_U(1-\bar{f})\epsilon_\mu + N_U\bar{f}\epsilon_f$$

If the expression in (5.5) is used to obtain the true fraction, then the fractional difference from $\bar{M}$, $\Delta m = M(\epsilon_f)/\bar{M} - 1$ can be obtained. It is given by:

$$\Delta m = \frac{|M-\bar{M}|}{\bar{M}} = \frac{\delta_\epsilon \epsilon_f \bar{f}}{(\epsilon_\mu - \epsilon_f)(1-\bar{f})}. \tag{5.7}$$

which corresponds to the error on the experimental measurement of M, for a given fake fraction $\bar{f}$, due to a fractional uncertainty δ_ϵ on the measurement of ϵ_f.

We expect the relative efficiency for real muons to be quite close to 1; a reasonable guess is that $\epsilon_{\rm DIF}$ is also close to 1 (although it must be lower than for real muons); on the other side $\epsilon_{\rm PT}$ must be close to 0 (see fig. 5.9). We will see later on that DIF and PT are about the same amount at the CMU level, so that $f_{\rm PT} = 0.5$; then since

$$\epsilon_f = \epsilon_{\rm PT} f_{\rm PT} + \epsilon_{\rm DIF}(1-f_{\rm PT})$$

is the expected fake efficiency, we can assume $\epsilon_f = 0.5$. Using these numerical values, the fractional error on M as a function of the fake fraction $\bar{f}$ in the CMU has been plotted in figure 5.10, for various values of δ_ϵ. It can be seen that if $\bar{f}$ is large, a deviation up to 100% from the true M is induced by just a 10% uncertainty on the measured ϵ_f. It is then clear that a CMU sample as pure as possible is needed in order to minimize the effect of the experimental error on the determination of ϵ_f.

5.2.2 Dimuon equations

The procedure described previously to determine M can be extended straightforwardly to the case of events with a muon *pair* candidate, with only a little more algebra. The definitions of CMU and CMP muon introduced above are retained. We then define three categories of pairs: CMU-CMU, CMU.not.CMP-CMP, and CMP-CMP. The CMU.not.CMP-CMP category is the class with a CMP candidate (which is also a CMU candidate) and a CMU.not.CMP candidate, i.e., a CMU muon candidate *without* a corresponding CMP stub. This will be a subset of CMU-CMU, but will be disjoint from CMP-CMP, as shown in fig. 5.11. In the following the shorthands UU, UP, and PP will be used to indicate

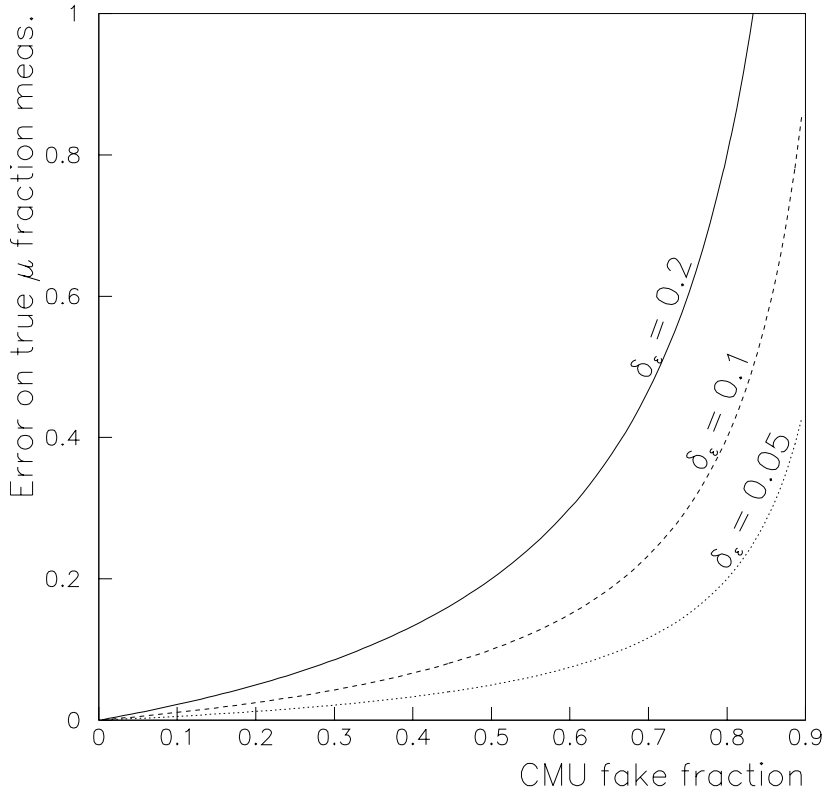

Figure 5.10: Fractional error on the experimental determination of the number of real muon pairs as a function of the fake CMU fraction for various values of the fractional error on ϵ.

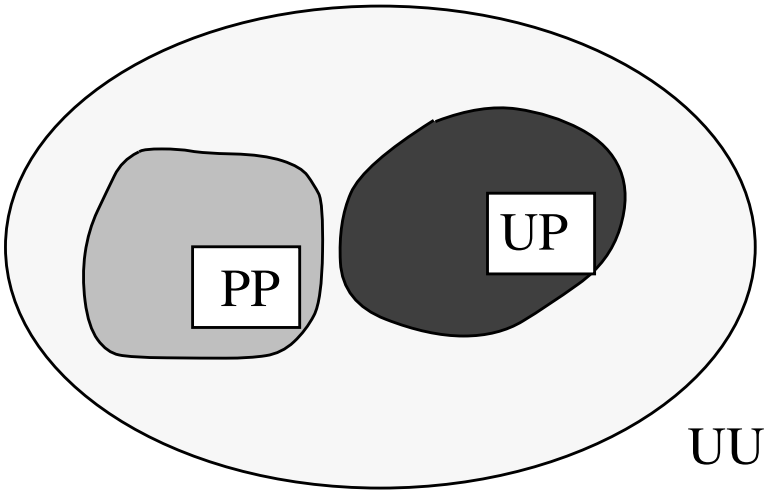

Figure 5.11: Venn diagram showing the relation between the UU, UP and PP sets of muon candidate pairs

CMU-CMU, CMU.not.CMP-CMP, and CMP-CMP. A further subdivision will distinguish negative like-charge pairs ($--$), positive like-charge pairs ($++$), and opposite charge pairs ($+-$).

We first write the expression for the total number of $--$ pairs in the UU category:

$$N_{\rm UU}^{--} = M^{--} + F_1^{--} + F_2^{--} \tag{5.8}$$

Where M^{--} is the number of **true** negative muon pairs, F_1^{--} the number of **fake-true** pairs and F_2^{--} the number of **fake-fake** pairs; this notation will be used also for the other charge combinations. The populations of the other two categories are then written using single particle relative probabilities introduced in the previous section and the unknown fractions M^{--}, F_1^{--} and F_2^{--}:

$$\begin{aligned} N_{\rm UP}^{--} &= 2\epsilon_\mu(1-\epsilon_\mu)M^{--} + \{\epsilon_\mu(1-\epsilon_f^-) + \epsilon_f^-(1-\epsilon_\mu)\}F_1^{--} \qquad (5.9)\\ &+ 2\epsilon_f^-(1-\epsilon_f^-)F_2^{--} \\ N_{\rm PP}^{--} &= \epsilon_\mu^2 M^{--} + \epsilon_\mu\epsilon_f^- F_1^{--} + \epsilon_f^{-2}F_2^{--} \qquad (5.10) \end{aligned}$$

For the $++$ combinations an analogous set of equations can be written:

$$\begin{aligned} N_{\rm UU}^{++} &= M^{--} + \gamma F_1^{--} + \gamma^2 F_2^{--} \qquad (5.11)\\ N_{\rm UP}^{++} &= 2\epsilon_\mu(1-\epsilon_\mu)M^{--} + \{\epsilon_\mu(1-\epsilon_f^+) + \epsilon_f^+(1-\epsilon_\mu)\}\gamma F_1^{--} \qquad (5.12)\\ &+ 2\epsilon_f^+(1-\epsilon_f^+)\gamma^2 F_2^{--} \\ N_{\rm PP}^{++} &= \epsilon_\mu^2 M^{--} + \epsilon_\mu\epsilon_f^+\gamma F_1^{--} + \epsilon_f^{+2}\gamma^2 F_2^{--} \qquad (5.13) \end{aligned}$$

where it has been kept into account that the number of true LS muon pairs M is expected to be independent of the charge of the pair

$$M^{++} = M^{--}$$

and

$$\gamma = \frac{F_1^{++}}{F_1^{--}} = \frac{F_1^{+-,p}}{F_1^{+-,n}}.$$

is introduced to make the relation between F_i^{++}, F_i^{--} explicit ($F_1^{+-,p}$,$F_1^{+-,n}$ indicating real-fake opposite charge pairs with positive fake and negative fake, respectively). Once we know ϵ_μ then the set of equations (5.8, 5.9, 5.10) can be solved completely with respect to ϵ_f^-. To obtain ϵ_f^+ from the set of equations (5.11, 5.12, 5.13) a quadratic equation is solved, and therefore we obtain two solutions: the first increases with increasing ϵ_f^- whereas the second decreases. We take the increasing one since it is physically sensible that the relative efficiencies for positively and negatively charged particles increase and decrease concurrently.

An independent set of equations holds for the OS category:

$$\begin{aligned}
N_{\rm UU}^{+-} &= M^{+-} + F_1^{+-} + F_2^{+-} && (5.14)\\
N_{\rm UP}^{+-} &= 2\epsilon_\mu(1-\epsilon_\mu)M^{+-} + \{\alpha^+[\epsilon_\mu(1-\epsilon_f^+) + \epsilon_f^+(1-\epsilon_\mu)] && (5.15)\\
&+ \alpha^-[\epsilon_\mu(1-\epsilon_f^-) + \epsilon_f^-(1-\epsilon_\mu)]\}F_1^{+-}\\
&+ \{\epsilon_f^+(1-\epsilon_f^-) + \epsilon_f^-(1-\epsilon_f^+)\}F_2^{+-}\\
N_{\rm PP}^{+-} &= \epsilon_\mu^2 M^{+-} + \{\alpha^+\epsilon_\mu\epsilon_f^+ + \alpha^-\epsilon_\mu\epsilon_f^-\}F_1^{+-} + \epsilon_f^+\epsilon_f^- F_2^{+-} && (5.16)
\end{aligned}$$

where ϵ_f^+ is obtained from the LS equations, ϵ_μ is the same as above, and:

$$\alpha^+ = \frac{\gamma}{1+\gamma},\ \alpha^- = \frac{1}{1+\gamma}$$

are introduced to simplify the notation. Again the set of equations is solved with respect to ϵ_f^-.

Using this technique the number of true pairs can be extracted, provided that the number of pairs (N's) in the various sign-type combinations, and the two relative efficiencies for true and fake negatively-charged muons have been measured independently.

5.3 Determination of the N's

In our sample of "high mass" dimuons, after the cuts discussed in § 5.1.1 are applied, pairs are selected in an invariant mass window $5 < M_{\mu\mu} < 50$. The lower

cut is applied to reject same-side sequential B decays, whereas the upper cut rejects Z decays, and it only eliminates few events. Both same side sequentials and Z decays only give opposite charge dimuons, but the invariant mass cuts are applied regardless of the charges, in order to preserve equal acceptance to opposite sign (OS) and like sign (LS) muons. The muon pair candidates in the nine categories defined by charge combinations and the presence or absence of a CMP stub are counted. The number of candidates in each category is shown in table 5.7.

	$+-$	$++$	$--$
CMU-CMU	8186	3080	2329
CMU.not.CMP-CMP	2327	1285	860
CMP-CMP	5255	1377	1236

Table 5.7: Composition of the dimuon sample.

The distributions of the invariant mass of the pair, for each of the nine categories, are shown in fig. 5.12 after the invariant mass cuts have been applied. The Υ peak around $M_{\mu\mu} \simeq 10$ GeV is clearly visible in the UU and PP opposite sign distributions. The peak does not appear in the UP subsample, indicating that a true muon pair (at least one from Υ decay) will most likely be a PP, because a real muon passing the cuts has a low probability not to reach the CMP; so the class UP (= CMU.not.CMP-CMP) contains mostly fake-true pairs.

The distribution of the transverse momentum for all the muon candidates in the sample is shown in fig. 5.13. This will be referenced later on, when dealing with the determination of ϵ_f.

Events with more than one muon pair

In a few cases we are presented with the problem that more than one pair in the event satisfies our cuts, for example muon 1,2,3 pass the single muon selection and $M_{1,2}$, $M_{1,3}$ are both within the allowed invariant mass intervals. In this case the most conservative choice would be to discard the whole event from the analysis. We choose to keep all pairs in these events and include the double counts in the computation of background. Out of a total of 53856 events examined 14564 have one or more pairs entering the distributions. 14486 have one pair, only 70 have two pairs, and 8 have three pairs. This accounts for the sum or the first row in table 5.7.

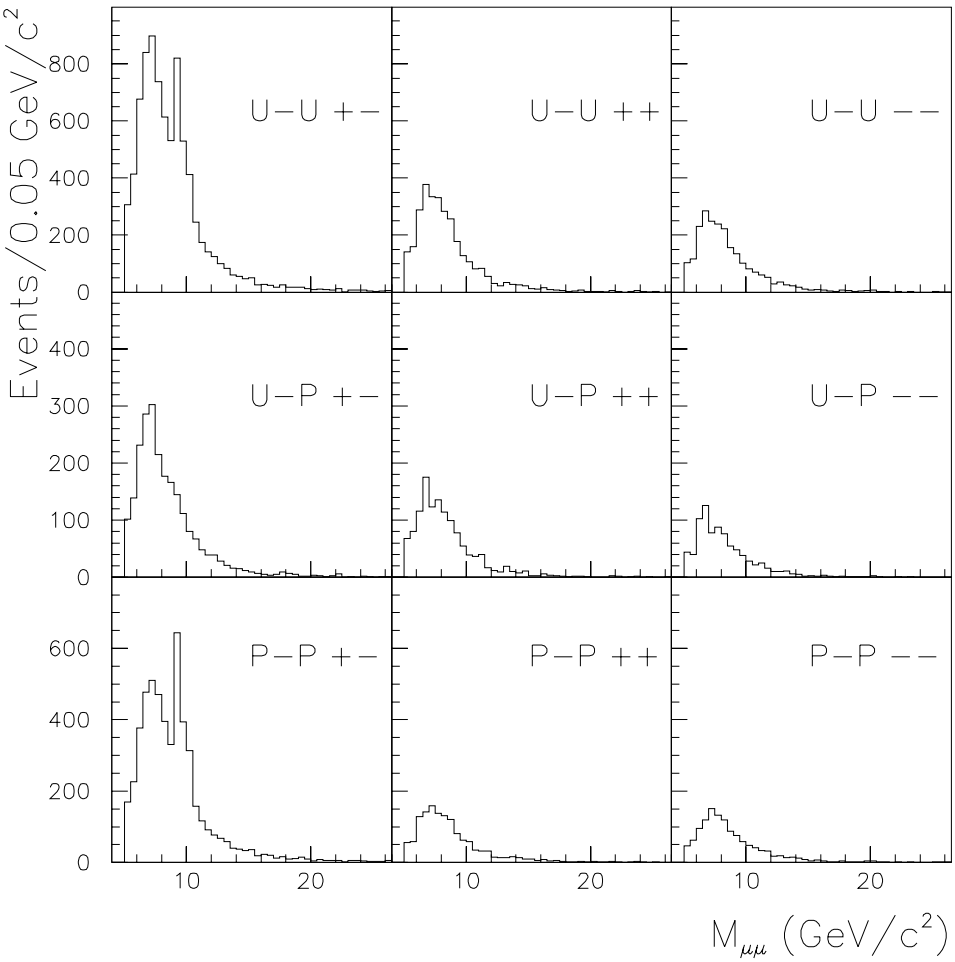

Figure 5.12: Invariant mass distribution of the muon pairs in the nine categories described in the text.

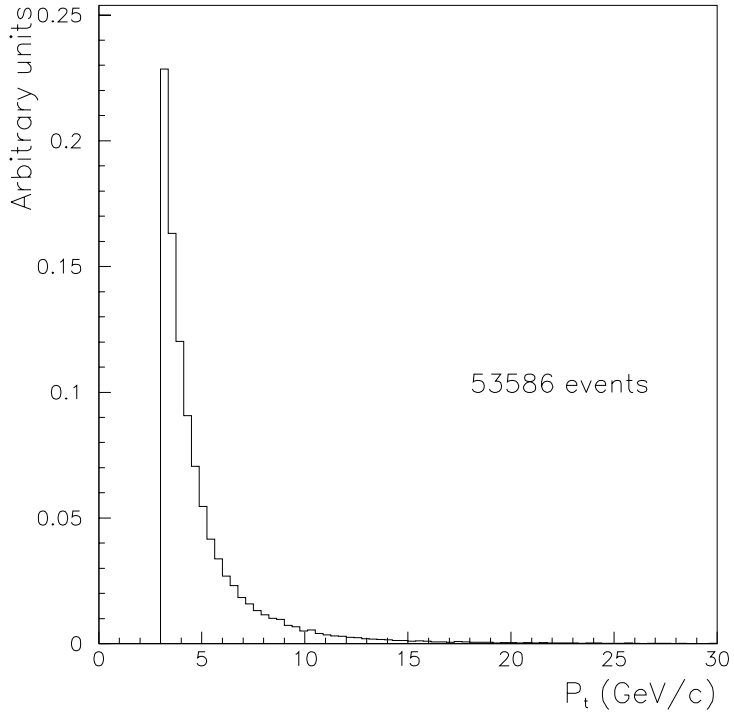

Figure 5.13: Transverse momentum distribution (in arbitrary units) of all the muon candidates passing the cuts. Indicated is the number of events in the sample containing at least a candidate CMU muon passing the single muon cuts.

Υ mass window cut

In fig. 5.14 the invariant mass distribution for the 3 OS categories is enlarged around the Υ peaks; the peaks are clearly visible even for higher lying states.

To get rid of the Υ decays we cut away a mass window between 9 GeV, more than 4 sigma below the $\Upsilon(1S)$ peak, and 10.8 GeV, well above the $\Upsilon(3S)$ invariant mass of 10.36 GeV. After cutting the Υ window we are left with a sample whose

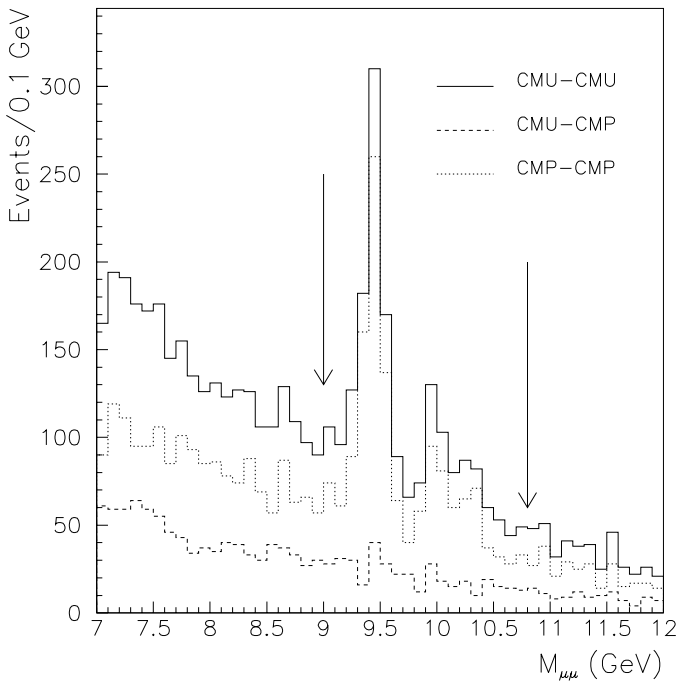

Figure 5.14: Invariant mass distribution of OS muon pairs. Arrows indicate the invariant mass window cut. The cut is applied to LS pairs as well for acceptance consistency.

population is described in table 5.8.

The difference between the second and third columns in table 5.8 indicates the presence of a large number of fake muon pairs from residual background. The different punchthrough probability for K^+ and K^-, is in fact the main responsible for this charge imbalance. We see on the other side that the UP category is the one with the highest fractional difference (remember that UP indicates that one muon is CMU.not.CMP, which is very unlikely for a real CMP fiducial muon, but quite likely for a fake), whereas this fractional difference is small for PP,

	+−	++	−−
CMU-CMU	6278	2616	1962
CMU.not.CMP-CMP	1948	1091	731
CMP-CMP	3810	1153	1024

Table 5.8: Composition of the dimuon sample after the Υ cut.

indicating that the CMP takes care quite well at least of the punchthrough. The residual imbalance is due to the small fraction of punchthrough surviving the CMP iron.

In § 5.6 the numbers of table 5.8 will be used to obtain the M's from the dimuon equations.

5.4 Determination of ϵ_μ

To estimate ϵ_μ we use muons from the J/ψ 's test_legs. In the J/ψ sample the invariant mass is formed separately for positive and negative test_leg J/ψ 's; a separate distribution is made for the subclass of events where the test_leg has a CMP stub. By definition ϵ_μ is the ratio of the number of J/ψ 's with test_leg in the CMP over the total number of J/ψ 's. The background subtraction is made using two methods: on the basis of a fit to the invariant mass distribution using a gaussian plus a second degree polynomial background, and, independently, by subtracting from the peak the average of the two sidebands. The number of good J/ψ 's is taken as the integral of a 3σ interval of the mass histogram around the fitted mass, after background subtraction. Fig. 5.15 shows the mass distribution for CMU+, CMU−, CMP+ and CMP− test_legs. The signal band is between the two straight solid lines, while the sidebands are taken in the regions between the dotted lines and the histogram limits. The integral of the sidebands is normalized to the ratio of the intervals before being subtracted from the integral under the peak. The signal and background integrals in the regions indicated are summarized in table 5.9. All the signal relative efficiencies, obtained with the two methods and for different μ charge, agree within errors. We also calculate the relative efficiencies for the test_legs in background events under the J/ψ peak, ϵ_{bkg}; these are obtained as the ratio of the integral of the background under the signal peak CMP and that under the signal peak CMU (fit), or as the ratio of the number of events in the sidebands of the CMP spectrum to the number of events in the sidebands of the CMU spectrum. These, as expected,

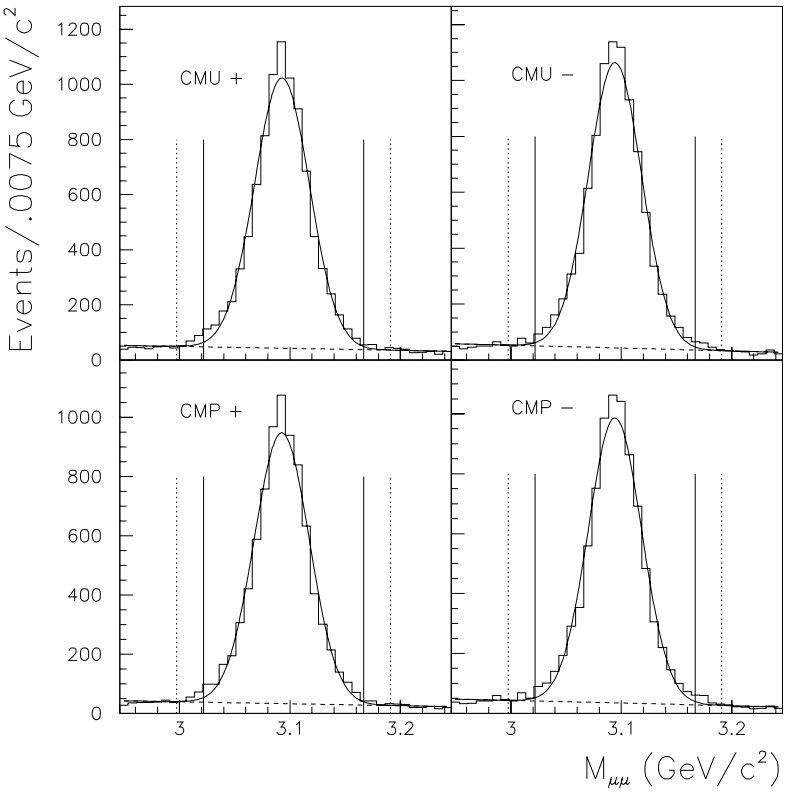

Figure 5.15: Invariant mass distributions of J/ψ 's with positive (right) and negative (left) test_leg. The case where test_leg has also a stub in the CMP is shown separately (bottom).

	CMU+	CMU−	CMP+	CMP−
Signal + Bkg	9092	9203	8356	8511
Background Fit	841	855	651	693
Background Sidebands	817	820	637	664
Signal - Fit	8251±95	8348±96	7705±91	7818±92
Signal - Sidebands	8275±95	8383±96	7719±91	7847±92
ϵ_μ S-Fit			0.933±0.0153	0.937±0.0154
ϵ_μ S-SB			0.933±0.0154	0.936±0.0153
ϵ_{bkg} (fit)			0.77	0.81
ϵ_{bkg} (SB)			0.78	0.81

Table 5.9: Summary of J/ψ events with various sign-type combinations of the test_leg, and resulting values for ϵ_μ

are lower than ϵ_μ. Putting all together, and averaging over the two charges, we obtain $\epsilon_\mu = 0.935 \pm 0.011$ from the fit, and $\epsilon_\mu = 0.934 \pm 0.011$ from the sideband subtraction. We take the value $\epsilon_\mu = 0.935 \pm 0.011$.

Solutions of the dimuon equations as functions of ϵ_f^-

The numbers in table 5.8, corresponding to the N_{UU}'s, N_{UP}'s and N_{PP}'s in the equations, are now inserted into the analytical solutions of the equations themselves, along with the estimate for ϵ_μ. The curves for the dependence of the various fractions on ϵ_f^- are shown in fig. 5.16, where the uncertainty on the solution due to statistical fluctuations of the N's, and the measurement uncertainty on ϵ_μ is also shown.

To keep into account the correlations in the fluctuations of the various numbers of events, the error on the curves is obtained as follows: the total numbers, N_{UU}'s, are extracted using a poissonian distribution with mean equal to the measured number of UU pairs; for each sign combination, from the generated N_{UU} the sum $N_{UP} + N_{PP}$ is extracted using a binomial with success probability equal to the measured ratio $\frac{UP+PP}{UU}$; N_{PP} is then extracted using a binomial with success probability equal to the measured ratio $\frac{PP}{UP+PP}$; finally N_{UP} is obtained by subtraction. ϵ_μ is independently extracted from a normal distribution with mean given by the experimental value and σ given by its error. For any given value of ϵ_f^- the extraction is repeated many times to obtain a distribution of solutions for the M's and F's.

The 1σ variation of the solutions is indicated by the bands in fig. 5.16.

The darkest band in each of the three plots describes the behaviour of the fake-real fractions F_1; it crosses the x-axis for some value of ϵ_f. Of course a negative fraction of fake-real pairs has no physical meaning, therefore the value at which $F_1 = 0$, which is only known up to the error band in figure, is an upper limit on the values ϵ_f can take up. This will be used later on when estimating the true muon fractions.

5.5 Determination of ϵ_f^-

As discussed in section 5.2, the value of ϵ_f^- is different for any given di-muon candidate sample, as it depends on the relative amount of fake muons from pions and kaons, and on whether this hadrons made it to the CMU via punchthrough or decay in flight.

Therefore the task of measuring directly ϵ_f^- for our sample, whose background composition is unknown, is not a straightforward one. One possibility would

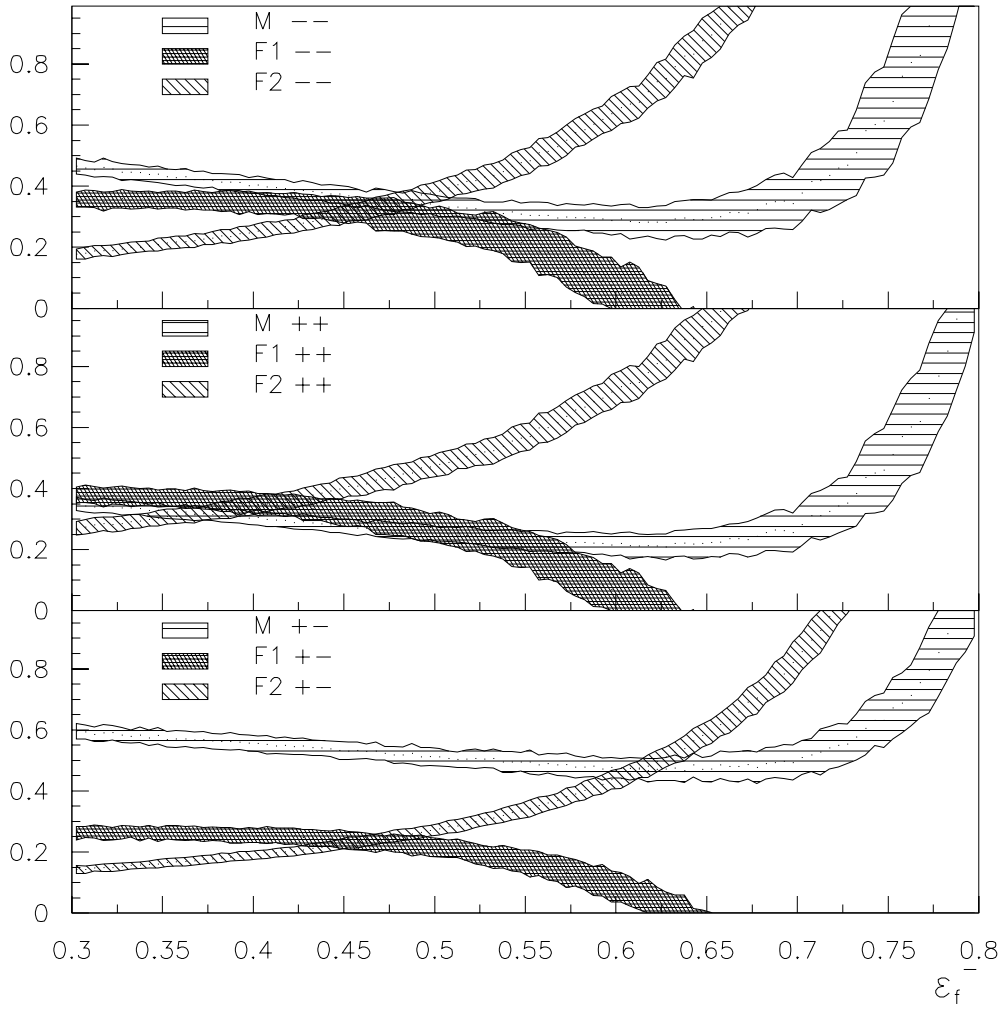

Figure 5.16: Solution of the dimuon equations as a function of ϵ_f. The hatched bands show the 1σ variation due to the statistical fluctuations in the measured number of dimuon candidates in CMU and CMP and to the experimental uncertainty on ϵ_μ.

be to make extensive use of Monte Carlo simulation to estimate the relative CMP efficiency for all categories of fakes, and combine it with an estimate of the π/K ratio in our sample. This looks quite unattractive, as the absolute value of efficiencies depends critically on having the exact amount and kind of material modeled in the simulation, and π/K ratio as a function of p_t is a rather poorly known quantity[35]. We wil rather try to use the data themselves to measure efficiencies, and will use Monte Carlo simulation only as far as efficiency ratios are concerned.

On the other hand, we do not need a precise value for ϵ_f^-. As can be seen from figure 5.16 the dependence of the true muon fractions on ϵ_f^- is rather weak, and there is already an upper limit $\epsilon_f^- \leq 0.63$ from the requirement that all muon fractions (true and fakes) must be positive (see the previous section).

It is therefore apparent that if a lower bound to ϵ_f^- can be found, close enough to the upper limit, we can still solve the dimuon equations with a reasonably small uncertainty.

We will follow this strategy in two steps. First we show that in our sample the value for ϵ_f^- for pions ($\epsilon_f^{\pi^-}$) is smaller than for kaons ($\epsilon_f^{K^-}$), therefore, although we do not know the relative amount of K and π in our sample, we can use $\epsilon_f^{\pi^-}$ as our lower limit. After this, we will show how a lower limit for $\epsilon_f^{\pi^-}$ can be obtained from our data using the decay $K_s^0 \to \pi^+\pi^-$. Finally, we discuss the anti-proton contribution to ϵ_f^- and present a cross-check on $\epsilon_f^{K^-}$ using the decay $\phi \to K^+K^-$.

5.5.1 ϵ_f^{π} vs. $\epsilon_f^{K^-}$

Given a sample of π or K mesons, the corresponding ϵ_f^-'s can be written as:

$$\epsilon_f^{K^-} = \epsilon_{DIF}^{K} f_{DIF}^{K^-} + \epsilon_{PT}^{K^-}(1 - f_{DIF}^{K^-}) \quad (5.17)$$

$$\epsilon_f^{\pi} = \epsilon_{DIF}^{\pi} f_{DIF}^{\pi} + \epsilon_{PT}^{\pi}(1 - f_{DIF}^{\pi}) \quad (5.18)$$

where $\epsilon_{\rm DIF}^{K^-}$ is the relative efficiency for being reconstructed in the CMP for a K-meson which made it to the CMU via Decay In Flight, and $\epsilon_{\rm PT}^{K^-}$ is the same for a K-meson which made it to the CMU via Punch Through; the relative fractions of the two kinds of K-mesons in the CMU are f_{DIF} and $f_{PT} = 1 - f_{DIF}$. Analogous notations are used for π-mesons. It should be noted that distinguishing between efficiency for positive and negative mesons of the same kind is only relevant for what concerns the punch through probability of kaons, therefore we simplified the notation by dropping the sign wherever irrelevant.

We now make the statement:

$$\epsilon_{DIF}^{K} \simeq \epsilon_{DIF}^{\pi} \quad (5.19)$$

$$\epsilon_{PT}^{K^-} \simeq \epsilon_{PT}^{\pi} \quad (5.20)$$

The first equation is motivated by the following consideration: once a meson has decayed before the CMU, thus producing a muon whose CMU stub matches the CTC track, this muon will most of the times traverse the absorber in front of the CMP and give a stub in the CMP as well. Since our requirements on CMP matching is very loose, we do not expect a significant drop in efficiency for kaons due to their wider opening angle in the decay. This is confirmed by a Monte Carlo simulation of the detector for single pion or kaon tracks generated in our kinematical range. The results of such simulation are shown in table 5.10.

P_t	π	K
3 GeV/c	0.71 ± 0.04	0.72 ± 0.08
6 GeV/c	0.92 ± 0.04	0.89 ± 0.07
9 GeV/c	0.92 ± 0.04	0.91 ± 0.07

Table 5.10: $\epsilon_{\rm DIF}$ from single particle Monte Carlo samples generated at different P_t.

The second equation is a straightforward consequence of the fact that the interaction length in iron is almost the same for negative charged kaons and pions (§ 5.2), and can again be checked using a Monte Carlo simulation of the detector. Since the punchthrough probability is very small, the Monte Carlo with full detector simulation is very inefficient. Therefore only a small statistics was obtained, showing that all the three relative efficiencies for $\pi^\pm$ K^+ and K^- punchthrough are very close and less then 10 %. The absolute probabilities to the CMU are of the same order.

The above arguments allow us to drop the meson kind from the relative efficiency symbol and write:

$$\epsilon_f^{K^-} \simeq \epsilon_{DIF} f_{DIF}^{K^-} + \epsilon_{PT}(1 - f_{DIF}^{K^-}) \quad (5.21)$$

$$\epsilon_f^{\pi} \simeq \epsilon_{DIF} f_{DIF}^{\pi} + \epsilon_{PT}(1 - f_{DIF}^{\pi}) \quad (5.22)$$

Once we notice that $\epsilon_{DIF} >> \epsilon_{PT}$ (see section 5.2), it is clear that the condition for $\epsilon_f^\pi < \epsilon_f^{K^-}$ is $f_{DIF}^\pi < f_{DIF}^{K^-}$, i.e. we have to prove that in our data sample the relative fraction of pions that reach the CMU thanks to decay in flight is lesser than for kaons.

We already saw that the punch through probability is about the same for π and K^-. As far as decay in flight are concerned, there are two main differences between kaons and pions, that push in opposite directions:

1. The kaon mean life is 2.1 times shorter then the pion one ($c\tau_K \simeq 3.7$m vs. $c\tau_\pi \simeq 7.8$m), also for the same p_t the boost of the pion is about 3.5 times bigger than the kaon ($m_\pi \simeq 140$ MeV, $m_K \simeq 494$ MeV); these combine to make the probability for a kaon to decay in any given volume ~ 7.4 larger than for a pion.

2. When mesons decay into a $\mu\nu$ pair, the different rest mass for the pion and kaon causes the opening angle of decay pair in the laboratory frame to be wider in the $K \to \mu\nu$ case. As a consequence the angle between the muon track and the meson track (kink) is larger for kaons. In spite of the larger pion boost, the maximum kink turns out to be 10 mrad for pions, and 70 mrad for kaons of P_t of 3 GeV/c^2. A large kink, implies a chance that the muon be discarded by the analysis cuts, for one of the following reasons:

   - if the kink is in the middle of the CTC volume, the two pieces of the track before and after the kink may match so badly that no track is found by the pattern reconstruction algorithm
   - if the kink is close to the interaction point, the reconstructed CTC track will not point to the vertex, thus failing the impact parameter cut $d < 3$ mm
   - if the kink is close to the calorimeter, the meson track will be correctly reconstructed and accepted, but the CMU stub will be outside the matching window. This last possibility is much more important for kaon decay, since the typical pion kink is about the same as the average multiple scattering angle for muons in the calorimeter iron

   this implies that it is comparatively more difficult for a kaon to make a CMU muon via decay in flight.

We need a Monte Carlo simulation to decide whether the combined effect of 1. and 2. above results in ϵ_{DIF} to be larger for pions or muons. In this case a Monte Carlo method is rather reliable, since only kinematic is involved. The results of such a Monte Carlo study are shown in table 5.11, from which we can conclude that it is easier for kaons to reach the CMU via decay in flight than it is for pions, therefore $f^{\pi}_{DIF} < f^{K}_{DIF}$.

5.5.2 ϵ^{π}_{f} vs. ϵ_f from $K^0_s \to \pi^+\pi^-$

Due to the uncertainties in the hadron-Fe and hadron-nucleon cross sections at low energy, and to the difficulty of precisely modeling the CDF calorimeter

P_t	3 GeV/c	6 GeV/c	9 GeV/c
π	0.153 ± 0.005 %	0.124 ± 0.004 %	0.085 ± 0.002 %
K	0.252 ± 0.019 %	0.223 ± 0.013 %	0.180 ± 0.005 %
K/π	1.65 ± 0.14 %	1.80 ± 0.12 %	2.10 ± 0.08 %

Table 5.11: DIF probability for various particles at various P_t values

composition, we decided not to rely on Monte Carlo simulation for what concerns the punch through probabilities. Therefore we will extract ϵ_f^π from the data. To this goal, one needs a sample of pure pions in our p_t range. Such a sample can be obtained by selecting track pairs originating from the $K_s^0 \to \pi^+\pi^-$ decay. We will call $\epsilon_f^{K_s \to \pi}$ the relative CMP efficiency for these pions.

These pions do not constitute a fully unbiased pion sample, but we can show that they provide nevertheless a lower bound for ϵ_f^π:

- K_s^0 typically decay a few cm away from the interaction vertex, therefore these pions have a slightly reduced volume where to decay. This effect make the decay in flight fraction in this sample a little smaller than in the inclusive pion sample.

- the pions that decay with wider angles, may, due the track kink, produce slightly mismeasured tracks that do not reconstruct the correct invariant mass. Therefore some K_0^s will fall outside the invariant mass window used to select this sample and get lost. Again this reduces the fraction of decay in flight.

Since both effects reduce the decay in flight fraction in the sample, pions selected in this way have a smaller f_{DIF} in the CMU, and therefore their relative efficiency to reach the CMP will be reduced, since ϵ_{PT} is quite small and ϵ_{DIF} is $\sim 90\%$. As a consequence $\epsilon_f^{K_s \to \pi} < \epsilon_f^\pi$.

In order to measure $\epsilon_f^{K_s \to \pi}$ we use the K_s^0 sample described in § 5.1

Again the sample is divided into two subsamples depending on the charge of the muon candidate (test_leg). For each charge sign, given N events from the sample, we then count the number of *signal* K_s events where the "muon" gave a CMP hit, N_P, and obtain the relative efficiency as the ratio N_P/N. In figure 5.17 the invariant mass distributions for the negative-muon-leg K_s are shown in CMU and CMP respectively. As a check the distributions for a positive "muon" leg are also shown in fig. 5.18. We fit these distributions with a gaussian plus a second degree polynomial background function to obtain the background

subtracted numbers entering in the ratios above. We summarize in table 5.12

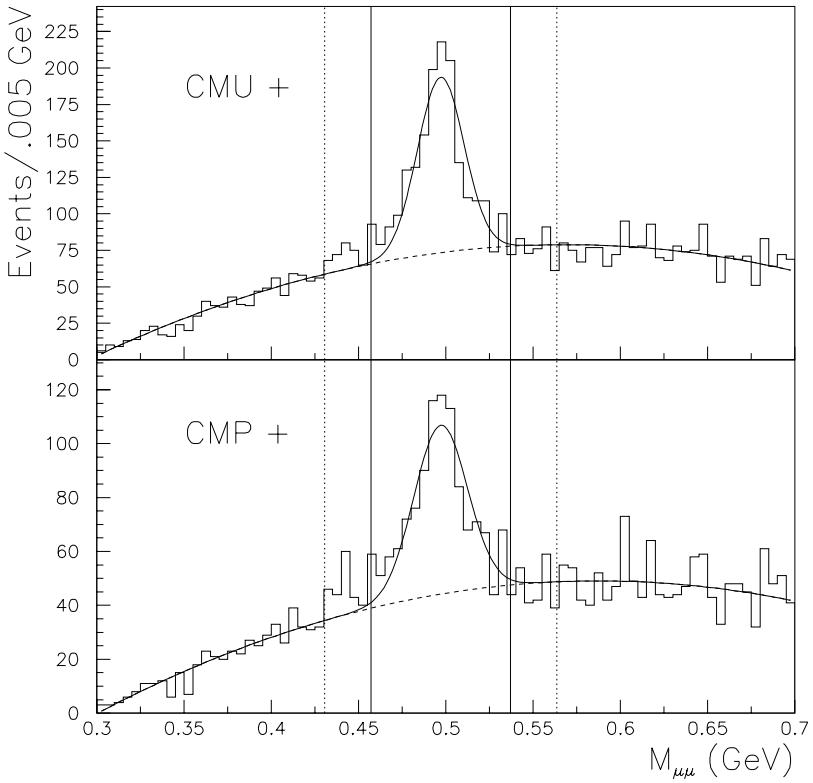

Figure 5.17: Invariant mass distributions of K_s with negative muon leg (upper). Invariant mass distribution as above when the muon leg has a CMP stub (bottom).

the numbers of reconstructed K_s, along with the resulting values of ϵ_f^-, ϵ_f^+. The value of ϵ_{bkg} is computed as a cross check (ϵ_{bkg} is the relative CMP efficiency for muon candidates in the background of the K_s peak, see § 5.4). Since we are dealing with pion fakes no sign dependence is expected for the CMP relative efficiency. On the other side the background to the K_s peak is enriched in true muons with respect to the background plus peak, and therefore ϵ_{bkg} is expected to be larger than ϵ_f^π.

Finally, the P_t dependence of ϵ_f is studied by dividing the K_s^0 sample into slices of "muon" P_t. For each slice the invariant mass distribution is obtained, and a fit to a gaussian plus polynomial background is performed, giving ϵ_f as the ratio $N_{\rm CMP}/N_{\rm CMU}$. In fig. 5.19 the values of ϵ_f^- and ϵ_f^+ are plot versus the "muon" P_t. No significant dependence is observed in the relevant P_t range, so that we are justified in using a single lower limit for ϵ_f^-, irrespective of the

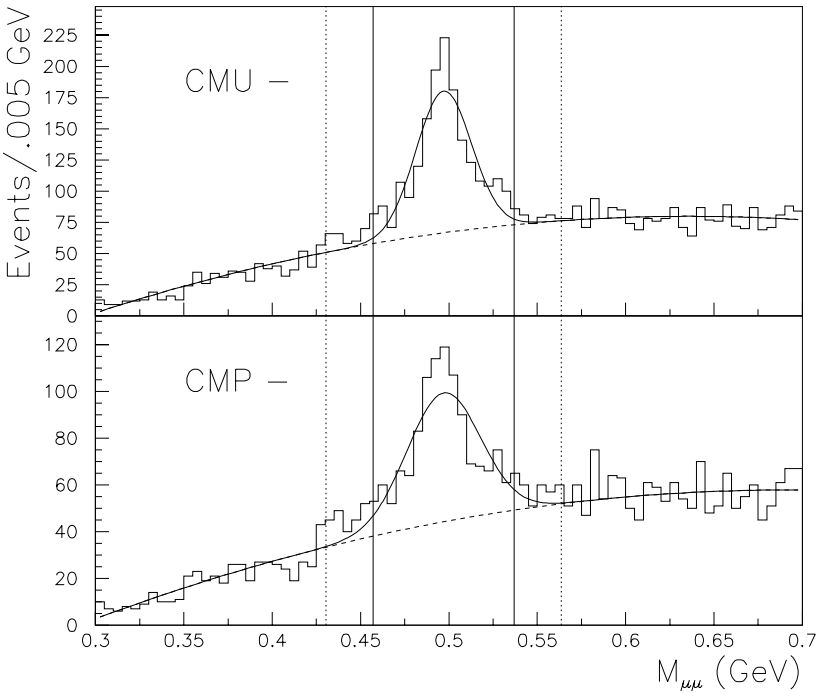

Figure 5.18: Invariant mass distributions of K_s with positive muon leg (upper). Invariant mass distribution as above when the muon leg has a CMP stub (bottom).

	CMU+	CMU−	CMP+	CMP−
Signal + Bkg	2110	2094	1260	1318
Background Fit	1215	1094	738	752
Background Sidebands	1239	1128	745	750
Signal - Fit	895±46	1000±46	522±35	566±36
Signal - Sidebands	871±46	967±46	515±35	569±36
ϵ_f S-Fit			0.58±0.05	0.57±0.04
ϵ_f S-SB			0.59±0.05	0.59±0.05
ϵ_{bkg} (fit)			0.61	0.69
ϵ_{bkg} (SB)			0.60	0.66

Table 5.12:

transverse momentum.

In conclusion, from averaging over positive and negative pions, we obtain $\epsilon_f^{K_s \to \pi\pi} = 0.58 \pm 0.03$; this value will be used as a lower limit on ϵ_f^- and indicated with $\epsilon_f^{-,\ell}$.

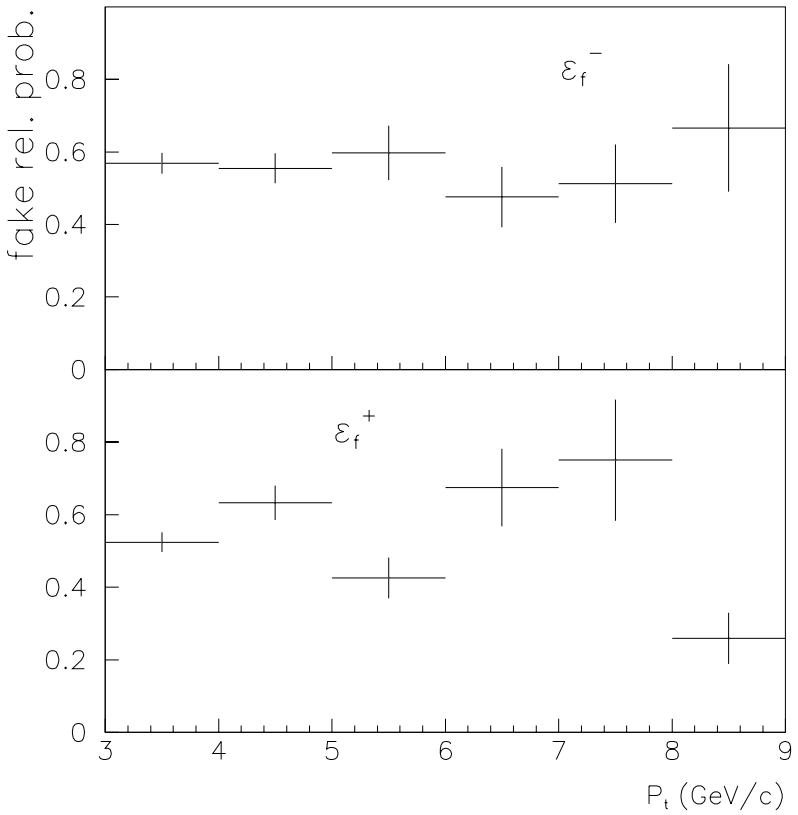

Figure 5.19: ϵ_f^- (top), and ϵ_f^+ (bottom) from K_s as a function of the "μ" P_t.

5.5.3 Effect of protons and anti-protons

Until now we have discussed the fake content of the dimuon sample as if only kaons and pions were produced in the interactions. Instead a substantial fraction of the hadrons originating from $\bar{p}p$ collisions is constituted of protons and anti-protons, either produced directly or from the decay of heavier baryons (e.g. $\Lambda \to p\pi$). Both protons and anti-protons are stable particles, so they do not contribute to the DIF fake fraction, but may and will contribute to the PT fraction, since the

interaction length for protons and pions in the few GeV energy range is similar. This is illustrated in figure 5.20 where the capability of penetrating the CDF calorimeter without interacting is studied for the various hadron species. Since experimental data for the hadron-Fe cross sections are only available for high hadron momentum, the curves shown have been obtained by extrapolating at low energy the hadron-Fe cross sections measured at 60 GeV, using the energy dependence of the $\bar{p}p$ and pp cross sections as a guide. This method is being used since long time in CDF [40] and has been checked in several analysis, e.g. [42].

The first question we have to answer is how many protons (or antiprotons) can be expected in each event. The particle content in $\bar{p}p$ collisions has been the subject of several experiment in the past, but unfortunately data exist only for either lower center-of-mass energies or lower hadron momentum than the range we are interested in. The proton/pion ratio has been measured by the British-Scandinavian collaboration [43] at the ISR at center of mass energies $\sqrt{s} = 23.4, 30.6, 44.6, 52.8$ and 63.0 GeV, in the p_t range 0.2-4 GeV, where they reported a proton fraction that rises with p_t up to 20% of the total charged multiplicity, and a considerably smaller anti-proton fraction. Their findings have been later confirmed by the Chicago-Princeton collaboration [44] in a fix target experiment at Fermilab ($p_{beam} = 200, 300$ and 400 GeV) which extended the measurement to $p_t \simeq 7$ GeV and reported a decrease of the proton fraction as p_t grows from ~ 3 to 7 GeV. Recently data have become available at higher energies from the E605 experiment [45] at Fermilab working with a fix target spectrometer at $p_{beam} = 800$ GeV ($\sqrt{s} = 38.8$ GeV). They measured the p/π^+ and $\bar{p}/\pi^-$ ratios in the p_t range 1-10 GeV, and reported for the $2 \sim 4$ GeV region values as high as 0.4 for p/π^+ and 0.1 for $\bar{p}/\pi^-$. As these results have obtained using a Beryllium target, they need to be extrapolated to the $\bar{p}p$ collision case; such an extrapolation has been studied by the Chicago-Princeton collaboration, which showed that results from Beryllium and Hydrogen target agree within 50%. Measurements at higher center-of-mass energies are only available [3] from the E735-C0 experiment [47] at the Tevatron ($\sqrt{s} = 1800$ GeV), but this experiment only have data for very low hadron momentum ($p_t < 1.2$ GeV).

All these experiments measured a weak dependence from center-of-mass energy of the p/π ratio in their p_t overlap regions, therefore it is not inappropriate to take the fix target results as indicative of the present CDF situation (hadron p_t in the 3-6 GeV range, and $\sqrt{s} = 1800$ GeV). An additional issue is the handling of the large discrepancy in the results for p/π^+ and $\bar{p}/\pi^-$. At low energies these ratio differ up to a factor ~ 4. At collider energies, the experiment C0 only

[3] Also the UA5 experiment [46] at the CERN SPS looked at production of specific particle types at collider energies ($\sqrt{s}$ from 200 to 900 GeV), but they only measured the k/π ratio.

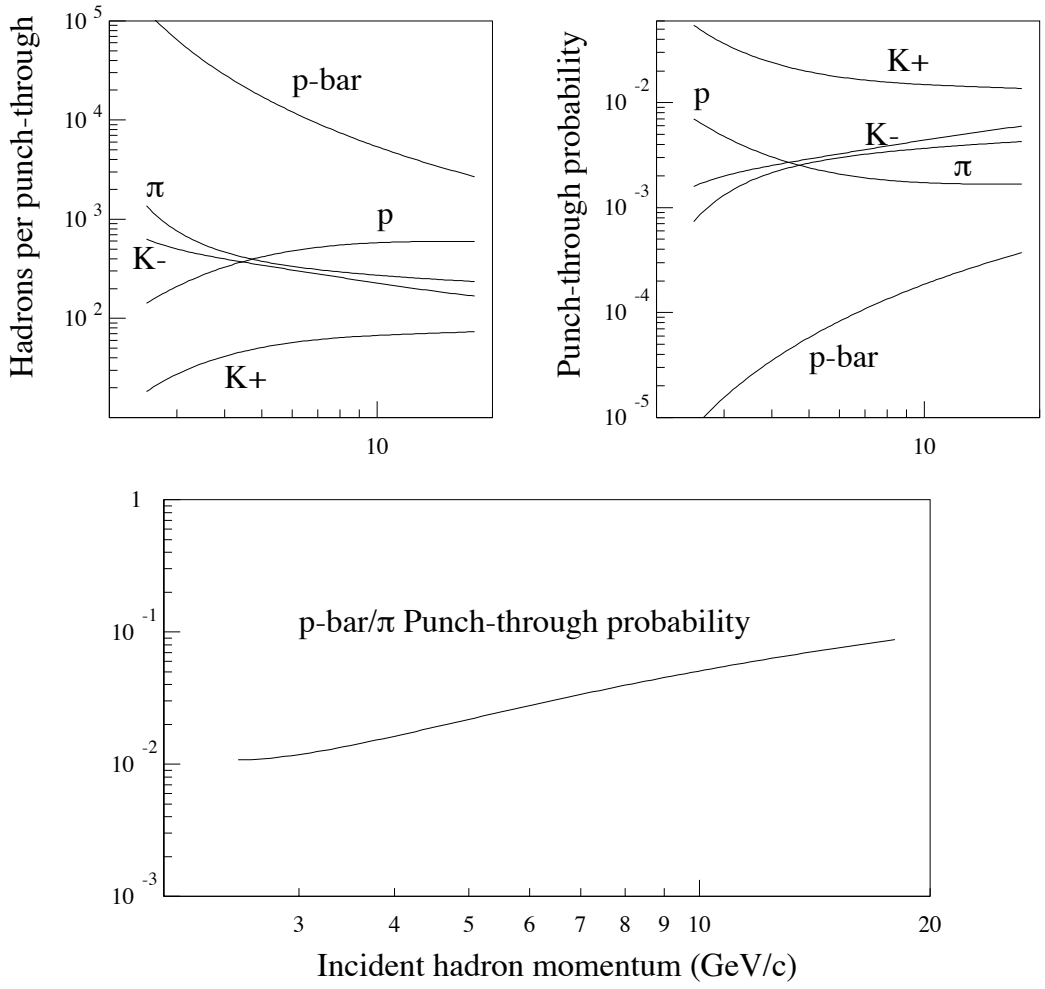

Figure 5.20: Punch-through contribution to CMU muon candidates as a functions of the hadron p_t. All distributions take into account dE/dx energy loss and average of absorbing material in the pseudorapidity interval $-0.6 < \eta < 0.6$.
Top left: Number of hadrons needed to produce one punch-though signal in the CMU.
Top right: Probability for each hadron kind to reach the CMU without interacting.
Bottom: Punch-though probability ratio for $\bar{p}$ vs. π.

reported results for anti-protons due to experimental difficulties with background subtraction. This discrepancy is expected to vanish at high energy as production from gluon splitting starts to dominate over valence quark scattering. The best that once can do is to take the average of the two ratios and use their discrepancy as an additional uncertainty.

In conclusion as many as $10 \sim 20\%$ of the particles produced in a typical $\bar{p}p$ interactions can be proton or anti-protons. At first sight, having ignored their contribution may look improper, but one should keep in mind that the only quantity we are trying to estimate from the data is ϵ_f^-, i.e. we are only interested in *negative* particles. Consequently, we can disregard the large CMU fraction due to protons, we only care about anti-protons. Besides, the hadrons that may give a fake CMU stub have moderate momentum, as the p_t distribution of our CMU candidates clearly shows (figure 5.13). Low energy anti-protons have a high probability to suffer annihilation when traversing the CDF calorimeter iron, and indeed, as shown in the bottom plot of figure 5.20, in the momentum range $3 \sim 6$ GeV they have a punch through probability about 2 orders of magnitude smaller than pions.

In this way we can conclude that even an anti-protons/pion ratio as high as 20% , would be reduced to 0.2% at the CMU. The implication for ϵ_f^- is that with respect to the situation we examined in the previous sections, the ϵ_{PT} fractions may be increased by about 0.2%, in turn lowering ϵ_f^- by less then this amount.

Therefore the effect on ϵ_f^- is definitely smaller then our experimental uncertainty on the determination of the lower limit from $K_s^0 \to \pi^+\pi^-$. Consequently we will keep the above determined range for ϵ_f^- and simply forget about anti-protons.

5.5.4 ϵ_f^- from $\Phi^0 \to K^+K^-$

As a cross check that $\epsilon_f^{K_s \to \pi\pi}$ is actually a lower bound to ϵ_f^- we reconstruct in our sample events with one muon leg which is a misidentified kaon from the decay of a ϕ. To this purpose we look in each event for a negatively charged CMU muon candidate, in the CMP fiducial volume, passing all the cuts in the standard selection. In the hypothesis that it is a misidentified kaon we perform a vertex constrained fit with any track with $P_t > 0.4$ GeV/c, and then form the invariant mass distribution in the region of the ϕ (fig. 5.21a). By background subtraction we obtain the number of ϕ decays with a misidentified muon leg in the CMU passing all the cuts, $N_U^\phi = 109 \pm 27$. A fraction of these misidentified muons will also give a hit in the CMP (fig. 5.21b); the background subtraction gives $N_P^\phi = 59 \pm 22$. The ratio of CMP ϕ's to the total gives the relative efficiency

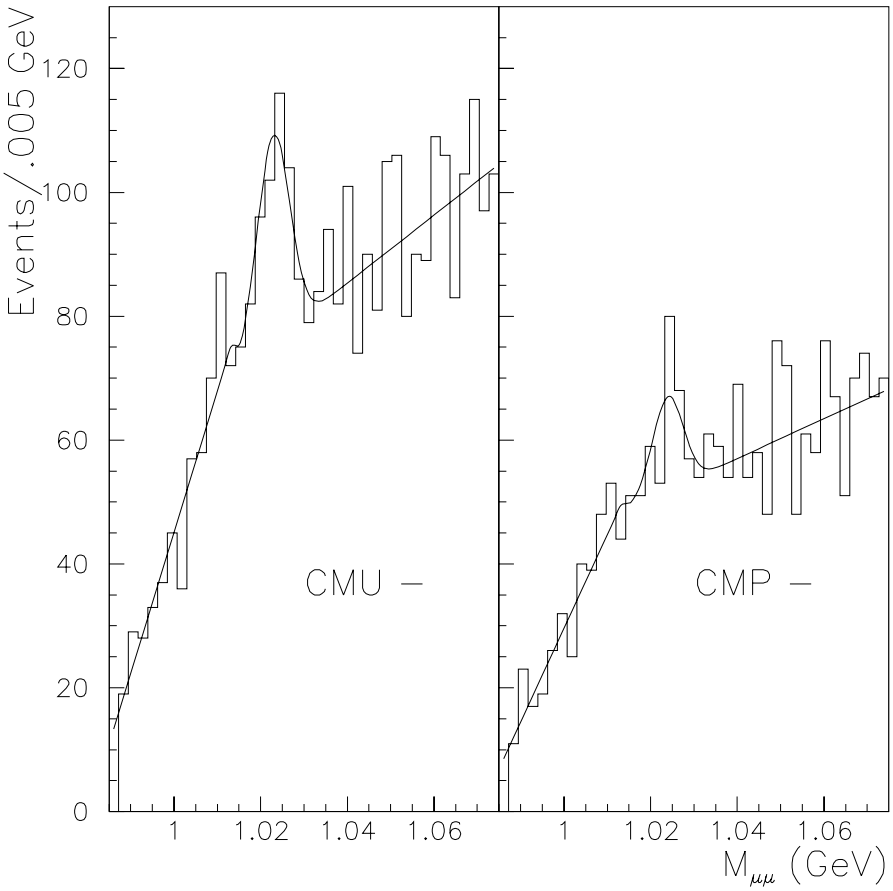

Figure 5.21: a)Invariant mass distributions of ϕ candidates with a CMU leg passing all the cuts. b) Invariant mass distribution as above when the muon leg has a CMP hit.

for a K^- to get to the CMP: $\epsilon_f^{-,\phi\to KK} = 0.54 \pm 0.24$. This result is consistent, within its large error, with the value obtained previously as a lower limit to ϵ_f^-.

5.6 True muon fractions

To obtain the number of true muons in each category, information on ϵ_f^- is added to the dimuon equation solutions presented in section 5.4, fig. 5.16. The number is computed using a Monte Carlo technique, in which the values of N_{UU}, N_{UP}, N_{PP}, ϵ_μ and ϵ_f^- are varied at each iteration according to their distributions. For ϵ_f^- an upper limit is derived by the condition that the F_1 be positive, as discussed in § 5.4. Since F_1 has in fact a range of values, determined by its error band, the limit is obtained at each iteration of the Monte Carlo, according to the extracted values of the N's and ϵ_μ. The lower limit to ϵ_f^- is the measured $\epsilon_f^{K_s\to\pi\pi}$ of § 5.5; to keep into account the experimental error, for each iteration a lower limit is extracted from a gaussian distribution with mean equals to the value of $\epsilon_f^{K_s\to\pi\pi}$ and sigma given by its error. The value of ϵ_f^- is finally extracted from a flat distribution between the lower and upper limits, determined for that iteration.

5.6.1 Monte Carlo Algorithm

A step-by-step description the algorithm to extract the number of true muon pairs is as follows:

- the N_{UU}'s are extracted, and the N_{UP}'s and N_{PP}'s determined, with the procedure discussed in § 5.4;
- a value of ϵ_μ is extracted from a normal distribution with mean and sigma as measured (§ 5.4);
- a value of ϵ_f^- is extracted from a flat distribution in the $[0,1]$ interval;
- if $F_1(\epsilon_f^-) \geq 0$, and $\epsilon_f^- > \epsilon_f^{-,\ell}$, where $\epsilon_f^{-,\ell}$ is the lower limit determined from K_s^0 , the extraction is retained and the fractions calculated at that value and accumulated in histograms. If $F_1(\epsilon_f^-) < 0$, the extraction is discarded;
- if ϵ_f^- is less than the measured lower limit, another random number q is extracted from a flat distribution in $[0,1]$ and compared to

$$G(\epsilon_f^-) = \exp\left[-\frac{1}{2}\left(\frac{\epsilon_f^- - \epsilon_f^{-,\ell}}{\sigma(\epsilon_f^{-,\ell})}\right)^2\right].$$

If $q > G(\epsilon_f^-)$ the extraction is discarded, otherwise fractions are calculated and accumulated in an histogram;

- finally, the fractions of true and fake muons are obtained as the mean of the histograms with the accumulated values. The various contributions to the error are then determined, as described in detail below.

5.6.2 Statistical and systematic uncertainties

The resulting values for the various fractions and for ϵ_f^+ are summarized in table 5.13.

	M	F1	F2	total true
	$\epsilon_f^+ = 0.52 \pm 0.03$			
++ UU	$0.211^{+0.032}_{-0.031}$	0.16	0.61	554^{+84}_{-81}
OS UU	$0.482^{+0.033}_{-0.033}$	0.14	0.38	3026^{+207}_{-207}
−− UU	$0.282^{+0.042}_{-0.040}$	0.16	0.53	553^{+82}_{-78}
LS PP	0.47 ± 0.07			1023 ± 152
OS PP	0.71 ± 0.04			2705 ± 152

Table 5.13:

To split the uncertainty on the true muon fractions into statistical and systematic effects (determination of the relative efficiency ϵ_μ, uncertainty on $\epsilon_f^{-,\ell}$) the Monte Carlo procedure is performed separately for the statistical fluctuations of the N's, and the variation of the two parameters. First of all the numbers are obtained from the procedure outlined above including all the systematic effects; from the filled histograms in fig. 5.22 the mean is taken as the value of the true fraction. In fig. 5.23 the histograms accumulated for the statistical fluctuations alone are shown with the gaussian fit. In fig. 5.24, for the center values of the N's and ϵ_f^-, the effect of the uncertainty on ϵ_μ is studied. The variation of ϵ_f^- induces an asymmetric fluctuation in the true fractions, since the variation is around the minimum for the M's, as is shown in fig. 5.25.

The resulting numbers are:

$$\begin{aligned} N^{LS} &= 1107 \pm 102(\text{stat.})^{+59}_{-49}(\text{sys.}) \\ N^{OS} &= 3026 \pm 119(\text{stat.})^{+176}_{-170}(\text{sys.}) \end{aligned}$$

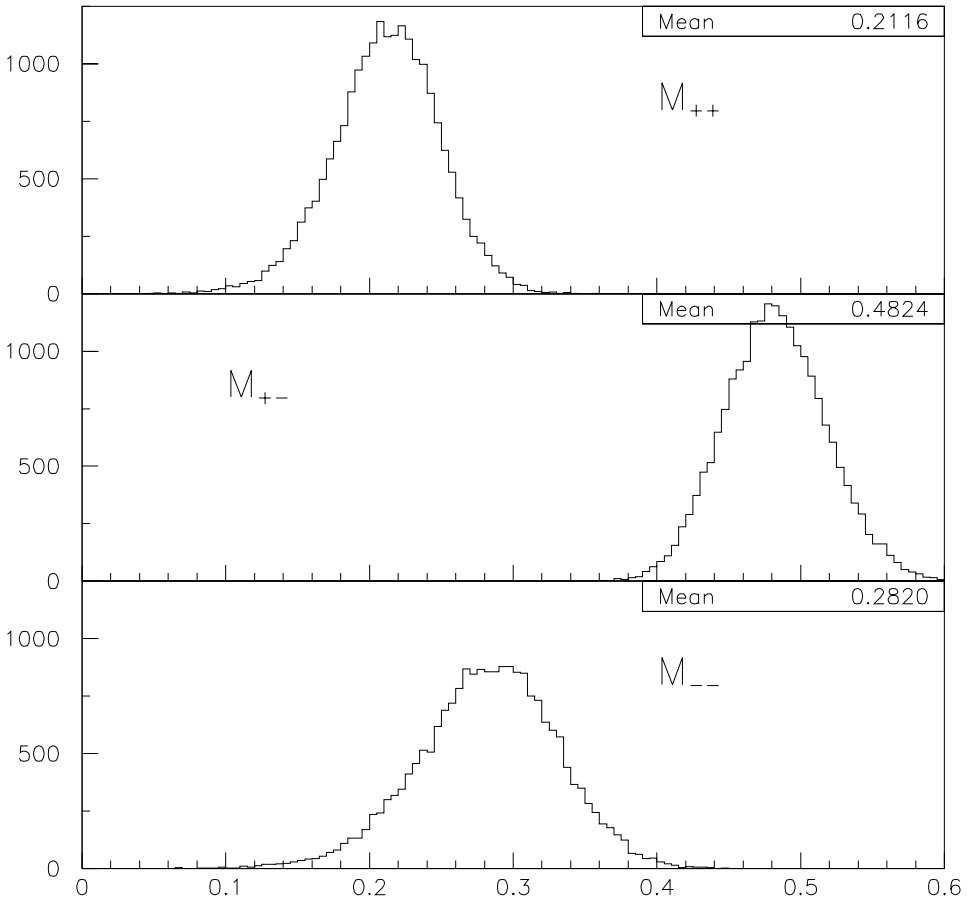

Figure 5.22: Distribution of the true fractions keeping into account statistic as well as systematic errors. The mean is taken as the central value in the following.

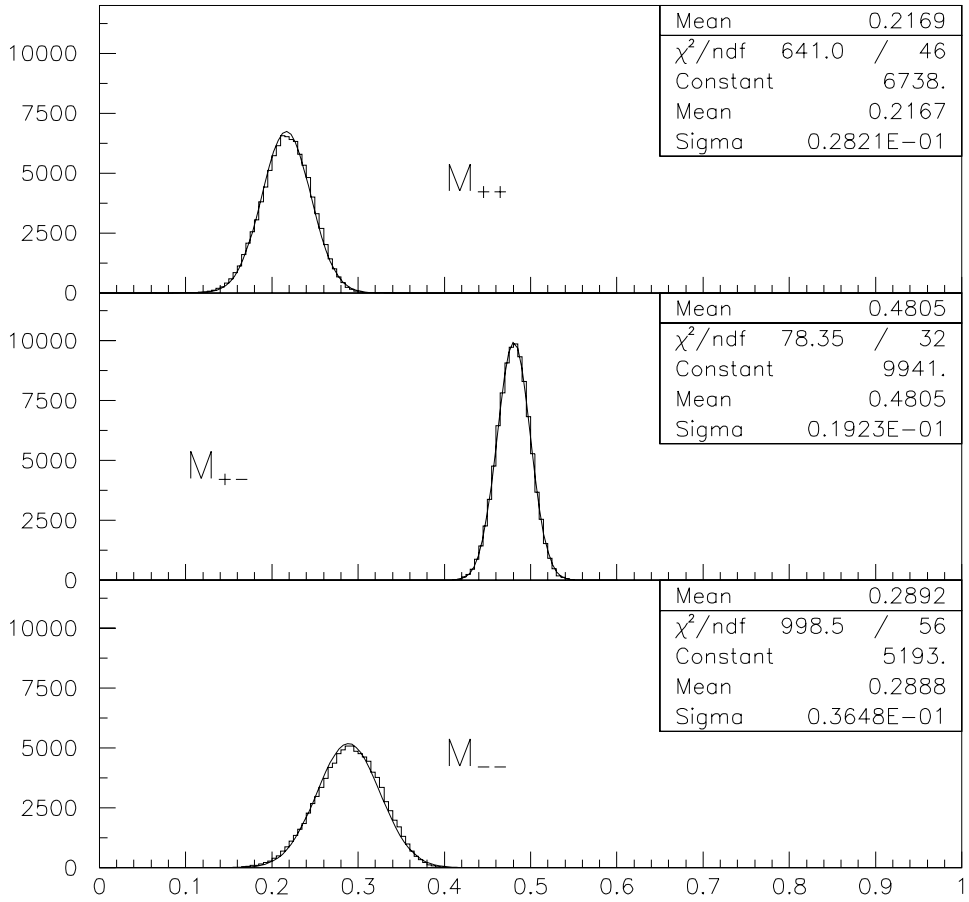

Figure 5.23: Histograms of the values of the true muon fractions keeping into account statistical fluctuations of the N's only. The fit to the gaussian gives the (symmetric) contribution to the overall uncertainties

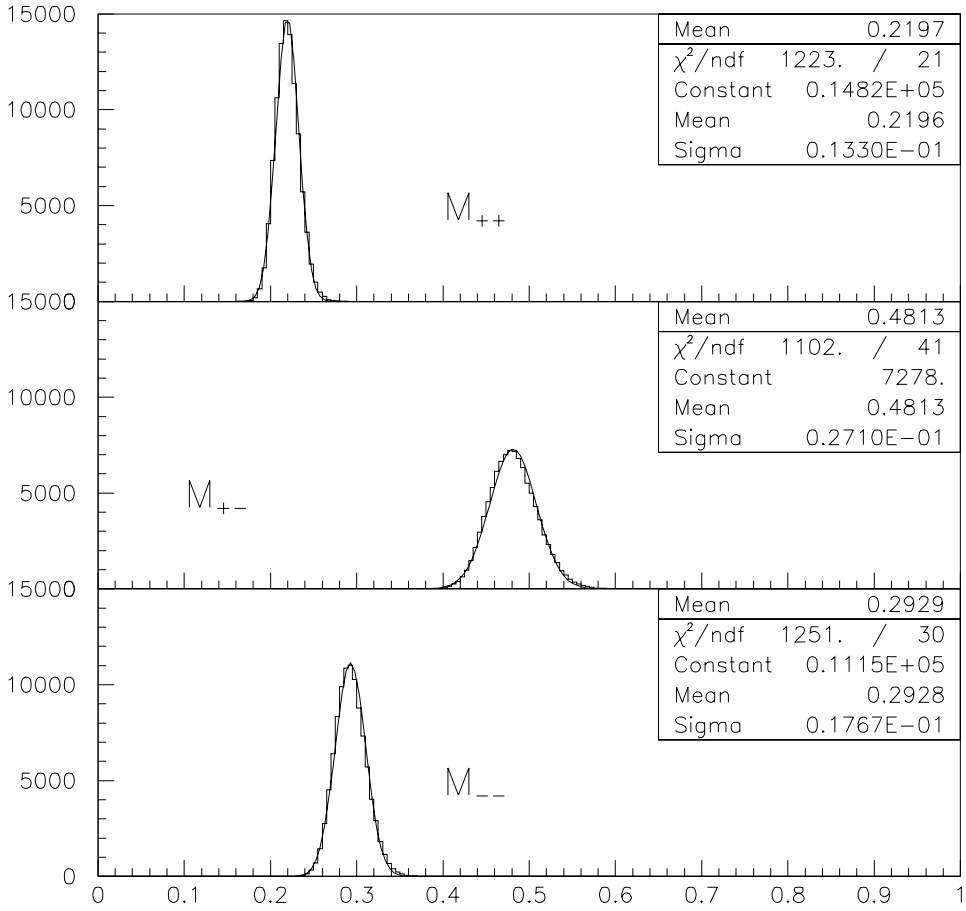

Figure 5.24: As in figure 5.23 for the systematic contribution from the uncertainty on ϵ_μ.

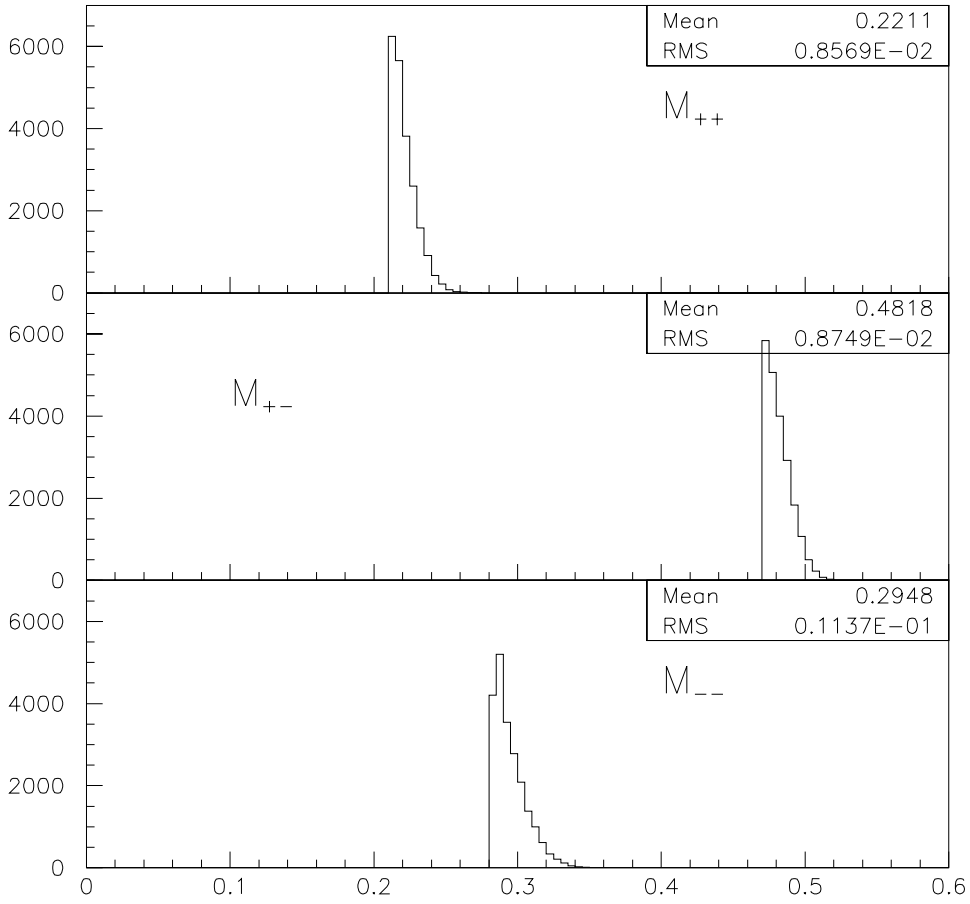

Figure 5.25: The asymmetric deviation of the true muon pair fractions due to the uncertainty on the value of ϵ_f^-. The RMS value is taken as the contribution to the (positive) error on the M's.

Chapter 6

Determination of R and $\bar{\chi}$

To determine R the remaining sources of OS dimuons are studied. In § 6.1 we discuss the cosmic ray background and its subtraction, and in § 6.2 the number of prompt OS dimuon pairs from Drell-Yan in the sample is determined and subtracted from the OS. With this the workout of R is concluded and various contributions to the final error on R are discussed in § 6.3. In § 6.4 the value of $\bar{\chi}$ is obtained from R, using a Monte Carlo determination of the fraction of sequentials, and a determination of the fraction of direct charm production from eμ data [48].

6.1 Cosmics background

Cosmic rays can hit the detector in time with the beam crossing window. A high-energy cosmic ray going through the center of the detector can simulate a pair of opposite charge muons. It is therefore necessary to make sure that background events from cosmic rays are either negligible or taken into account. In fig. 6.1a the distribution of the 3–D angle between the two muon tracks is shown for the UU OS sample before applying the impact parameter cut; comparing it to the superimposed UU LS distribution, which is expected to be free of cosmics, a cosmic ray signal is evidenced by the small excess in the OS distributions at $\Delta\phi \simeq 2\pi$.

After the impact parameter cut (fig. 6.1b) the excess is much less important, but still present. We choose to evaluate this excess and to subtract it from the number of UU OS events. A linear fit to the last 6 bins (shown in fig. 6.1c) gives $N_{\text{cosmic}} = 21 \pm 7$. This will be subtracted from OS when obtaining R.

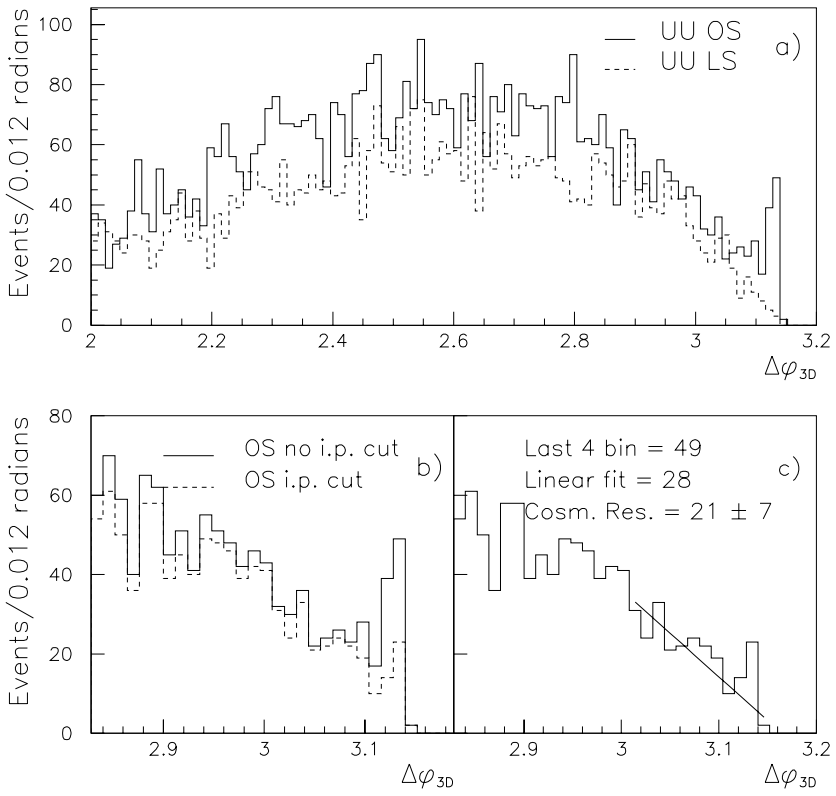

Figure 6.1: a)$\Delta\Phi_{3D}$ distribution for OS (solid) and LS (dotted) CMU-CMU pairs passing all cuts except the impact parameter cut. The small excess at $\Delta\Phi_{3D} = 2\pi$ indicates the presence of cosmic ray background. b) After the impact parameter cut the excess is much less evident. c) A linear fit is used to evaluate the residual background from cosmics.

6.2 Drell-Yan background

While Drell-Yan pairs are produced as prompt leptons directly from the hard scattering of a quark-antiquark pair, b-quarks are produced as jets, and similarly fake muons originate mostly from pions and/or kaons produced in the hadronization of jets. The jet production process results in more energy being produced close to the leading lepton (or hadron) than it is in the case of prompt leptons, which have no fragmentation, no hadronization and no color in the final state. Therefore Drell-Yan muon pairs are expected to be fairly isolated with respect to dimuons from $b\bar{b}$ decays and fake muons.

We use this difference in energy flux around the muon to separate Drell-Yan muon pairs within our subsample. We define an isolation transverse energy $E_t^{iso}(i)$ as the transverse energy measured in a cone of $R = \sqrt{\Delta\eta^2 + \Delta\phi^2} = 0.7$ ($E_t^{0.6}(i)$) minus the transverse energy in a cone of $R = 0.4$ ($E_t^{0.4}(i)$) centered along the direction of muon i. This variable was chosen instead of the more obvious $E_t^{0.6}(i)$ or $E_t^{0.4}(i)$, because it showed a better capability of differentiating between isolated muon pairs (an Upsilon sample was used) and b-type production (the CMU-CMU dimuon sample was used as source of non-isolated muons). [1]

Since we want a global variable to account for the isolation of the muon pair we define $E_t^{iso} = \sum_{i=1,2} E_t^{iso}(i)$. Once again, we used the Upsilon sample and the inclusive CMU-CMU sample to check the relative discriminating power of various combination of $E_t^{iso}(1)$ and $E_t^{iso}(2)$, and the sum of the two resulted to be the best choice. The distribution of this variable for the 6287 events in the CMU-CMU OS subsample (after removal of the Υ mass window) is shown in figure 6.2.

In order to use this distribution to evaluate the Drell-Yan content of the sample, we need to model the two contributions to the CMU-CMU OS isolation shape (outside the Υ peak): 1) b+charm+fakes and 2) Drell-Yan. We will then fit the CMU-CMU OS E_t^{iso}distribution with the sum of those two shapes leaving to the fit procedure to adjust the two normalization coefficients. In formulas:

$$E_t^{iso}(OS) = \alpha \cdot E_t^{iso}(\text{DY}) + \beta \cdot E_t^{iso}(\text{N-DY}) \tag{6.1}$$

where:

- E_t^{iso}(OS) is the E_t^{iso}distribution for CMU-CMU OS events (our signal sample)
- E_t^{iso}(DY) is the $E_t^{iso}$for Drell-Yan process (or our best approximation to it)

[1] More complicated track cluster variables (e.g. p_t^{rel}: the momentum of the muon in the direction orthogonal to the closest jet) have been proposed recently [48], but they could not be used in this analysis since at the time this work was already completed.

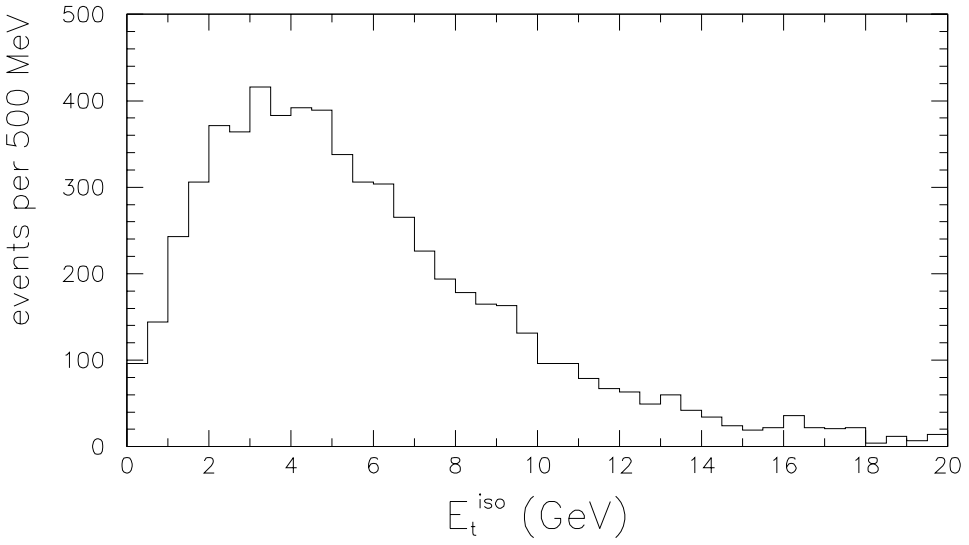

Figure 6.2: E_t^{iso}distribution for CMU-CMU OS events after all analysis cuts.

- E_t^{iso}(N-DY) is the E_t^{iso}distribution for the bottom+charm+fakes (or our best approssimation for it)
- α and β are fit parameters and the fit is performed by minimizing the χ^2 resulting from the sum of the bin-by-bin difference of the left hand side and right hand side members of equation 6.1, divided by the statistical error and squared.

The number of Drell-Yan events to be subtracted (N_{D-Y}) will be obtained as α times the integral of the E_t^{iso}(DY) distribution used in the fit.

6.2.1 E_t^{iso} modeling for non-Drell-Yan component

Since the Drell-Yan process only produces opposite sign di-muons, the shape for the non-Drell-Yan contribution can be obtained from the LS subsample. A naïve choice would be to use the LS CMU-CMU sample, but, since the non-Drell-Yan sample contains both real and fake muons, we have to worry that the E_t^{iso} distribution may not be the same for the two; therefore a bias could be introduced by the fact that the fake fraction is different in the OS and LS CMU-CMU subsamples (see table 5.13). For this reason we use the CMP-CMP LS which has approximately the same fraction of true muons as the CMU-CMU OS (see table 5.13). It should be noticed that the CMP-CMP subsample is only a subset of the CMU-CMU in which tighter quality cuts are imposed on the muon

candidates without using the calorimeter energy, so that the E_t^{iso} distribution of true and fake muons is not biased by restricting ourselves to the CMP-CMP case, only the relative fraction of true and fake is different.

The E_t^{iso} distribution for the CMP-CMP LS (after all analysis cuts, including removal of the Υ mass window) is shown in figure 6.3, we will use that distribution as E_t^{iso}(N-DY) in equation 6.1.

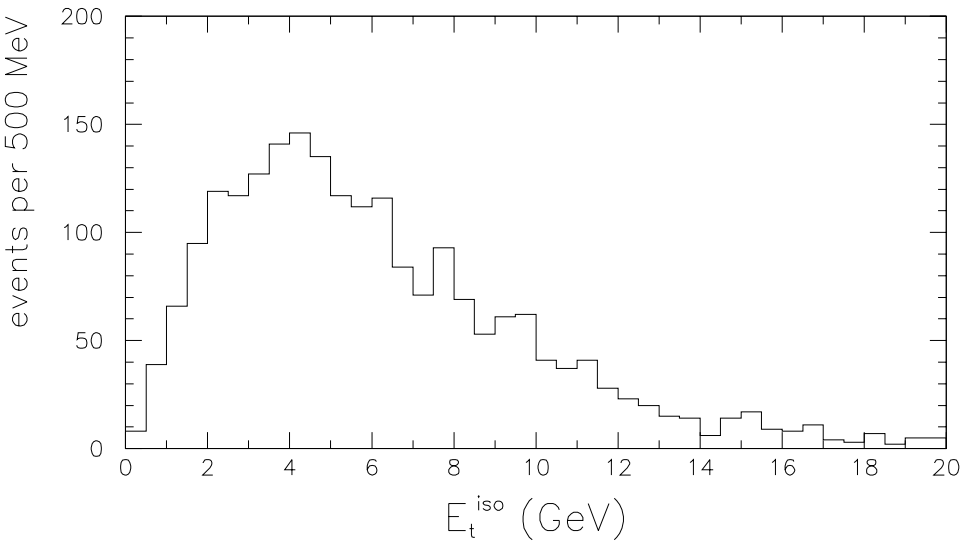

Figure 6.3: E_t^{iso}distribution for CMP-CMP LS events after all analysis cuts.

6.2.2 E_t^{iso} modeling for Drell-Yan

A more delicate task is the modeling of the E_t^{iso}(DY) distribution, since there is no pure Drell-Yan data sample available. In the past CDF has used to this purpose (in the di-electron channel), the E_t^{iso}distribution from Z^0 events [17]. That approach might however be biased, since leptons from Z^0 decay have quite a different P_t distribution than Drell-Yan pairs, which may result in different isolation, and suffer of severe statistical limitation. For these reasons we choose a different approach.

Two methods are used in this analysis to model the E_t^{iso}(DY) distribution.

The first method, is to use Υ decays. They can be extracted from our data sample, simply selecting the proper mass window in the OS di-muon sample.

The second method, is to use a shower Monte Carlo to simulate the Drell-Yan process and the accompanying radiation, and superimpose this to real minimum

bias events to simulate the underlying event (for which parton shower Monte Carlos are unreliable).

Both this methods will have letpon pairs in the same momentum range as the events that we want to model. As explained in the following, the two methods are only slightly biased in opposite directions, so that they should bracket the correct distribution.

As far as the Monte Carlo plus minimum bias is concerned, the resulting E_t^{iso}distribution gives only a lower limit to the energy flux around the Drell-Yan lepton for two reasons:

1. the underlying event in a hard collision is expected to be more energetic than minimum bias, this is expected theoretically and has been reported for example by CDF in comparing minimum bias with the underlying event in jet production [49]

2. the procedure of offline summing of simulated Monte Carlo and real minimum bias events, adds up the two energy distributions in the calorimeter only after the readout threshold has been applied, therefore we treat as zero-energy any individual contribution which was below the threshold. This result in an underestimate of the sum.

In the Υ case, while the main elementary process is very similar to Drell-Yan [50], the initial state is predominantly a gluon pair, while it is a quark pair for Drell-Yan. Since gluons radiate more then quarks, one can expect to have an overestimate of the energy flux when using Υ events.

In this way, our two methods bracket from above and below the E_t^{iso}(N-DY) distribution and therefore the DY fractions obtained with them will bracket the real Drell-Yan content of the CMU-CMU OS subsample.

$\Upsilon \rightarrow \mu^+\mu^-$

When using the $\Upsilon \rightarrow \mu^+\mu^-$ decays to model the E_t^{iso}(DY) distribution, we select a Υ sample from the OS CMP-CMP subsample, which has a higher purity. In figure 6.4 the Υ peak in the two muon invariant mass distribution is shown for both the CMP-CMP OS and the CMU-CMU OS subsamples.

The Υ sample is defined by the cut $9.2GeV \leq m_{\mu\mu} \leq 9.7GeV$ (solid lines in figure 6.4). From that figure it is evident this invariant mass cut will select a sample of events that has both Υ decays and background. To estimate the amount of background, we fit the invariant mass distribution with the sum of a gaussian and a second degree polynomial (this fit is the curve superimposed to

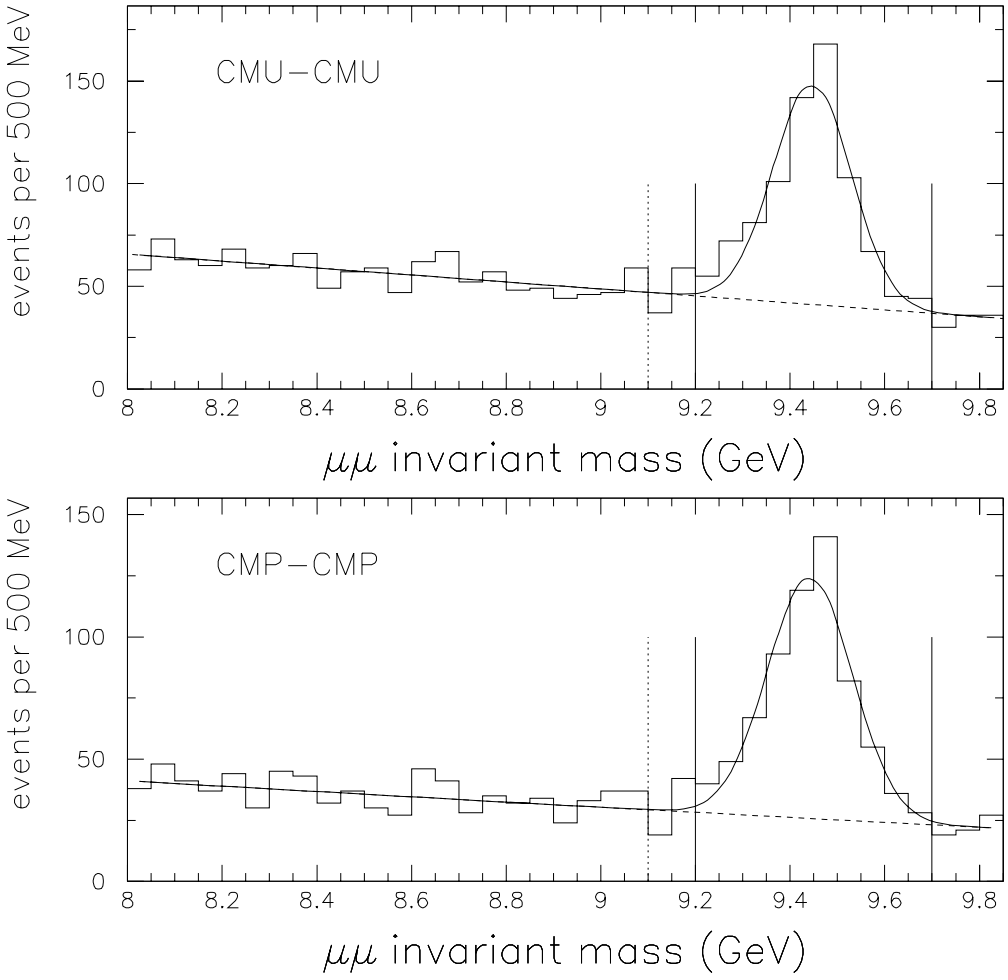

Figure 6.4: Fit to the Υ peak: CMU-CMU (top) and CMP-CMP (bottom). We find 469 ± 30 Υ in the CMU-CMU OS subsample, in the Υ mass window over a background of 430 (top), and 453 ± 27 in the CMP-CMP over a background of 260 (bottom). The black lines indicate the Υ mass window (see text), the region at the left of the dotted line is used to obtain the background E_t^{iso}distribution.

the data in figure 6.4) and use the integral of the fitted polynomial in the 9.2-9.7 GeV mass window (dashed line in the figure) as number of background events.

In order to obtain E_t^{iso}(DY), we subtract from the E_t^{iso}distribution of the events contained in the Υ mass window, the E_t^{iso}distribution for the background. The background distribution is obtained by selecting the muon pairs in the left sideband of the peak: $8.0GeV \leq m_{\mu\mu} \leq 9.1GeV$ (on the left of the dotted line in figure 6.4). Indicating this latter distribution as $E_t^{iso}(\Upsilon_{SB})$ we rewrite equation 6.1 as:

$$E_t^{iso}(OS) = \alpha \cdot (E_t^{iso}(\Upsilon) - \gamma \cdot E_t^{iso}(\Upsilon_{SB})) + \beta \cdot E_t^{iso}(N - DY) \qquad (6.2)$$

The value of γ, i.e. the ratio between the background underneath the Υ peak and the number of events in the sideband, is then left as another parameter in the fit to the E_t^{iso}subsample distribution, adding to the χ^2 the term $(\gamma/\sigma_\gamma)^2$. In this way the value and uncertainty on γ are directly included in the fit results for the parameters and errors. For the CMP-CMP case we estimate from the fit to the di-muon invariant mass distribution:

$$\gamma = 0.33, \quad \sigma_\gamma = 0.02$$

The E_t^{iso}distribution for the Υ sample, for the background (from the sideband) and the resulting model for E_t^{iso}(DY) are shown in figure 6.5.

Minimum bias plus MC

We generated Drell-Yan events in the di-muon channel using the HERWIG Monte Carlo [51], suppressing the underlying event generation. The event then was run through a complete simulation of the detector and $E_t^{iso}$was computed for each muons. On an event-by-event basis, this Monte Carlo events have been combined with minimum bias data by adding to the $E_t^{iso}$of each muon a value obtained from selecting at random a cone in a real CDF minimum bias event. These random cones were chosen with angular distribution obtained from the muons of the CMU-CMU OS sample. The distribution of the resulting values of $E_t^{iso}$is taken as model of E_t^{iso}(DY) for the fit of equation 6.1. This distribution is shown in figure 6.6.

6.2.3 Drell-Yan fraction in the data

By using the $\Upsilon \to \mu\mu$ events to model the E_t^{iso}(DY) distribution, we obtain the fit shown in figure 6.7 where it is compared to the data, i.e. to the CMU-CMU OS

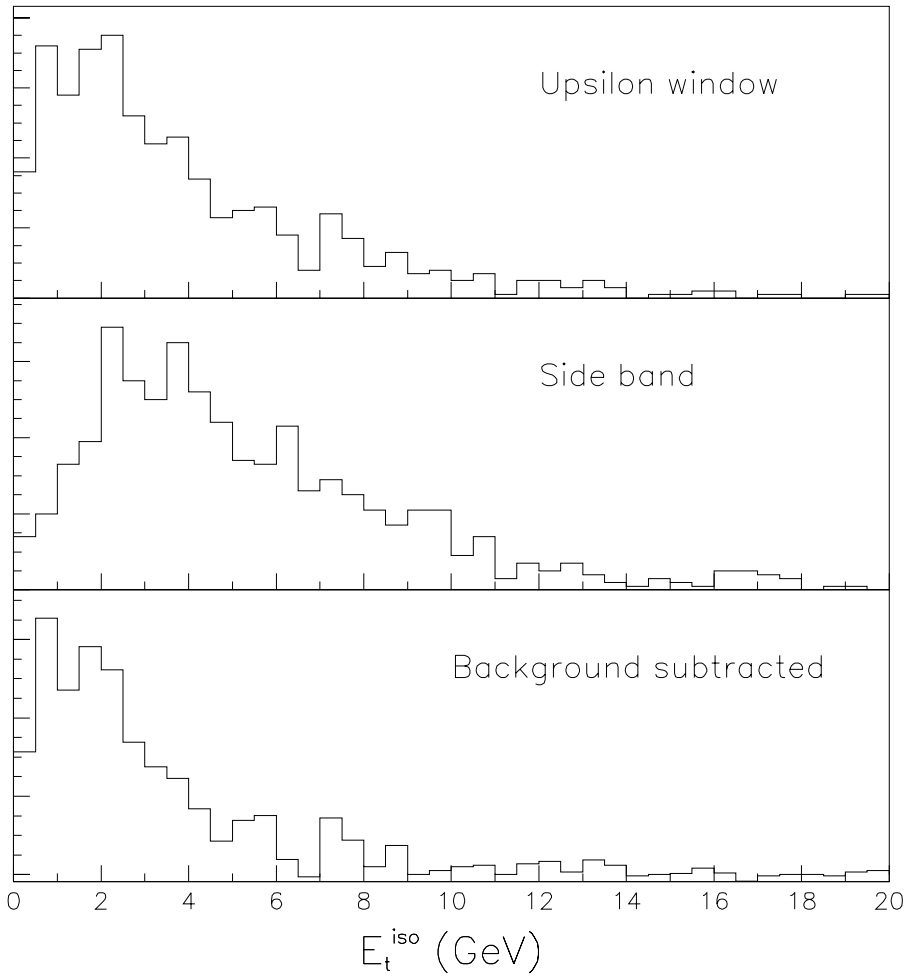

Figure 6.5: E_t^{iso}distributions model for Υ (arbitrary units). Top: CMP-CMP OS events within the Υ mass window; middle: side band events; bottom: background subtracted $\Upsilon \to \mu\mu$ events, i.e. the model for E_t^{iso}(DY).

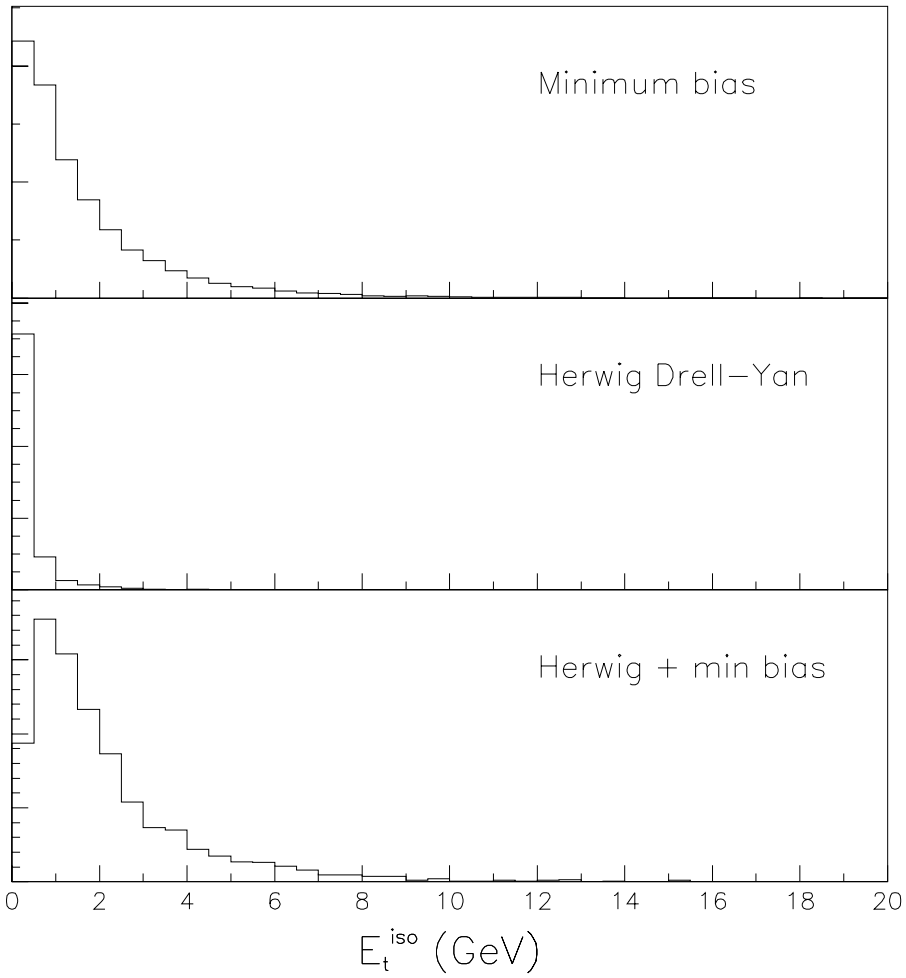

Figure 6.6: E_t^{iso}distributions model for Drell-Yan (arbitrary units). Top: random cones in min bias events; middle: HERWIG Monte Carlo; bottom: sum of Herwig and minimum bias, i.e. the model for E_t^{iso}(DY).

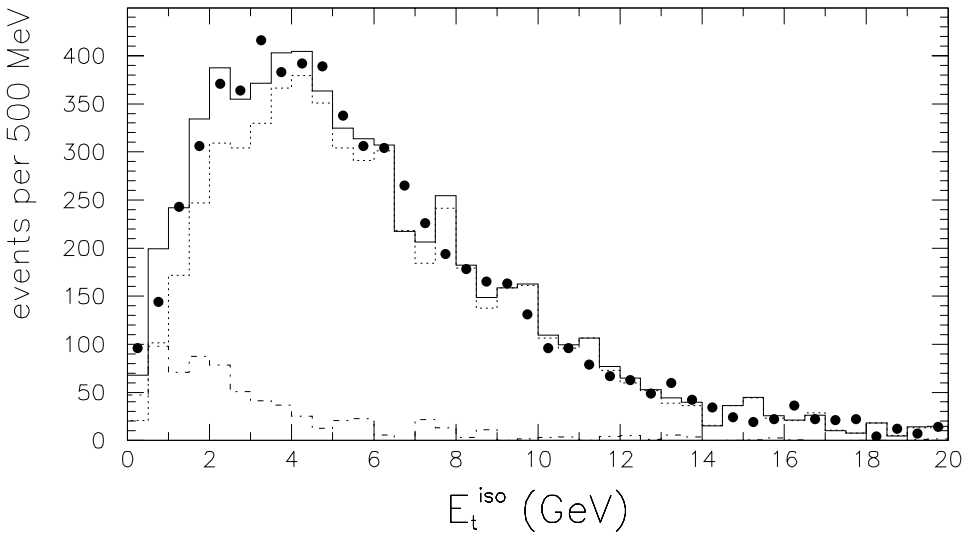

Figure 6.7: E_t^{iso}distributions for the CMU-CMU OS distribution (dots) and the fit from equation 6.2 (solid histograms). The contribution to the fit from $E_t^{iso}(\Upsilon)$ after background subtraction (E_t^{iso}(DY)) is shown by the dashed histogram. The dotted histogram shows the contribution to the fit from the CMP-CMP LS distribution (E_t^{iso}(N-DY)).

subsample. This method estimates the Drell-Yan contribution to be subtracted to the CMU-CMU OS subsample to be 616 ± 106 events.

In the same way, we redo the fit using the minimum bias plus Monte Carlo model for E_t^{iso}(DY). The fit result is show in figure 6.8.

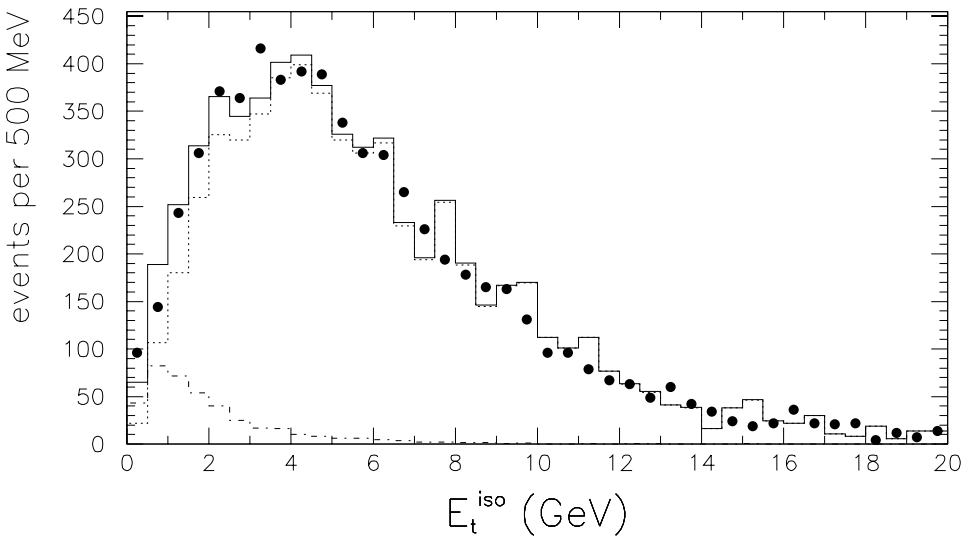

Figure 6.8: E_t^{iso}distributions for the CMU-CMU OS distribution (dots) and the fit from equation 6.1 (solid histograms). The contribution to the fit from the DY Monte Carlo plus minimum bias (E_t^{iso}(DY)) is shown by the dashed histogram. The dotted histogram shows the contribution to the fit from the CMP-CMP LS distribution (E_t^{iso}(N-DY)).

With this procedure we estimate the residual Drell-Yan pairs in our subsample to be 398 ± 70 events.

Since both fits reproduce well the data, and we know that they bracket the correct result, we take the weighted average of the two method as the estimate for the Drell-Yan fraction in the CMU-CMU OS subsample. On the other hand, the two results are statistically not compatible (a little more than 3σ apart). We treat this discrepancy as systematic uncertainty following the method used by the Particle Data Group [13], and obtain:

$$N_{D-Y} = 460 \pm 110$$

6.2.4 Comparison with the CDF measurement of the Drell-Yan cross section

The above analysis provided an estimate for the number of Drell-Yan events in our sample. It is in principle possible to compare this number with a direct estimate based on an independent measurement of the D-Y cross section. CDF has measured the Drell-Yan dilepton production cross section in the range $M_{ll} > 11$ GeV/c^2 [52] using data from 1988-89 run. This cross section measurement can be used in combination with known acceptances and efficiencies to extrapolate the expected number of events over 5 GeV/c^2 invariant mass at the integrated luminosity relevant to the CDF run Ia. We carried on this exercise along the following steps:

1. The published CDF result combines the di-muon and di-electron channel, for each of them:

   (a) the published number of events in each M_{ll} bin was corrected for the published backgrounds in order to obtain the "measured" number of Drell-Yan events (there were in total 172 events before background subtraction, 66 di-muons and 106 di-electrons).

   (b) these numbers were individually corrected for the published efficiencies and acceptances

   (c) the results were summed to obtain the integrated number of Drell-Yan events for $M_{ll} > 11$ GeV/c^2 which resulted to be 850 ± 280 di-electron events in 4.13 pb^{-1} of integrated luminosity and 1173 ± 540 di-muon events in 2.77 pb^{-1}.

2. the integral for the dimuons was rescaled to the di-electron luminosity, and the two numbers averaged to give a total of 950 ± 270 Drell-Yan events in either di-lepton channel for $M_{ll} > 11$ GeV/c^2 in 4.13 pb^{-1}.

3. this number was rescaled to the luminosity of the present sample, taking care of the fact that in the meanwhile the absolute luminosity normalization for CDF changed by $\sim 10\%$ [53], which gives 3744 ± 1050 Drell-Yan events.

4. this number of events was extrapolated to the invariant mass range of the present sample ($M_{ll} > 5$), using the integral mass distribution from HERWIG Monte Carlo events after simple kinematic and geometrical cuts meant to reproduce the acceptance of the published CDF analysis (this extrapolation factor turned out to be of the order of 4.5) to obtain 16500 ± 5000 events.

5. this number was normalized for the present analysis kinematic cuts acceptance (obtained from the same Monte Carlo used for the mass extrapolation, with no detector simulation) to 1600 ± 500 events

6. finally we further multiply by the present analysis quality cut efficiency (93% for each muon from a sample of $J/\psi \to \mu\mu$ events), and for the trigger and offline reconstruction efficiency (that we got from other ongoing CDF analysis) and for the CMP geometrical acceptance. The final number is 240 ± 70 Drell-Yan events with $M_{ll} > 5$ GeV in 16.4 pb^{-1} of data.

In conclusion, from extrapolating the published CDF Drell-Yan cross section measurement, 240 ± 70 events are expected in our sample, where the error is only statistical.

When we look back at the many steps in the procedure and at the big multiplicative factors involved (we started with 172 events and inflated it to 20k before bringing it down again to 240), and when we consider that for the present analysis (that was not meant to be a cross section measurement) the acceptance and efficiency have not been studied in great detail, that the published cross section had a factor two discrepancy between the di-electron and the di-muon channel, that the Monte Carlo extrapolation we used to expand down the mass range has never been checked with data and has large uncertainties due to the choice of the parton distribution functions, and finally the fact that we did not include several systematics uncertainties, the comparison between the present extrapolation (240 ± 70) and the above estimate obtained mostly from present data (460 ± 110) is quite satisfactory.

For all the above stated reasons, we consider this extrapolation only a check of the estimate reported in the previous section, and do not average the two together.

6.3 The R ratio

The ratio of the number of LS to OS pairs is finally determined with its errors. The total number of true LS is the one determined in section 5.6. From the total number of OS pairs determined there the number of Drell-Yan events estimated in 6.2, as well as the number of pairs from residual cosmic ray events, from 6.1, must be subtracted:

$$R = \frac{N^{LS}}{(N^{OS} - N^{DY} - N^{COSMIC})} = 0.435 \pm 0.044(\text{stat.})^{+0.038}_{-0.035}(\text{sys.})$$

In table 6.1 the various contributions to the error on R are summarized and the final overall error is the quadrature sum of all the contributions.

Source	Error
Statistical	± 0.044
ϵ_μ	± 0.031
$\epsilon_{\bar{f}}$	$+0.015$
Drell-Yan subt.	± 0.016
Cosmics subt.	± 0.001
Total	$^{+0.058}_{-0.056}$

Table 6.1: Summary of contributions to the error on R.

6.4 Determination of $\bar{\chi}$

To obtain the value of $\bar{\chi}$ from the experimental value of R extracted in the previous chapter the relation (4.3) is used, which contains three unknown parameters besides $\bar{\chi}$ in the right hand side.

The values for $f_c = N_c/N_f$ and $f_s = N_s/N_f$ are determined by means of a Monte Carlo simulation. Only geometric and kinematic cuts are needed since we expect other cuts to act similarly on true muons either from charm or beauty semileptonic decays. A Monte Carlo determination for an electron-muon sample with exactly the same kinematic cuts as the dimuon sample used for this analysis will be used [48]. The main characteristics of the simulation are recalled in § 6.4.1.

Finally, the relation between χ_d and χ_s induced by the measurement of $\bar{\chi}$ is obtained, using production ratios of B_d and B_s estimated phenomenologically. The result is then compared to the world average measurements of χ_d and $\bar{\chi}$.

6.4.1 Monte Carlo study of B-meson decays

The ISAJET [33] Monte Carlo, version 6.46 was used to generate $b\bar{b}$ and $c\bar{c}$ events; the gluon splitting component is obtained by reiterating the fragmentation stage on generic TWOJET events. Fragmentation is performed in the Peterson fragmentation scheme with $\epsilon = 0.006$, and the Feynman-Field scheme is used for hadronization [55]. The B mesons are decayed using the CLEO Monte Carlo [56], version 9.00, which incorporates the latest results on B branching ratios from the CESR experiment.

Simulated processes

Decay processes of $b\bar{b}$ pairs giving rise to dimuon final states have been already illustrated in § 4.3. They are listed again for convenience hereafter.

Process 1 is the direct semileptonic decay of both b and $\bar{b}$ quarks. In process 2 the b decays semileptonically, while the $\bar{b}$ decays to an hadronic final state which must include a charmed meson; this in turn decays semileptonically into a $\mu\nu_\mu$ + X. Process 3 is the charge conjugate of process 2, and was not simulated separately, but kept into account by doubling the events from process 2. Therefore, only the two processes 1 and 2 have been simulated; the P_t and invariant mass cuts combine to cancel the cascade sequential (same side sequential, process 7 in § 4.3).

6.4.2 Sequentials fraction

$b\bar{b}$ direct production events were generated with ISAJET using a b-jet P_t threshold of 2.9 GeV/c; gluon splitting events were generated with ISAJET generic jet fragmentation with gluon jet P_t threshold at 9.8 GeV/c. The decays were performed using the CLEO updated table, and a fast detector simulation was run to obtain track parameters. For process 1 all $\bar{B}$ and B hadrons were forced to decay semileptonically. For process 2 the B hadrons were forced, while the $\bar{B}$'s were decayed by the standard table, but in the cascade decay the D^+'s were then forced to decay semileptonically, and all other D mesons were forced to decay to leptons with the branching fractions relative to D^+ as given by the CLEO tables. The total contribution to the number of sequential decays to dimuon was taken as twice the number of events in this category passing the acceptance cuts, in order to account for the contribution of process 3.

The simulated samples generated are summarized in table 6.2.

The fraction of sequential decays is obtained as the ratio of the number of events for process 2 and 3 to that for process 1, normalized to account for the

	DIRECT		GLUON SPLITTING	
Process 1	1286	0.835 pb^{-}1	662	2.08 pb^{-}1
Process 2 & 3	420	1.74 pb^{-}1	346	6.64 pb^{-}1

Table 6.2: Summary of simulated $b\bar{b}$ samples.

branching ratio $BR(B^0 \to \mu + X) = 0.107 \pm 0.005$ and $BR(D_s^+ \to \mu + X) = 0.172 \pm 0.019$. The result is $f_s = 0.253$.

The systematic uncertainty on the sequential fraction from the uncertainty on the fragmentation was estimated by varying the Peterson parameter ϵ by 1 sigma, and contributes about 5 %. Uncertainty on structure function and on detector response is the largest contribution to the systematic error on f_s. The final estimate from [48] is $f_s = 0.253 \pm 0.051$.

6.4.3 Charm fraction

The fraction of direct $c\bar{c}$ events, f_c was determined on the eμ sample with the same kinematic cuts as our dimuon data, by fitting a combination of the P_t^{rel} distribution for $c\bar{c}$ and $b\bar{b}$ (from Monte Carlo) to the data distribution [48]. This procedure gives $f_c = 0.106 \pm 0.035$ where the error is statistical only.

6.4.4 Conclusions, the value of $\bar{\chi}$

We have measured the fraction of real muons in the CDF dimuon sample, and estimated the residual content of Drell-Yan and cosmic ray dimuons after our selection. The value of R, the ratio of LS to OS dimuons, thus obtained in § 6.3, along with the values of f_s and f_c can now be inserted in the equation (4.3) from which $\bar{\chi}$ is finally extracted. The result is:

$$\bar{\chi} = 0.121 \pm 0.026(\text{stat.})^{+0.032}_{-0.031}(\text{sys.}).$$

In table 6.3 the error is broken into the various contributions from statistics and systematics. The systematic errors on the sequential and charm fractions are still under study.

The average mixing parameter thus determined gives a constraint on the $\chi_d - \chi_s$ plane shown in figure 6.9, where the fractions P_d and P_s are assumed to be 0.375 and 0.15 [17]. The dotted band indicates the world average value for χ_d. Finally the present result for $\bar{\chi}$ is compared to other results from LEP experiments and the old CDF and UA1 results in fig. 6.10.

Source	Error
Statistical	± 0.026
ϵ_μ	± 0.018
$\epsilon_{\bar{f}}$	$+0.009$
Drell-Yan subt.	± 0.009
Cosmics subt.	± 0.0005
f_s	± 0.022
f_c	± 0.009

Table 6.3: Summary of contributions to the systematic error

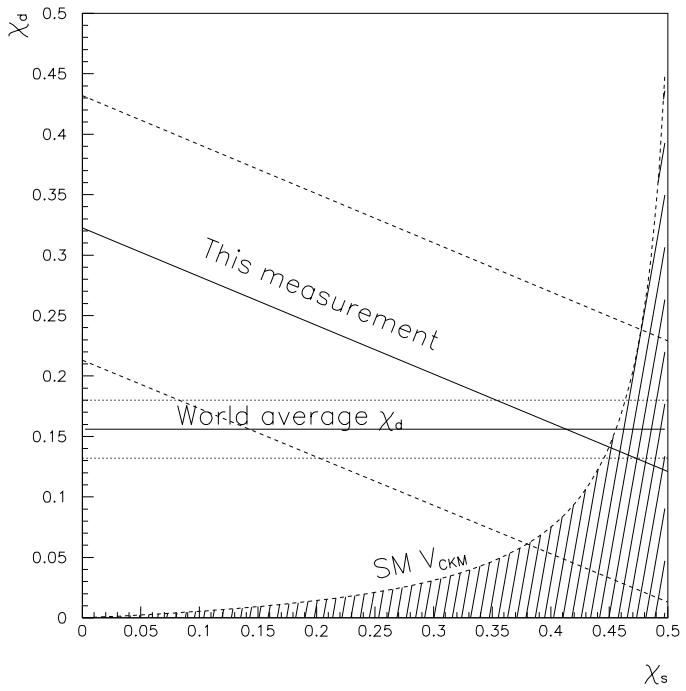

Figure 6.9: Constraint in the χ_d-χ_s plane from the present measurement of $\bar{\chi}$, assuming $P_d : P_s = 0.375 : 0.15$ (dashed lines indicate $\pm 1\sigma$ interval), compared to χ_d world average (dotted lines indicate $\pm 1\sigma$ interval) and the SM unitarity constraint (hatched area)

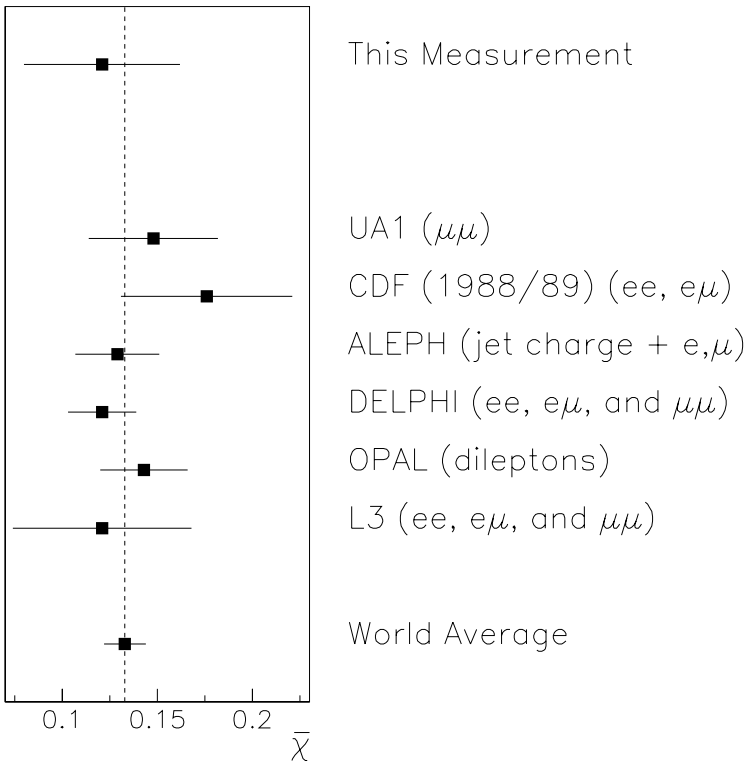

Figure 6.10: Comparison of various measurements of $\bar{\chi}$. The channels used for each measurement are indicated.

The value is in agreement with the measurements of χ_d, the SM constraint, and the world average of $\bar{\chi}$.

Bibliography

[1] S.L.Glashow, Nucl. Phys. **22** (1961, 579; S.Weinberg, Phys. Rev. Lett. **19** (1967, 1264; A.Salam, in *Elementary Particle Theory*, N.Svartholm (ed.), Almqvist and Wiksell, Stokholm (1968).

[2] L.B.Okun, Leptons and Quarks, Interscience (1985), Ch. 21.

[3] D.Karlen, in Review of Particle Properties, Phys. Rev. **D50** (1994), 1416;

[4] M.Kobayashi and K.Maskawa, Prog. Theor. Phys. **49** (1973), 652.

[5] S.L.Glashow, J.Iliopoulos, and L.Maiani, Phys. Rev. **D2** (1970), 1285.

[6] H.Fritzsch, Phys. Lett. **B70** (1977), 436 and Phys. Lett. **B73** (1978), 317; B.Stech, Phys. Lett. **B130** (1983), 189.

[7] M.Gell Mann and A.Pais, Phys. Rev. **97** (1955), 1387

[8] L.Wolfenstein, Phys. Rev. Lett. **51** (1983), 1945.

[9] F.J.Gilman, L.Kleinchnecht and B.Renk in Review of Particle Properties, Phys. Rev. **D50** (1994), 1315.

[10] W.Hollick, talk at the *XVI International Symposium on Lepton-Photon Interactions*, Ithaca, 10-15 August 1993, to be published in the Proceedings.

[11] A.J.Buras *et al.* , Nucl. Phys. **B245** (1984), 369.

[12] F.Abe *et al.* (CDF Collab.), Phys. Rev. **D50** (1994), 2966; Phys. Rev. Lett. **73** (1994), 225; Phys. Rev. Lett. **74** (1995), 2626.

[13] L.Montanet *et al.* (Particle Data Group), Phys. Rev. **D50**, (1994), 1173.

[14] A.J.Buras, M.Jamin and P.H.Weisz, Nucl. Phys. **B347** (1990), 491.

[15] W.B.Atwood and J.A.Jaros, in *B Decays*, edited by S.Stone; World Scientific, 1992.

[16] M.V.Danilov, Proceedings of the LP-HEP '91 Conference, Geneva 1991.

[17] F.Abe *et al.* (CDF Collab.), Phys. Rev. Lett. **67** (1991), 3351.

[18] C.Albajar *et al.* (UA1 Collab.), Phys. Lett. **B192** (1987), 245;

[19] H.Albrecht *et al.* (ARGUS Collab.), Phys. Lett. **B192** (1987), 245; M.Artuso *et al.* (CLEO Collab.), Phys. Rev. Lett. **62** (1989), 2233.

[20] MAC Collab., Phys. Lett. **B200** (1991), 221; MARKII Collab., Phys. Lett. **B240** (1990), 289.

[21] D.Buskulic *et al.* (Aleph Collab.) Phys. Lett. **B284** (1992), 177;

[22] B.Adeva *et al.* (L3 Collab.), Phys. Lett. **B252** (1990), 703;

[23] T.Akers *et al.* (OPAL Collab.), Z. Phys. **C60**, (1993), 199.

[24] L.Abreu *et al.* (DELPHI Collab.), Phys. Lett. **B301** (1993), 145

[25] T.Albajar *et al.* (UA1 Collab.), Phys. Lett. **B262** (1991), 171.

[26] H.Schroder, in *B Decays*, edited by S.Stone, World Scientific, 1992, p.292 and references therein.

[27] F.Abe *et al.* (CDF Collab.), Nucl. Inst. Meth. **A271** (1988), 387 and references therein.

[28] W.C.Carithers *et al.* , Nucl. Inst. Meth. **A289** 388, (1990).

[29] F.Bedeschi *et al.* , Nucl. Inst. Meth. **A268** (1988), 50.

[30] E.Barsotti *et al.* , Nucl. Inst. Meth. **A269**, 82 (1988).

[31] D.Amidei *et al.* , Nucl. Inst. Meth. **A269**, 51 (1988).

[32] F.Abe *et al.* , Phys. Rev. Lett. **61** (1988), 1819.

[33] F.E.Paige and S.D.Protopopescu, BNL Report 37066.

[34] J.J.Hernandez *et al.* (Particle Data Group), Phys. Lett. **B239** (1990),1.

[35] F.Abe *et al.* ; Phys. Rev. **D40** (1989),R3791.

[36] C.Anway-Wiese, CDF internal note 1994;

[37] F.Abe *et al.* (CDF Collab.), Phys. Rev. Lett. **61** (1988), 1819;

[38] S.E.Kopp, C.Grosso-Pilcher; CDF internal note 1992

[39] C.Campagnari, B.Fahrat, P.Sphicas and A.Yagil; CDF internal note 2098

[40] D.A.Smith, PhD thesis, University of Illinois at Urbana-Champaign (1989); D.A.Smith and H.B.Jensen, CDF internal note 707

[41] A.Caner *et al.* , CDF internal note 2363

[42] F.Abe *et al.* ; Phys. Rev. Lett. **71** (1993). 3421.

[43] B.Alper *et al.* ; Nucl. Phys. **B87** (1975), 19.

[44] D.Antreasyan *et al.* ; Phys. Rev. **D19** (1979), 764.

[45] P.B.Straub *et al.* ; Phys. Rev. **D45** (1992), 3030.

[46] G.J.Ansorge *et al.* ; Z.Phys. C **41** (1988) 179.

[47] T.Alexopoulos *et al.* ; Phys. Rev. **D48** (1993), 984.

[48] H.Mitsushio *et al.* ; CDF internal note 2915, CDF internal note 3042.

[49] F.Abe *et al.* ; Phys. Lett. **B70** (1993),1376.

[50] R.Baier and R.Ruckl, Z. Phys. C **19** (1983),251.

[51] G.Marchesini and B.R.Webber, Nucl. Phys. **B310** (1988), 461; G.Marchesini *et al.* , Comput. Phys. Commun. **67** (1992), 465;

[52] F.Abe *et al.* ; Phys. Rev. **D49** (1994),R1.

[53] F.Abe *et al.* ; Phys. Rev. **D50** (1994), 2966;

[54] C.Peterson *et al.* , Phys. Rev. **D27** (1983), 105; J.Chrin *et al.* , Z. Phys. C **36** (1987), 163;

[55] R.Field and R.Feynman, Nucl. Phys. **B136** (1978), 1;

[56] The Monte Carlo is tuned on the most recent measurement of B branching fractions from the CLEO collaboration, as reported in the Review of Particle Properties (see references therein).